UCGE Reports
Number 20193

Department of Geomatics Engineering

Epipolar Resampling of Linear Array Scanner Scenes

(URL: http://www.geomatics.ucalgary.ca/links/GradTheses.html)

by

Michel Morgan

May 2004

UNIVERSITY OF
CALGARY

UNIVERSITY OF CALGARY

Epipolar Resampling of Linear Array Scanner Scenes

by

Michel Fawzy Morgan

A THESIS
SUBMITTED TO THE FACULTY OF GRADUATE STUDIES
IN PARTIAL FULFILMENT OF THE REQUIREMENTS FOR THE
DEGREE OF DOCTOR OF PHILOSOPHY

DEPARTMENT OF GEOMATICS ENGINEERING

CALGARY, ALBERTA

MAY, 2004

ABSTRACT

Normalized image generation (epipolar resampling) is an important task for automatic image matching. Normalized images facilitate the detection of feature correspondences in the images and therefore provide the advantages of reducing the search space as well as the matching ambiguities. Normalized image generation is a well-established procedure for images captured by frame cameras. Digital frame cameras that produce resolution and ground coverage comparable to those of analog aerial photographs are not yet available. Instead, linear array scanners can be used on aerial or space platforms in order to obtain such characteristics. The resulting scenes are formed by stitching the captured one-dimensional images that are produced as the sensor moves. Rigorous modeling necessitates accessing or estimating a large number of exterior orientation parameters of the images. The resulting epipolar lines are non-straight lines, which causes difficulties in epipolar resampling using the rigorous model. By comparison, the parallel projection model requires a smaller number of parameters, and it results in straight epipolar lines. In addition, as the flying height increases and the angular field of view decreases, similar to the case of space-borne scanners, the true perspective geometry can be approximated by parallel geometry. The mathematical models and the transformations related to the parallel projection model and its relation to the rigorous perspective projection model are developed. An approach for epipolar resampling of linear array scanner scenes based on the parallel projection model is established. Experimental results using synthetic as well as real data prove the feasibility of the developed approach.

ACKNOWLEDGEMENT

Thanks be to God, my Father, my Redeemer and my Counselor, that through Him everything is possible. I would like also to thank my family for supporting and believing in me.

I would like to express my gratitude to my supervisor, Dr. Ayman Habib, for his support and guidance throughout my graduate studies. His continuous encouragement and advice were greatly appreciated. Also I would like to thank Drs. Naser El-Sheimy and Matthew Tait, members of my supervisory committee, for the valuable discussions and their comments on my research.

I would like also to acknowledge my teachers and supervisors at my previous institutes, that through them I learnt great deal about photogrammetry and geomatics in general. Among them, I would like to thank Drs. Tony Schenk, Burkhard Shaffrin, Alan Saalfeld (The Ohio State University), Drs. Klaus Tempfli, Moustafa Radwan (ITC Institute), Drs. Youssef Abdel-Aziz, Shawki El-Ghazali, Ashraf Nasr, Yasser El-Manadili (Cairo University).

This research was funded in part by the University of Calgary and the Korean Electronics and Telecommunications Research Institute (ETRI). I would like to acknowledge the University of Calgary for providing me the Silver Anniversary Scholarship. I would like also to thank ETRI for providing the data.

I would like to thank the American Society of Photogrammetry and Remote Sensing (ASPRS), Leica Geosystems, Space Imaging, The International Geographic Information Foundation, Talbert and Leota Abrams Foundation for providing awards, data, internships and financial support that helped me during my PhD study.

TABLE OF CONTENTS

LIST OF TABLES

LIST OF FIGURES

LIST OF SYMBOLS, ABBREVIATIONS, NOMENCLATURE

ADS 40	Airborne Digital Sensor produced by Leica Geosystems
AFOV	Angular Field Of View
CCD	Charged Couples Device
DEM	Digital Elevation Model
DLT	Direct Linear Transformation
DPW	Digital Photogrammetric Workstations
EOP	Exterior Orientation Parameters
GCP	Ground Control Points
IOP	Interior Orientation Parameters
PTP	Perspective to Parallel
P_x	x-parallax
P_y	y-parallax
ROP	Relative Orientation Parameters
SDLT	self-calibrating Direct Linear Transformation
Std	Standard deviation

CHAPTER 1: INTRODUCTION

1.1 GENERAL

Image resampling according to epipolar geometry is a prerequisite for a variety of photogrammetric tasks such as image matching, digital elevation model (DEM) and ortho-photo generation, aerial triangulation, map compilation, and stereoscopic viewing. The resampling process for images captured by the frame camera has been established and implemented in current Digital Photogrammetric Workstations (DPW); for example see Cho et al., 1992. Scanning analog images or using a digital camera directly can produce digital images, which are the input media for DPW. So far, there is no digital frame camera that is capable of producing geometric resolution that is comparable to those produced by analog cameras. To overcome this limitation, linear array scanners have been developed to capture scenes through multiple exposures of several (one to three) scan lines along the image plane. This imaging scenario makes the perspective geometry of line cameras more complicated than that of frame images. Moreover, established procedures for resampling frame images according to epipolar geometry are not suitable for scenes captured by linear array scanners, due to the geometric differences between the two systems. This research will investigate the feasibility of, and develop a methodology for, resampling scenes captured by linear array scanners according to epipolar geometry.

1.2 RESEARCH OBJECTIVES AND SCOPE

The objective of the proposed research is to investigate the feasibility of resampling scenes captured by linear array scanners according to epipolar geometry. The feasibility study starts with the analysis of the epipolar geometry of an imaging sensor using its rigorous model. This requires the availability of the Interior Orientation Parameters (IOP) of the scanner. The IOP include the principal distance, the coordinates of the perspective center, and various lens distortions. Furthermore, the Exterior Orientation Parameters (EOP), which describe the position and the attitude of the imaging sensor as a function of time, are required. After analyzing the epipolar geometry, resampling the scenes using an alternative model “the parallel projection model”, which does not need the IOP or the EOP of the imaging scanner is investigated.

The major objective of this research is to develop an approach for epipolar resampling of linear array scanner scenes. To achieve this goal, other objectives become important including the analysis of the epipolar lines in linear array scanner scenes using the rigorous and approximate models.

1.3 STRUCTURE OF THE DISSERTATION

Chapter 2 contains a literature review; it explains, in detail, the epipolar geometry and resampling for images captured by frame cameras. This review is important since it allows us to investigate potential problems and solutions when dealing with scenes captured by linear array scanners. Chapter 2 also includes an introduction to imaging and stereo coverage alternatives of various line scanners (e.g., SPOT, IKONOS, ADS40). Both the rigorous model and approximate models (including the parallel projection model) are introduced in this chapter. Finally, a review of the literature regarding the epipolar geometry of linear array scanners is presented.

Chapter 3 examines the shape of the epipolar line in linear array scanner scenes with different altitudes and with different stereo coverage methods. This investigation allows us to inspect the deviation of the epipolar lines from straightness for these scenarios. Similar to frame images, cases which yield straight, or close to straight, epipolar lines would be more suitable for resampling these scenes according to epipolar geometry.

The outcome of the investigations in Chapter 3 indicated that it is almost impossible to obtain straight epipolar lines from different linear array scanners with different imaging configurations for stereo coverage. Moreover, it has been established that, as the flying height increases and the Angular Field Of View (AFOV) decreases, the generated epipolar lines become straighter. This particular scenario is very close to parallel projection. Therefore, Chapter 4 has been dedicated to study the parallel projection theory including the mathematical relationship between the object and scene coordinates and the shape of the expected epipolar lines. The necessary tools have been derived throughout this chapter to facilitate the various transformations for epipolar line determination and epipolar resampling.

As indicated in Chapter 4, parallel projection maintains uniform scale. Given this situation, Chapter 5 deals with the necessary transformation of the captured scene according to perspective geometry into parallel projection geometry to maintain uniform scale. In addition, navigation parameters (the EOP of the scanner) may be available and could be used in perspective-to-parallel projection transformation. Therefore, the relationships between the navigation parameters and the parallel projection parameters are derived in this chapter.

Chapter 6 deals with epipolar line determination and the generation of normalized scenes (i.e., resampled scenes according to epipolar geometry). In Chapter 6, the relationship between the x-parallax values in the normalized scenes and the corresponding height is analyzed. The discussion outlines the necessary conditions for having an x-parallax that is linearly proportional to the corresponding elevation. An approach for epipolar resampling is developed in this chapter. Finally, experimental results using synthetic and real data are presented.

Chapter 7 includes a summary, along with conclusions and recommendations of the research.

1.4 RESEARCH CONTRIBUTIONS

This research starts by presenting and closely analyzing the findings from prior literature that are relevant to epipolar resampling of linear array scanner scenes. They include:

- Analyzing the epipolar geometry of frame images and linear array scanners (Chapter 2);
- Analyzing the parallel projection model (Chapter 4); and
- Analyzing the perspective-to-parallel transformation (Section 5.2, Chapter 5);

In this dissertation, many mathematical models, transformations and approaches are developed. Contribution of this research includes:

- Developing the epipolar line equation of the constant-velocity-constant-attitude model and investigating the straightness of the epipolar lines (Chapter 3);
- Developing the transformation between the linear and non-linear forms of the parallel projection model (Section 4.4, Chapter 4);
- Developing the mathematical model relating scenes generated according to the parallel projection that are sharing the same plane or sharing the same projection direction (Section 4.5, Chapter 4);
- Developing a model combining the parallel projection model and the perspective-to-parallel transformation (Section 5.3, Chapter 5);
- Developing the relationship between scanner navigation data and parallel projection parameters (Section 5.4, Chapter 5);
- Developing two approaches to eliminate y-parallax between scenes captured according to parallel projection (Section 6.2, Chapter 6);
- Developing epipolar resampling approach to eliminate y-parallax values and maintain linear relationship between x-parallax and height values (Section 6.3, Chapter 6);
- Testing the developed mathematical models and transformations and the epipolar resampling approach (Chapters 3 to 6); and

- Developing software using C++ programming language for implementing the developed epipolar resampling approach.

CHAPTER 2: LITERATURE REVIEW

2.1 INTRODUCTION

Section 2.2 of this chapter contains a discussion and analysis of the epipolar geometry of frame images (Schenk, 1990; Cho et al., 1992; Zhang et al., 1995; Luong and Faugeras, 1996; Papadimitriou and Dennis, 1996; Schenk, 1999; Tsioukas et al., 2000). Section 2.2.1 introduces some definitions and quantities that are associated with frame images and, more specifically, those associated with stereopair frame images. Section 2.2.2 explains different methods for determining epipolar lines for stereopairs. Epipolar resampling and generating normalized frame images are discussed in Section 2.2.3.

In Section 2.3, linear array scanners are introduced, including the motivation, terminology and methods of stereo observations. Rigorous and approximate models for linear array scanners are also introduced in this section. Finally, a literature review regarding the epipolar geometry of linear array scanners is discussed.

2.2 EPIPOLAR GEOMETRY OF FRAME IMAGES

2.2.1 Definitions

It is important to introduce some terms with their definitions (Schenk, 1990; Cho et al., 1992; Zhang et al., 1995; Luong and Faugeras, 1996; Papadimitriou and Dennis, 1996; Schenk, 1999; Tsioukas et al., 2000). These terms will be used throughout the analysis of the epipolar geometry of frame images.

Figure 2.1 shows two relatively oriented frame images. *O* and *O'* are the perspective centers of the left and right images, respectively, at the time of exposure.

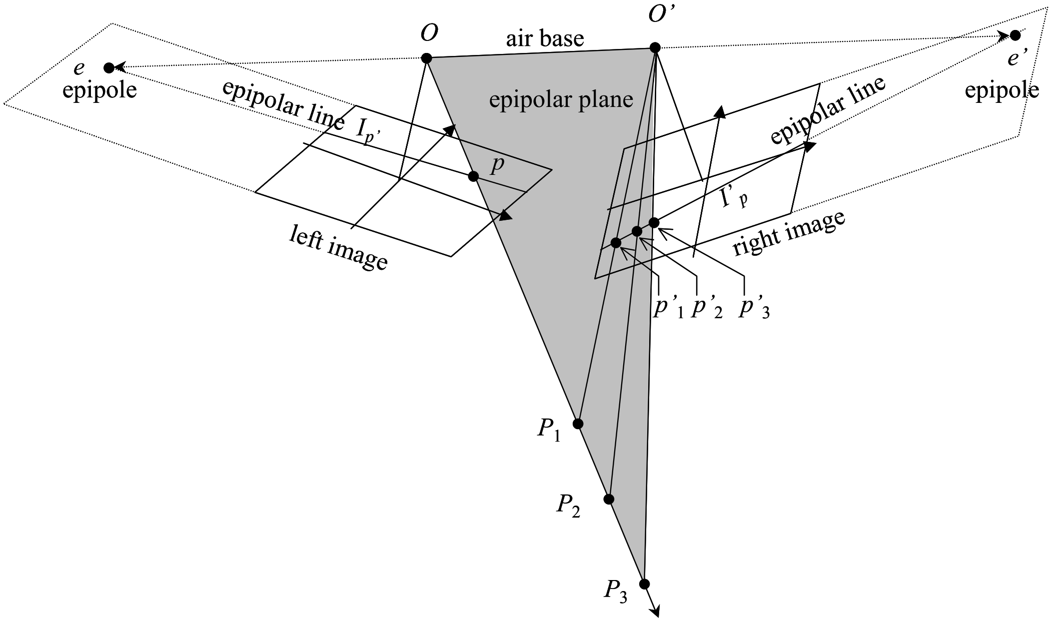

Figure 2.1: Epipolar geometry in frame images

Epipolar plane: The epipolar plane for a given image point *p* in one of the images is the plane that passes through the point *p* and both perspective centers, *O* and *O'*. Alternatively, it can be defined using the corresponding point in the object space and the two perspective centers.

Air base: The line connecting the perspective centers of the two images under consideration.

Epipoles: The intersections of the air base with the images themselves, or the planes that contain the images. As seen in Figure 2.1, *e* and *e'* are the epipoles of the given stereopair.

Epipolar line: The epipolar line can be defined in two ways. First, it can be defined as the intersection of the epipolar plane with the image, which produces a straight line (in frame images). Secondly, the epipolar line can be represented by the locus of all possible conjugate points of *p* on the other image. The latter definition is used in Section 2.3 when dealing with linear array scanners.

It should be noted that no DEM is needed to determine the epipolar line. This can be easily seen in Figure 2.1. Selecting several points along the ray (Op) - i.e., choosing different height values of the object point - will yield the same epipolar line ($I'p$) in the other image. The epipolar lines also pass through the epipoles as clearly seen in this figure.

Another important property of epipolar lines in frame images is their existence in conjugate pairs. Considering Figure 2.2, where I'_p is the epipolar line in the right image for point p in the left image, and p'_1, p'_2 are two different points in the right image selected on I'_p. The epipolar lines of points p'_1 and p'_2 ($I_{p'1}$ and $I_{p'2}$, respectively) will be identical and pass through the point p. Similarly, the epipolar line of any point, other than p'_1 or p'_2, lying on I'_p, will be identical to $I_{p'}$ and will pass through the point p. This can be easily seen in Figure 2.1, since all of these points and lines lie in the same plane (the epipolar plane).

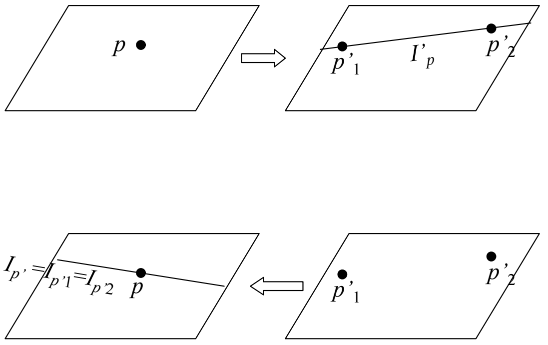

Figure 2.2: Epipolar line pairs

2.2.2 Determination of Epipolar Line in Frame Images

Generally, two methodologies can be adopted to determine the epipolar lines in frame images. Both methods rely on the knowledge of the EOP or at least the Relative Orientation Parameters (ROP) of the two frame images.

2.2.2.1 Method 1: Collinearity Equations Through the Object Space

The collinearity equations (Kraus, 1993), Equations 2.1, relate a point in the object space to its corresponding point in the image space; see Figure 2.3.

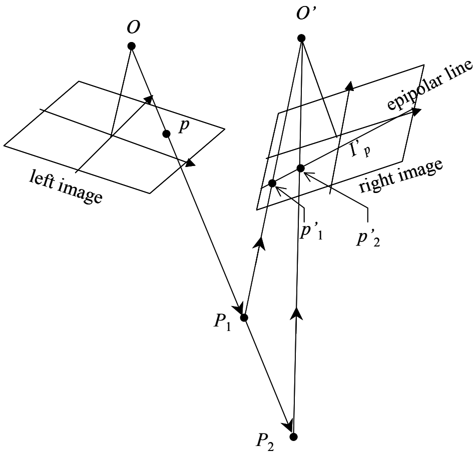

Figure 2.3: Determining the epipolar line by back-projecting points along the left light ray to the right image

$$\begin{bmatrix} X_j \\ Y_j \\ Z_j \end{bmatrix} = \begin{bmatrix} X_0 \\ Y_0 \\ Z_0 \end{bmatrix} + \frac{1}{\lambda_j} R_{(\omega,\varphi,\kappa)} \begin{bmatrix} x - x_0 \\ y - y_0 \\ -c \end{bmatrix} \tag{2.1}$$

Where:

x, y	are the image coordinates of a point of interest in the left image whose epipolar line to be determined in the right image;
x_0, y_0, c	are the IOP of the frame camera;
$X_0, Y_0, Z_0, \omega, \varphi, \kappa$	are the EOP of the left image;
X_j, Y_j, Z_j	are the object space coordinates of the corresponding object point;
λ_j	is the scale factor; and

$$R_{(\omega,\varphi,\kappa)} = \begin{bmatrix} r_{11} & r_{12} & r_{13} \\ r_{21} & r_{22} & r_{23} \\ r_{31} & r_{32} & r_{33} \end{bmatrix} = \begin{bmatrix} 1 & 0 & 0 \\ 0 & \cos\omega & -\sin\omega \\ 0 & \sin\omega & \cos\omega \end{bmatrix} \begin{bmatrix} \cos\varphi & 0 & \sin\varphi \\ 0 & 1 & 0 \\ -\sin\varphi & 0 & \cos\varphi \end{bmatrix} \begin{bmatrix} \cos\kappa & -\sin\kappa & 0 \\ \sin\kappa & \cos\kappa & 0 \\ 0 & 0 & 1 \end{bmatrix}$$

In Equations 2.1, there exist three equations and four unknowns. These unknowns are: the object space coordinates and the scale factor. Remember that the DEM, or the true elevation of the object point, is not required. The left light ray can be determined based only on the orientation parameters. Two different points are selected along that ray by choosing two different scale factors (λ_1, λ_2) and then solving Equations 2.1 independently for points (X_1, Y_1, Z_1) and (X_2, Y_2, Z_2). The appropriate values of (λ_1, λ_2) can be chosen in such a way so that the object space points represent the minimum and maximum elevation in the object space.

The two object points are then re-projected into the right image knowing its orientation parameters, by solving Equations 2.2 for the corresponding right image coordinates (x'_j, y'_j).

$$\begin{aligned} x'_j &= x_0 - c\frac{r'_{11}\left(X_j - X'_0\right) + r'_{21}\left(Y_j - Y'_0\right) + r'_{31}\left(Z_j - Z'_0\right)}{r'_{13}\left(X_j - X'_0\right) + r'_{23}\left(Y_j - Y'_0\right) + r'_{33}\left(Z_j - Z'_0\right)} \\ y'_j &= y_0 - c\frac{r'_{12}\left(X_j - X'_0\right) + r'_{22}\left(Y_j - Y'_0\right) + r'_{32}\left(Z_j - Z'_0\right)}{r'_{13}\left(X_j - X'_0\right) + r'_{23}\left(Y_j - Y'_0\right) + r'_{33}\left(Z_j - Z'_0\right)} \end{aligned} \tag{2.2}$$

Where:

X'_0, Y'_0, Z'_0, ω', φ', κ' are the EOP of the right image, and

$$R'_{(\omega',\varphi',\kappa')} = \begin{bmatrix} r'_{11} & r'_{12} & r'_{13} \\ r'_{21} & r'_{22} & r'_{23} \\ r'_{31} & r'_{32} & r'_{33} \end{bmatrix} = \begin{bmatrix} 1 & 0 & 0 \\ 0 & \cos\omega' & -\sin\omega' \\ 0 & \sin\omega' & \cos\omega' \end{bmatrix} \begin{bmatrix} \cos\varphi' & 0 & \sin\varphi' \\ 0 & 1 & 0 \\ -\sin\varphi' & 0 & \cos\varphi' \end{bmatrix} \begin{bmatrix} \cos\kappa' & -\sin\kappa' & 0 \\ \sin\kappa' & \cos\kappa' & 0 \\ 0 & 0 & 1 \end{bmatrix}$$

Points (x'_1, y'_1) and (x'_2, y'_2) form the epipolar line.

2.2.2.2 Method 2: Coplanarity Condition Without Visiting the Object Space

The object space point (X_j, Y_j , Z_j) is related to both the right and left images through Equations 2.3, where the object space coordinates are eliminated.

$$\begin{bmatrix} X_0 \\ Y_0 \\ Z_0 \end{bmatrix} + \frac{1}{\lambda_j} R_{(\omega,\varphi,\kappa)} \begin{bmatrix} x - x_0 \\ y - y_0 \\ -c \end{bmatrix} = \begin{bmatrix} X'_0 \\ Y'_0 \\ Z'_0 \end{bmatrix} + \frac{1}{\lambda'_j} R'_{(\omega',\varphi',\kappa')} \begin{bmatrix} x' - x_0 \\ y' - y_0 \\ -c \end{bmatrix} \tag{2.3}$$

Equations 2.3 represent three independent equations with four unknowns (λ_j, λ'_j, x', y'), which, after reduction, give the equation of the required epipolar line in the right image as a relation between (x', y').

Further reduction of the above equations by eliminating (λ_j, λ'_j) is similar to using the coplanarity condition (Kraus, 1993); see Equation 2.4 and Figure 2.4.

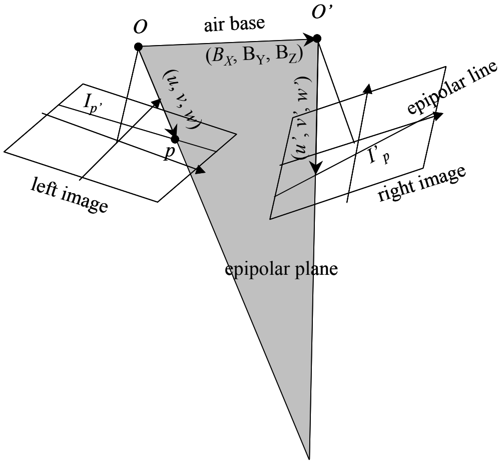

Figure 2.4: Coplanarity condition of vectors (B_X, B_Y, B_Z), (u, v, w) and (u', v', w')

$$\begin{vmatrix} B_x & B_y & B_z \\ u & v & w \\ u' & v' & w' \end{vmatrix} = 0 \tag{2.4}$$

Where:

$$\begin{bmatrix} u \\ v \\ w \end{bmatrix} = R_{(\omega,\varphi,\kappa)} \begin{bmatrix} x - x_0 \\ y - y_0 \\ -c \end{bmatrix},$$

$$\begin{bmatrix} u' \\ v' \\ w' \end{bmatrix} = R'(\omega', \varphi', \kappa') \begin{bmatrix} x' - x_0 \\ y' - y_0 \\ -c \end{bmatrix}, \text{ and}$$

$$\begin{bmatrix} B_X \\ B_Y \\ B_Z \end{bmatrix} = \begin{bmatrix} X'_0 \\ Y'_0 \\ Z'_0 \end{bmatrix} - \begin{bmatrix} X_0 \\ Y_0 \\ Z_0 \end{bmatrix} \text{ are the components of the air base.}$$

Expanding Equation 2.4 gives a linear relation between *x'* and *y'* (the epipolar line equation).

It is important to note that the epipolar lines of different points are not parallel in general. An exception is made for the case where the images are parallel to the air base. This is clear since all epipolar lines meet at the epipoles and the epipoles are at infinity; therefore, the epipolar lines will be parallel. In the following section, such an observation will be used for resampling the images to generate normalized images, in what is called "epipolar resampling".

2.2.3 Epipolar Resampling and Generation of Normalized Frame Images

This section introduces the objectives and the importance of the normalized images. The discussion begins by explaining the concept and derives the mathematical model for epipolar resampling. Finally, the procedure for epipolar resampling and generating the normalized images is introduced.

2.2.3.1 Objectives

The main objective of epipolar resampling is to generate normalized images, which have the innate property that corresponding points lie on the same rows (or columns). This prime advantage reduces the search space and computation time in addition to reducing matching ambiguities. This is important for a wide variety of applications such as:

- Automatic matching
- Automatic relative orientation
- Automatic aerial triangulation
- Automatic DEM generation
- Ortho-photo generation, and
- Stereo viewing

Figure 2.5 shows normalized stereo images, where point a in the left image has coordinates of (x_a, y_a). For normalized images, the search space for its conjugate a' in the right image will have a y' value equal to that of point a. Therefore, $y'_{a'} = y_a$. In this case, the search space of the corresponding point will be along the line $y' = y_a$. Similarly, for point b' in the right image, its conjugate in the left image, b, will be along the line $y = y'_{b'}$. For digital images, the search space for the conjugate point will be a row in the other image.

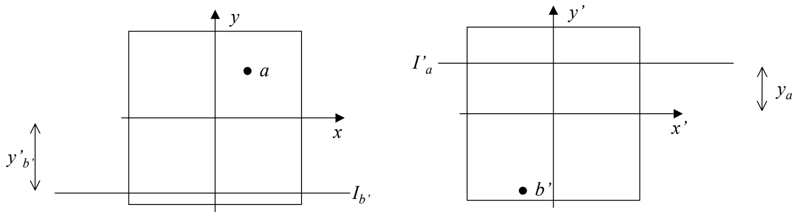

Left normalized image

Right normalized image

Figure 2.5: Normalized stereopair

2.1.3.2 Concept

As discussed earlier, resampling frame images requires that the new images be parallel to the air base. In this case, the epipolar lines in both images will be parallel. As seen in Figure 2.6, a new plane, parallel to the air base and containing the normalized images, can be used. It must be noted that there is no unique plane that will result in parallel epipolar lines. For example, two different planes that are parallel to the air base, each for resampling one of the images, results in parallel epipolar lines in each image independently. However, the spacing (normal distances) between the epipolar lines in one of the images will differ from the spacing between the corresponding points in the other image. In other words, the resulting images will have different scales. Therefore, the two images must be resampled to the same plane at a distance c_n from the air base, and not to two different parallel planes, as seen in Figure 2.6. In addition, there is an infinite number of planes that are parallel to the air base and that are at a distance, c_n , from it. These planes are tangent to the cylinder whose axis is the air base and radius is c_n. Therefore, rotation ω_n can be fixed to a certain value. Such a value can be chosen to be the average of ω and ω' of the left and right original images, respectively, in order to minimize possible scale distortions in the corresponding direction.

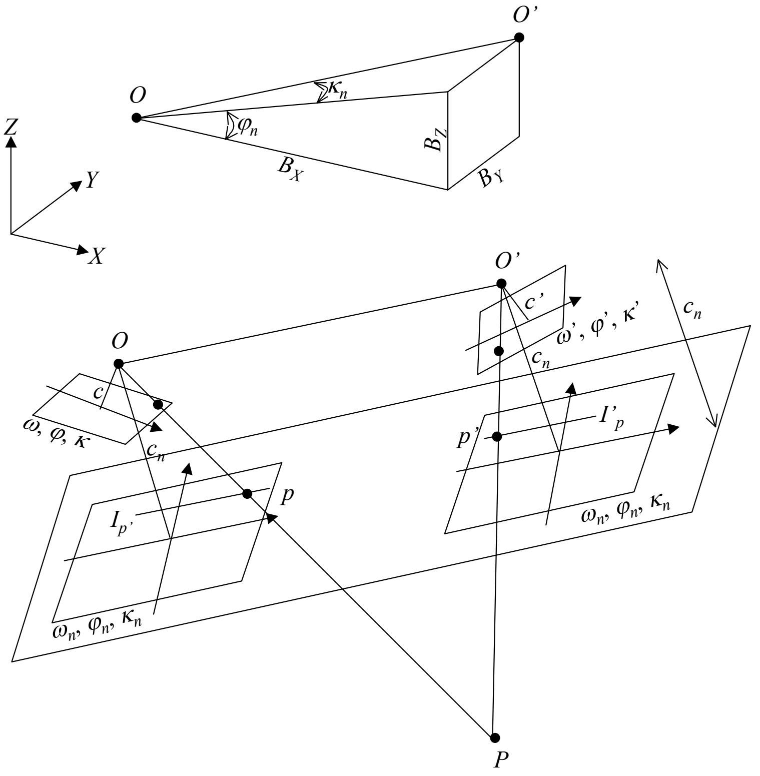

Figure 2.6: Concept of epipolar resampling and normalized images

One must note that the choice of IOP of the normalized images is arbitrary, but they should be equal in both left and right normalized images. For example, if the plane is chosen within a distance of c_n from the air base, the new normalized images will have a principal distance of c_n. However, it is preferred to use the same IOP values of the original images to obtain similar scales for both the original and normalized images.

Within the new image plane, both images must be rotated (κ rotation) to ensure that the corresponding points and epipolar lines lie along the same row (or column). Therefore, the EOP of the new images will be selected as follow:

- The perspective centers of the normalized images will be the same as those of the original images, $O(X_0, Y_0, Z_0)$ and $O'(X'_0, Y'_0, Z'_0)$.

- The orientations of the normalized images will be chosen as follows (Cho et al., 1992; Schenk, 1999):

  A primary rotation φ_n will be chosen in such a way to ensure that the new image plane is parallel to the air base; it can be computed as in Equation 2.5.

  $$\varphi_n = -\arctan\left(\frac{B_Z}{B_X}\right) \tag{2.5}$$

  A secondary rotation κ_n will be chosen so that the rows of the new images are parallel to the air base. It can be computed as in Equation 2.6.

  $$\kappa_n = \arctan\left(\frac{B_Y}{\sqrt{B_X^2 + B_Z^2}}\right) \tag{2.6}$$

  A tertiary rotation ω_n will be chosen in such a way as to minimize the scale distortion in the corresponding direction, and can be computed as in Equation 2.7.

  $$\omega_n = \frac{\omega + \omega'}{2} \tag{2.7}$$

  Therefore, the corresponding rotation matrix R_n is computed as follows:

  $$R_n = R_{\varphi_n} R_{\kappa n} R_{\omega n}$$

2.2.3.3 Mathematical Model

In this section, the mathematical model for transforming or resampling the image into a normalized one is derived. Consider any of the original images in Figure 2.6 - the left image for example. Its points must be transformed to the normalized image whose perspective center is identical to that of the original image, its orientations are as determined in Equations 2.5, 2.6, and 2.7, and having arbitrary IOP (x_{0n}, y_{0n}, c_n). Such a transformation is performed through the object space, as seen in Figure 2.7. In this figure, a profile of the images and the light ray are shown. Starting from the point in the original image, the collinearity equations or the equations of the light ray in space, can be written as:

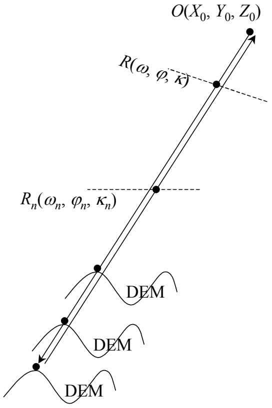

Figure 2.7: Tracing light ray from the original image to the object space, then to the normalized image

$$\begin{bmatrix} X \\ Y \\ Z \end{bmatrix} = \begin{bmatrix} X_0 \\ Y_0 \\ Z_0 \end{bmatrix} + \frac{1}{\lambda} R_{(\omega,\varphi,\kappa)} \begin{bmatrix} x - x_0 \\ y - y_0 \\ -c \end{bmatrix} \tag{2.8}$$

The same object space point (X, Y, Z) appears in the normalized image. Therefore, other collinearity equations, for the corresponding point in the normalized image, can be written as follows:

$$\begin{bmatrix} X \\ Y \\ Z \end{bmatrix} = \begin{bmatrix} X_0 \\ Y_0 \\ Z_0 \end{bmatrix} + \frac{1}{\lambda_n} R_{n(\omega_n,\varphi_n,\kappa_n)} \begin{bmatrix} x_n - x_{0n} \\ y_n - y_{0n} \\ -c_n \end{bmatrix} \tag{2.9}$$

Equating both Equations 2.8 and 2.9 results in:

$$\begin{aligned}\begin{bmatrix} x_n - x_{0n} \\ y_n - y_{0n} \\ -c_n \end{bmatrix} &= \lambda_n R_n{}^T{}_{(\omega_n,\varphi_n,\kappa_n)} \left(\begin{bmatrix} X_0 \\ Y_0 \\ Z_0 \end{bmatrix} + \frac{1}{\lambda} R_{(\omega,\varphi,\kappa)} \begin{bmatrix} x - x_0 \\ y - y_0 \\ -c \end{bmatrix} - \begin{bmatrix} X_0 \\ Y_0 \\ Z_0 \end{bmatrix} \right) \\ &= \frac{\lambda_n}{\lambda} R_n{}^T R \begin{bmatrix} x - x_0 \\ y - y_0 \\ -c \end{bmatrix}\end{aligned} \tag{2.10}$$

Equations 2.10 contain three equations in three unknowns (x_n, y_n, λ_n/λ). Therefore, x_n and y_n can be computed, regardless of the actual values of λ_n or λ. Before proceeding further, it is important to note that an object space point (or DEM) is not required in order to resample the frame image according to epipolar geometry. It can be seen from the above analysis that the actual values of λ_n or λ are not required. This can also be visualized by tracing the light rays in Figure 2.7, starting from the perspective center *O* to the point in the original image. This ray is extended till it hits the object space (or DEM). Then, the object space point is back-projected into the new normalized image. This ray should also pass through the perspective center of the normalized image, which is the same as that of the original image. Therefore, the two light rays - those projected into the object space and projected back from the object space - coincide. Therefore, regardless of where these light rays hit the object space (DEM), the same back-projected point in the normalized image is obtained. Thus, it can be concluded that a DEM is not required for epipolar resampling of frame images (as long as their perspective centers do not change). This discussion is important since it would be related/compared to scenes captured by line scanners.

The ratio λ_n/λ can be eliminated from Equations 2.10 by dividing the first and the second equations with the third one to give Equations 2.11, which are the mathematical functions that relate the coordinates in the original image to the corresponding coordinates in the normalized images.

$$\begin{aligned} x &= x_0 - c\frac{m_{11}(x_n - x_{0n}) + m_{21}(y_n - y_{0n}) + m_{31}(-c_n)}{m_{13}(x_n - x_{0n}) + m_{23}(y_n - y_{0n}) + m_{33}(-c_n)} \\ y &= y_0 - c\frac{m_{12}(x_n - x_{0n}) + m_{22}(y_n - y_{0n}) + m_{32}(-c_n)}{m_{13}(x_n - x_{0n}) + m_{23}(y_n - y_{0n}) + m_{33}(-c_n)} \end{aligned} \tag{2.11}$$

Where:

$$M = R_n^{\ T} R = \begin{bmatrix} m_{11} & m_{12} & m_{13} \\ m_{21} & m_{22} & m_{23} \\ m_{31} & m_{32} & m_{33} \end{bmatrix}$$

2.2.3.4 Procedure

The procedure for epipolar resampling and generating the normalized images can be summarized as follows (refer to Figure 2.8):

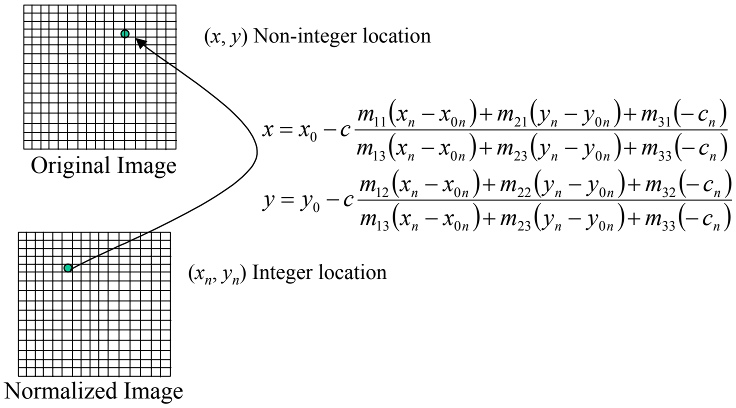

Figure 2.8: Procedure of epipolar resampling, or normalized image generation

1. Start from any pixel location in the normalized image (x_n, y_n).
2. Compute the corresponding location in the original image (x, y) using Equations 2.11. The values of x and y are usually non-integer.
3. Compute the gray value, $g(x, y)$, in the original image using an appropriate interpolation method such as nearest neighbor, bilinear interpolation or cubic convolution.

4. Assign the interpolated gray value to the pixel in the normalized image, i.e., $g(x_n,y_n)=g(x,y)$.
5. Repeat the above steps for all pixels in the normalized image.
6. Repeat the above steps for the other image in the stereopair.

2.3 LINEAR ARRAY SCANNERS

2.3.1 Introduction

Scenes captured from linear scanners (also called pushbroom scanners or line cameras) are valued for their great potential for generating ortho-photos and updating map databases (Wang, 1999). The linear scanners with up to one-meter resolution from commercial satellites could deliver more benefits and provide a challenge to traditional topographic mapping based on aerial images (Fritz, 1995). In this section, motivations for using linear array scanners are discussed. Scanner types and ways of stereo observation are also introduced. Finally, geometric modeling of linear array scanners together with their epipolar geometry are introduced.

2.3.1.1 Motivations for using Linear Array Scanners

Two-dimensional digital cameras capture data using a two-dimensional Charged Coupled Device (CCD) array. However, the limited number of pixels in current digital imaging systems hinders their application to extensive large scale mapping functions in comparison with scanned analog photographs. Increasing the principal distance of the 2-D digital cameras will increase the ground resolution, but will also decrease the ground coverage. On the other hand, decreasing the principal distance will increase the ground coverage at the expense of ground resolution.

One-dimensional digital cameras (linear array scanners) can be used to obtain large ground coverage and maintain a ground resolution comparable to scanned analog photographs. However, they capture only a one-dimensional image (narrow strip) per snapshot. Ground coverage and resolution in the scanning direction are achieved by the large number of pixels in the 1-D array (see Figure 2.9). On the other hand, successive ground coverage in the flying direction is achieved by moving the sensor (airborne or space-borne) and capturing more 1-D images. The ground resolution in the flying direction can be maintained by synchronizing the scanning frequency and the speed of the platform. The scene of an area of interest is obtained by stitching together the resulting 1-D images. It is important to note that every 1-D image is associated with one combination of exposure station and scanner orientations at the time of exposure. Therefore, each 1-D image will have a distinct set of EOP. A clear distinction is made herein between the two terms "scene" and "image" throughout the analysis of linear array scanners. Before proceeding, one has to note that the technology is evolving with a high speed. This leads to increase in the number of pixels of the 2-D cameras as well as the 1-D scanners. However, the latter can always achieve larger number of pixels compared to the number of rows or columns in 2-D cameras.

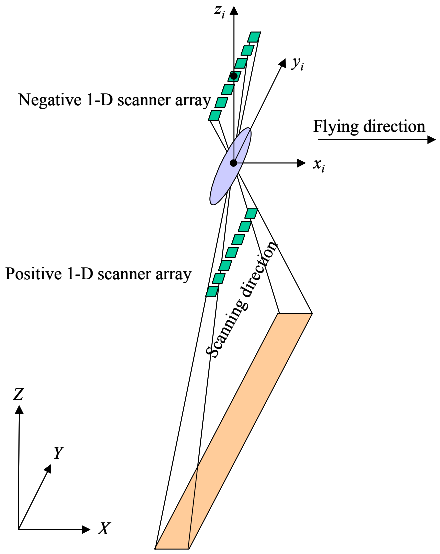

Figure 2.9: Linear array scanner

2.3.1.2 Differences between Image and Scene

An **image** is defined as the recorded sensory data associated with one exposure station. In the case of a frame image, it contains only one exposure station, and consequently it is one complete image. In the case of a linear array scanner, there are many 1-D images, each associated with different exposure stations. The mathematical model that relates a point in the object space and its corresponding point in the image space is contained in the collinearity equations, which use the EOP of the appropriate image (in which the point appears).

By way of contrast, a **scene** is the recorded sensory data associated with one (as in frame images) or more exposure stations (as in linear array scanners) that maps near-continuous object space in a single short trip of the sensor. Therefore, in frame images, the image and scene are identical terms while, in linear array scanners, the scene is an array of consecutive 1-D images.

Consequently, it is important to distinguish between the scene coordinates and image coordinates. As shown in Figure 2.10, i and y are the scene coordinates while x_i and y_i are the image coordinates for image number i. Only x_i and y_i can be used in the collinearity equations, while i indicates the image number or the time of exposure.

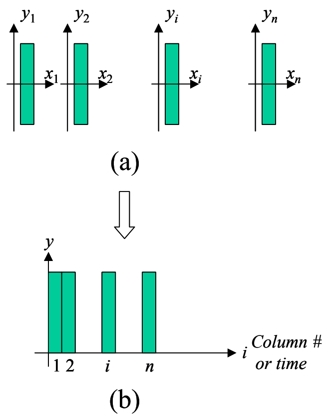

(a)

(b)

Figure 2.10: A sequence of 1-D images (a) consisting a scene (b)

2.3.1.3 Types of Linear Array Scanner Systems

A linear array scanner system may be comprised of one or more 1-D scanners in the image plane. Figure 2.9 shows an example of one linear array scanner system and Figure 2.11 shows a three-line camera. The latter system has three linear array scanners, scanning in three different directions: backward, nadir, and forward-looking. As the platform moves, each of the scanners captures a different scene in the corresponding direction. Another type, panoramic linear array scanners, are used to capture a large swath normal to the flying direction (Habib and Beshah, 1998a). Due to the large scale differences within the captured scenes, this system will not be included in the analysis that follows. The various systems achieve stereo coverage differently by different means, as will be explained in the next subsection.

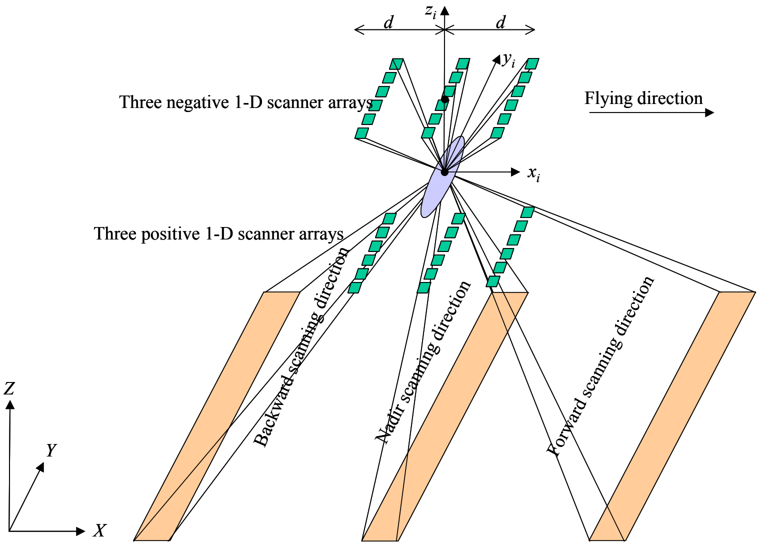

Figure 2.11: Three-line camera

2.3.1.4 Stereo Coverage

One of the main objectives of photogrammetry is to reconstruct the three-dimensional object space from 2-D images or scenes. This is usually achieved by intersecting light rays of corresponding points in different views. Therefore, different views or stereo coverage are essential for deriving 3D information regarding the object space. In linear array scanners, stereo coverage can be achieved in each of the following ways:

- One scanner and across-track stereo coverage using roll angles

Stereo coverage can be achieved by tilting the camera sideways across the flight direction to produce different roll angles (see Figure 2.12a). This has been adopted in SPOT (Fraser et al., 2001). A drawback of this type is the large time gap between the images of the stereopair, and consequently changes may occur between the two scenes (Wang, 1999). In addition, large radiometric differences may occur between the recorded scenes and cause problems in image matching.

- One scanner and along track stereo coverage using pitch angles

In this case the camera is tilted forward and backward along the flight direction to produce different pitch angles (see Figure 2.12b). This type of stereo coverage is used in IKONOS (Fraser et al., 2001). This method has the advantage of reducing the time gap between the scenes comprising the stereopair and consequently reducing the radiometric or geometric differences between them.

- Three scanners (three-line camera)

In this case, three scanners are used to capture backward-looking, nadir, and forward-looking scenes, producing different x_i values (see Figure 2.12c). Continuous stereo or triple coverage can be achieved along the flight line with reduced time gaps. Similar scales are achieved for the three scenes generated by the scanners. However, different radiometric qualities exist among the scenes, which may cause problems in image matching. This method is implemented in MOMS and ADS40 (Heipke et al., 1996; Sandau et al., 2000; Fraser et al., 2001).

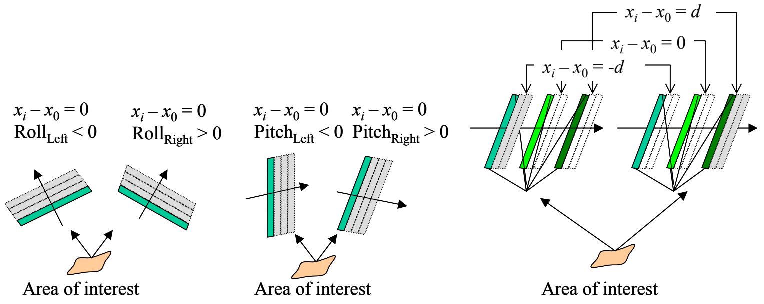

(a) (b) (c)

Figure 2.12: Stereo coverage in linear array scanners achieved by roll angle rotation in two flying paths (a), pitch angle rotation in the same flying path (b), and three-line camera (c)

A final significant characteristic is that ($x_i - x_0$) is always constant, as shown in Figures 2.9 to 2.12. It is always zero except for the backward and forward scanners in the three-line camera where it has the values of $-d$ and d, respectively, where d is the spacing between the scanners in the focal plane.

2.3.2 Modeling of Linear Array Scanners

The rigorous and generalized sensor models are the two broad categories of sensor models in use (McGlone, 1996). These are briefly discussed in the following subsections.

2.3.2.1 Rigorous Model

Rigorous (or exact) modeling of linear array scanners describes the actual geometric formation of the scenes at the time of photography. This modeling requires a knowledge of the IOP of the scanner and the EOP of each image in the scene. Usually, EOP do not abruptly change their values between consecutive images in a scene, especially for space-based scenes. Therefore, most rigorous modeling methods adopt a polynomial representation of EOP (Wang, 1999; Lee et al., 2000); see Equations 2.12:

$$
\begin{aligned}
X_{0i} &= X_0 + \Delta X\, i + \ldots + \Delta X_{nX}\, i^{nX} \\
Y_{0i} &= Y_0 + \Delta Y\, i + \ldots + \Delta Y_{nY}\, i^{nY} \\
Z_{0i} &= Z_0 + \Delta Z\, i + \ldots + \Delta Z_{nZ}\, i^{nZ} \\
\omega_i &= \omega + \Delta\omega\, i + \ldots + \Delta\omega_{n\omega}\, i^{n\omega} \\
\varphi_i &= \varphi + \Delta\varphi\, i + \ldots + \Delta\varphi_{n\varphi}\, i^{n\varphi} \\
\kappa_i &= \kappa + \Delta\kappa\, i + \ldots + \Delta\kappa_{n\kappa}\, i^{n\kappa}
\end{aligned}
\tag{2.12}
$$

Where:

i	is the image number (which is directly related to the time of exposure);
(X_{0i}, Y_{0i}, Z_{0i})	are the spatial location of the exposure station of image i;
$(\omega_i, \varphi_i, \kappa_i)$	are the rotation angles of image i;
(nX, nY, nZ)	are the degrees of the polynomials of X_{0i}, Y_{0i} and Z_{0i}, respectively;
$(n\omega, n\varphi, n\kappa)$	are the degrees of the polynomials of ω_i, φ_i and κ_i, respectively;
(X_0, Y_0, Z_0)	are the spatial location of the exposure station of the first image in the scene (image 0);
$(\Delta X, \Delta Y, \Delta Z)$	are the linear changes of scanner location (components of the scanner velocity vector – the first order components of the scanner location);
$(\Delta X_{nX}, \Delta Y_{nY}, \Delta Z_{nZ})$	are the nX^{th}, nY^{th} and nZ^{th} order components, respectively, of the scanner location;
$(\omega, \varphi, \kappa)$	are the rotation angles of the first image in the scene;
$(\Delta\omega, \Delta\varphi, \Delta\kappa)$	are the linear changes of the rotation angles (the first order components of the scanner rotation angles); and
$(\Delta\omega_{n\omega}, \Delta\varphi_{n\varphi}, \Delta\kappa_{n\kappa})$	are the $n\omega^{\text{th}}$, $n\varphi^{\text{th}}$ and $n\kappa^{\text{th}}$ order components, respectively, of the scanner rotation angles.

It is important to note that the order of each polynomial may differ from those of the other polynomials. In other words, values of nX, nY , nZ, $n\omega$, $n\varphi$ and $n\kappa$ may differ, depending of the scanner movement pattern. Their typical values are therefore scanner-dependent. The parameters included in Equation 2.12 are either given (directly) from the navigation units such as GPS and INS sensors mounted on the platform, or indirectly estimated using ground control in bundle adjustment (Habib and Beshah, 1998; Habib et al., 2001; Lee and Habib, 2002).

Other methods (Ethridge, 1977; McGlone and Mikhail, 1981; Lee et al., 2000) use piecewise polynomial modeling to represent the flight trajectory and the platform attitude. This option is preferable if the scene time is large, and the variations in EOP do not comply with one set of polynomial functions.

With the large number of unknowns in indirect methods using Ground Control Points (GCP), instability in the bundle adjustment exists, especially for space-based scenes (Wang, 1999; Fraser et a., 2001). This is attributed to the narrow Angular Field of View (AFOV) of space scenes, which results in very narrow bundles in the adjustment procedures.

Finally, Lee and Habib (2002) avoided the polynomial representation of EOP, by explicitly considering the parameters of each image in the scene. Linear feature constraints were used to aid independent recovery of the EOP of the images as well as to increase the geometric strength of the bundle adjustment.

2.3.2.2 Generalized Models

Generalized sensor models represent an approximate transformation between the scene and object coordinates and do not necessarily represent the exact transformation. Therefore, they can be considered as approximate models. These sensor models can be used as a generic solution for all sensor types (Paderes et al., 1989; Tao and Hu, 2001; Grodecki and Dial, 2003). This class of models includes rational functions, such as DLT, SDLT, and 2-D Affine, which will be introduced in the following subsections.

2.3.2.2.1 Rational Functions

Recently, the US military intelligence community has initiated the use of the rational function model. They have been implemented in some commercial software packages (Madani, 1999; Dowman and Dolloff, 2000). It is important to note that some satellite scene providers do not provide the IOP associated with their scanners or EOP associated with their scenes for security reasons (Fraser et al., 2001). Some satellite scenes are provided nowadays with generalized models, such as rational function models, describing the relation between scene and object coordinates. A general form of the rational functions can be written in Equations 2.13.

$$\begin{aligned} x &= \frac{F_1^r(X,Y,Z)}{F_2^r(X,Y,Z)} \\ y &= \frac{F_3^r(X,Y,Z)}{F_4^r(X,Y,Z)} \end{aligned} \qquad (2.13)$$

where F_i^r is a polynomial function of r-degree of the object coordinates (X, Y, Z). Equations 2.13 represent a forward transformation from the object coordinates to the scene coordinates. The degree of the polynomial is the maximum summation of the powers of the object coordinates. For example, in a third-degree polynomial such as $\sum_k C_k X^a Y^b Z^b$, the summation of a, b and c should not exceed three. An alternative representation, the backward representation, can be seen in Equations 2.14, where the object planimetric coordinates are rational functions of the elevation and the scene coordinates.

$$\begin{aligned} X &= \frac{B_1^r(x,y,Z)}{B_2^r(x,y,Z)} \\ Y &= \frac{B_3^r(x,y,Z)}{B_4^r(x,y,Z)} \end{aligned} \qquad (2.14)$$

Where B_i^r (x, y, Z) is an r-degree polynomial. The denominators in each expression may be the same or different. For example, F_2^r and F_4^r in Equations 2.13 – or B_2^r and B_4^r in Equations 2.14 - could have identical or different coefficients).

Similar to the case of rigorous modeling, the rational functions' parameters can be determined directly (using scanner IOP and EOP) or indirectly using control information (Tao and Hu, 2001).

It is important to mention that directly determined rational functions' parameters are subject to biases in the scanner's IOP or EOP (Baltsavias et al., 2001; Fraser et al., 2001; Hanley et al., 2002; Fraser and Hanley, 2003). Therefore, indirectly determining these coefficients is preferable for the achievement of increased absolute accuracy. On the other hand, many GCPs are required to indirectly determine these parameters (Tao and Hu, 2001), which therefore limits the use of rational functions, especially in remote areas.

2.3.2.2.2 Direct Linear Transformation (DLT)

The collinearity equations (Equations 2.1) can be rewritten so that the image coordinates are rational functions of the object coordinates (Abdel-Aziz and Karara, 1971):

$$
\begin{aligned}
x &= \frac{A_1 X + A_2 Y + A_3 Z + A_4}{1 + A_9 X + A_{10} Y + A_{11} Z} \\
y &= \frac{A_5 X + A_6 Y + A_7 Z + A_8}{1 + A_9 X + A_{10} Y + A_{11} Z}
\end{aligned}
\tag{2.15}
$$

where A_1, …, A_{11} are the DLT parameters. It is important to note that DLT consists of first-degree forward rational functions with common denominators. Therefore, these parameters can be obtained directly (using IOP and EOP) or indirectly (using GCP). Although DLT can be considered as the rigorous model of frame images, it is considered as approximate modeling of linear array scanners, since the EOP are no longer the same for images in the scene.

Wang (1999) developed self-calibrating DLT, referred to as the SDLT, which includes an additional parameter, A_{12}, representing additional correction to the image coordinates:

$$\begin{aligned} x &= \frac{A_1X + A_2Y + A_3Z + A_4}{1 + A_9X + A_{10}Y + A_{11}Z} \\ y - A_{12}xy &= \frac{A_5X + A_6Y + A_7Z + A_8}{1 + A_9X + A_{10}Y + A_{11}Z} \end{aligned} \tag{2.16}$$

Importantly, Wang assumed a straight line trajectory with constant heading in his derivation.

2.3.2.2.3 Two-D Affine Model

For scanners with a narrow AFOV and moving with constant-velocity and constant attitude, the relationship between the scene and object coordinates can be approximated by a 2-D Affine transformation (Equations 2.17) using fewer parameters (Ono et al., 1999; Fraser, 2000). This characteristic makes it appealing to many researchers and applications (Okamoto, 1992; and Okamoto et al., 1992; Okamoto et al., 1996; Ono et al., 1996; Okamoto and Fraser, 1998; Ono et al., 1999; Fraser, 2000; Hattori et al., 2000; Ono et al., 2000).

$$\begin{aligned} x &= A_1X + A_2Y + A_3Z + A_4 \\ y &= A_5X + A_6Y + A_7Z + A_8 \end{aligned} \tag{2.17}$$

Fraser et al. (2001) achieved sub-pixel accuracy using the 2-D Affine model for IKONOS scenes. Therefore, this model will be closely investigated in Chapter 4. Achievement of such a level of accuracy motivates the use of this type of model for space scenes. However, it is important to mention that such accuracies are achieved under the assumption of high-quality image mensuration and ground control, and favorable imaging geometry (Hanley and Fraser, 2001; Fraser et al., 2001; Fraser et al., 2002).

It is important to mention that raw scenes obtained from linear array scanners comply with perspective geometry. Therefore, prior to using the model in Equations 2.17, a perspective-to-affine transformation must be applied to transform the scenes from their original state, as a perspective projection, to a 2-D Affine model (Okamoto et al., 1992; Okamoto et al., 1996; Okamoto and Fraser, 1998; Ono et al., 1999; Hattori et al., 2000; Ono et al., 2000). Such a transformation assumes flat terrain or a DEM and assumes a knowledge of the scanner roll angle. Chapter 5 of this dissertation is dedicated to the analysis of this transformation together with developing the relationship between the rigorous model and the parallel projection parameters.

2.3.3 Epipolar Geometry of Linear Array Scanner Scenes

As discussed earlier, every scan line at each different exposure station has a different perspective center and attitude. Therefore, the EOP will vary from one scan line to another. Hence, the epipolar lines should be clearly defined in such scenes before studying their geometry. Figure 2.13 shows a schematic drawing of two linear array scanner scenes. For a 1-D image in the left scene with *O* as its perspective center, point *p* can correspond to many epipolar planes, unlike the case of frame images - compare Figures 2.1 and 2.13. In this case, there are as many epipolar planes as there are perspective centers in the right scene. Therefore, the epipolar line cannot be defined as the intersection of planes. Instead, the second definition used in frame images is adopted, where the epipolar line is defined as **the locus of all possible conjugate points of *p* in the other scene based on the orientation parameters**.

In order to determine the epipolar line, the EOP of the scan lines together with the IOP of the scanner must be available. The epipolar line can be determined in a similar manner to that discussed in Section 2.2.2 by repeating the procedure for each scan line, since each scan line has different EOP. The change in EOP from one scan line to the next is one of the factors that determine the shape of the epipolar line. Subsections 2.3.3.1 and 2.3.3.2

analyze the shape of epipolar lines derived from the rigorous perspective model and from the 2-D Affine model, respectively.

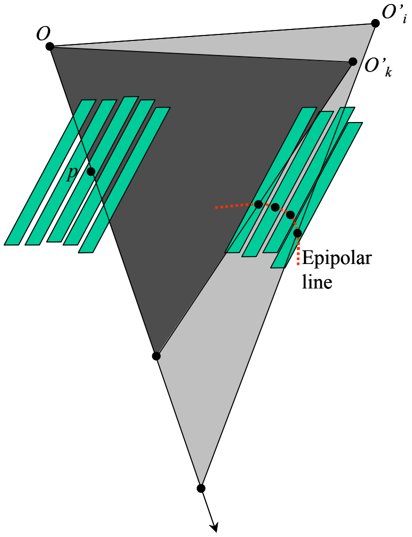

Figure 2.13: Epipolar line in linear array scanner scenes

2.3.3.1 Epipolar Line Determination using the Rigorous Model

Kim (2000) originated this determination by modeling the changes of EOP, as expressed in Equations 2.18. This model is called the "Orun and Natarajan" model as cited from Orun and Natarajan (1994). The author indicated the suitability of the model for describing the EOP of SPOT scenes.

$$\begin{aligned}
&X_{0j} = X_0 + \Delta X\ j + \Delta X_2\ j^2 \\
&Y_{0j} = Y_0 + \Delta Y\ j + \Delta Y_2\ j^2 \\
&Z_{0j} = Z_0 + \Delta Z\ j + \Delta Z_2\ j^2 \\
&\kappa_j = \kappa + \Delta\kappa\ j + \Delta\kappa_2\ j^2 \\
&\omega_j = \omega \\
&\varphi_j = \varphi \\
&X'_{0i} = X'_0 + \Delta X'\, i + \Delta X'_2\ i^2 \\
&Y'_{0i} = Y'_0 + \Delta Y'\, i + \Delta Y'_2\ i^2 \\
&Z'_{0i} = Z'_0 + \Delta Z'\, i + \Delta Z'_2\ i^2 \\
&\kappa'_i = \kappa' + \Delta\kappa'\, i + \Delta\kappa'_2\ i^2 \\
&\omega'_i = \omega' \\
&\varphi'_i = \varphi'
\end{aligned} \tag{2.18}$$

where *j* and *i* are the scan lines in the left and right scene, respectively.

The author proved the relation that expresses the epipolar line, as indicated in Equation 2.19. The notations are modified to eliminate any conflict with those used in this dissertation, especially in the analysis of the epipolar geometry presented in Chapter 3.

$$y' = \frac{K_1 j + K_2 y + K_3}{(K_4 j + K_5 y + K_6)\sin Q(i) + (K_7 j + K_8 y + K_9)\cos Q(i)} \tag{2.19}$$

where:

y	is the point in the left scene, along the j^{th} scan line, whose epipolar line to be determined;
y'	is the corresponding point in the right scene, as a function of the scan line i;
K_1 to K_9	are constants for a given scan line j in the left scene; and
$Q(i)$	is a quadratic function of i associated with yaw angle variation of the right sensor.

From Equation 2.19, the relation between *y'* and *i* is no longer a straight line; rather, its shape is hyperbola-like. Kim (2000) continued by analyzing the existence of conjugate epipolar lines in SPOT scenes. He selected two different points (p'_1 and p'_2) on the right epipolar line (I'_p). The left epipolar lines ($I_{p'1}$ and $I_{p'2}$) of the selected points were not identical, as shown in Figure 2.14. Therefore, the commonly known term "epipolar pairs" does not exist for a linear array scene whose EOP are modeled as in Equations 2.19.

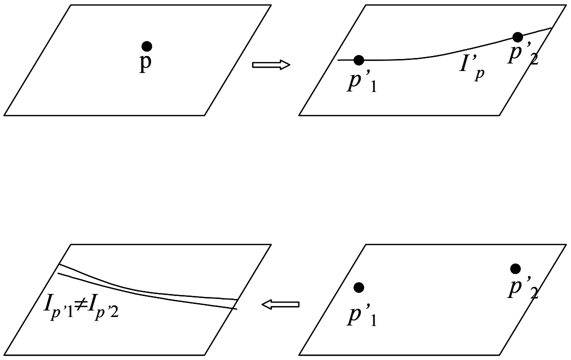

Figure 2.14: The nonexistence of conjugate epipolar lines in linear array scenes whose EOP are similar to those of the Orun and Natarajan model

In Chapter 3, a different model (the constant-velocity-constant-attitude model) will be analyzed and the resulting epipolar line equation will be developed.

2.3.3.2 Epipolar Geometry using 2-D Affine Model

Ono et al. (1999) derived the equation for epipolar lines, Equation 2.21, using the 2-D Affine model.

$$y' = C_1 x' + C_2 x + C_3 y + C_4 \tag{2.21}$$

Where C_1 to C_4 are the epipolar line parameters determined using point correspondences in both scenes. Equation 2.21 represents a straight line. Having straight epipolar lines motivates us to investigate the parallel projection model very closely (as done in Chapter 4) and its use in epipolar resampling (Chapter 6).

2.4 SUMMARY

This chapter presented a discussion of the epipolar geometry of frame images as reported in the literature. Of importance in this field are the facts that epipolar lines in frame images are straight lines, and neither epipolar line determination nor epipolar resampling require any knowledge of DEM.

Linear array scanners were also introduced in Chapter 2, including different methods for their geometric modeling. Epipolar lines in linear array scanners were found to be non-straight lines using Orun and Natarajan’s EOP model. As it is desirable to obtain a straight epipolar curve, a subclass of this EOP model is chosen for analysis in Chapter 3.

Finally, the 2-D Affine (or the parallel projection) model is found to produce straight epipolar lines. Therefore, such a model will be investigated for the purpose of epipolar resampling of linear array scanner scenes (Chapters 4 to 6).

CHAPTER 3: EPIPOLAR LINES OF CONSTANT-VELOCITY-CONSTANT-ATTITUDE LINEAR ARRAY SCANNERS

3.1 INTRODUCTION

In Chapter 2, the epipolar geometry of linear array scanners of the “Orun and Natarajan” EOP model were investigated and it was concluded that epipolar lines are not straight lines (Kim, 2000). This chapter establishes the epipolar line equation of linear array scanners using the constant-velocity-constant-attitude EOP model, which is a subclass of “Orun and Natarajan.” To the best of the author’s knowledge, there has been no prior research in this area. The motivation for investigating such a model stems from the fact that many space scenes are acquired within a very short time (e.g., about one second for IKONOS scene); similar assumptions were made for EOP when deriving the SDLT model for linear array scanners (Wang, 1999). The scanner, therefore, can be assumed to travel with constant velocity and constant attitude during the scene capture. Section 3.2 is dedicated to the analysis of this EOP model, followed by a presentation of experimental results using synthetic data in Section 3.3.

3.2 CONSTANT-VELOCITY-CONSTANT-ATTITUDE EOP MODEL

Assuming a linear transition of the platform having constant speed and attitude, the navigation parameters (EOP for any scan line) of the sensor during the capture of the left and right scene are as expressed as in Equations 3.1.

$$
\begin{aligned}
&X_{0j} = X_0 + \Delta X\ j \\
&Y_{0j} = Y_0 + \Delta Y\ j \\
&Z_{0j} = Z_0 + \Delta Z\ j \\
&\kappa_j = \kappa \\
&\omega_j = \omega \\
&\varphi_j = \varphi \\
\\
&X'_{0i} = X'_0 + \Delta X'\, i \\
&Y'_{0i} = Y'_0 + \Delta Y'\, i \\
&Z'_{0i} = Z'_0 + \Delta Z'\, i \\
&\kappa'_i = \kappa' \\
&\omega'_i = \omega' \\
&\varphi'_i = \varphi'
\end{aligned}
\tag{3.1}
$$

Where:

j	is the scan line number on the left scene;
i	is the scan line number on the right scene;
(X_0, Y_0, Z_0)	is the position of the first exposure station in the left scene;
$(\Delta X, \Delta Y, \Delta Z)$	is the constant velocity vector of the scanner while capturing the left scene;
(X'_0, Y'_0, Z'_0)	is the position of the first exposure station in the right scene;
$(\Delta X', \Delta Y', \Delta Z')$	is the constant velocity vector of the scanner while capturing the right scene;
$(\omega, \varphi, \kappa)$	are the rotation angles of the left scanner; and
$(\omega', \varphi', \kappa')$	are the rotation angles of the right scanner.

For a point (j, y_j) in the left scene, the collinearity equations can be written as:

$$
\begin{bmatrix} X - X_{0j} \\ Y - Y_{0j} \\ Z - Z_{0j} \end{bmatrix} = \frac{1}{\lambda_j} R_{j(\omega_j, \varphi_j, \kappa_j)} \begin{bmatrix} x - x_0 \\ y_j - y_0 \\ -c \end{bmatrix}
\tag{3.2}
$$

As mentioned in Chapter 2, ($x_i - x_0$) is always constant. It is always zero, except for the backward and forward scanners in a three-line camera where it is $-d$ and d, respectively. In addition, x_0 is constant for the scanner as it is the principal point's x-coordinate. As a result, x_i is always constant. It is always equal to x_0, except for the backward and forward scanners in three-line cameras where it is x_0-d and x_0+d, respectively. Therefore, x is used in lieu of x_i in the following derivations. Equations 3.2 can be rewritten as:

$$\begin{aligned} \frac{X - X_{0j}}{Z - Z_{0j}} &= \frac{r_{j11}(x - x_0) + r_{j12}(y_j - y_0) + r_{j13}(-c)}{r_{j31}(x - x_0) + r_{j32}(y_j - y_0) + r_{j33}(-c)} \\ \frac{Y - Y_{0j}}{Z - Z_{0j}} &= \frac{r_{j21}(x - x_0) + r_{j22}(y_j - y_0) + r_{j23}(-c)}{r_{j31}(x - x_0) + r_{j32}(y_j - y_0) + r_{j33}(-c)} \end{aligned} \tag{3.3}$$

Where:

$$R_{j(\omega_j,\varphi_j,\kappa_j)} = \begin{bmatrix} r_{j11} & r_{j12} & r_{j13} \\ r_{j21} & r_{j22} & r_{j23} \\ r_{j31} & r_{j32} & r_{j33} \end{bmatrix}$$

Rearranging and separating the constants and the parameters in Equations 3.3 results in:

$$\begin{aligned} X &= \left[\frac{r_{j11}(x - x_0) + r_{j12}(y_j - y_0) + r_{j13}(-c)}{r_{j31}(x - x_0) + r_{j32}(y_j - y_0) + r_{j33}(-c)}\right] Z \\ &\quad + \left[X_{0j} - Z_{0j} \frac{r_{j11}(x - x_0) + r_{j12}(y_j - y_0) + r_{j13}(-c)}{r_{j31}(x - x_0) + r_{j32}(y_j - y_0) + r_{j33}(-c)}\right] \\ Y &= \left[\frac{r_{j21}(x - x_0) + r_{j22}(y_j - y_0) + r_{j23}(-c)}{r_{j31}(x - x_0) + r_{j32}(y_j - y_0) + r_{j33}(-c)}\right] Z \\ &\quad + \left[Y_{0j} - Z_{0j} \frac{r_{j21}(x - x_0) + r_{j22}(y_j - y_0) + r_{j23}(-c)}{r_{j31}(x - x_0) + r_{j32}(y_j - y_0) + r_{j33}(-c)}\right] \end{aligned} \tag{3.4}$$

It is important to note that, for a given point, y_j is constant; for a given image, the rotation matrix R_j is constant; and for a given camera, x_0, y_0 and c are constants. Therefore, the following constant terms (A_1 to A_4) can be introduced:

$$
\begin{aligned}
A_1 &= \frac{r_{j11}(x-x_0)+r_{j12}(y_j-y_0)+r_{j13}(-c)}{r_{j31}(x-x_0)+r_{j32}(y_j-y_0)+r_{j33}(-c)} \\
A_2 &= X_{0j}-Z_{0j}\frac{r_{j11}(x-x_0)+r_{j12}(y_j-y_0)+r_{j13}(-c)}{r_{j31}(x-x_0)+r_{j32}(y_j-y_0)+r_{j33}(-c)} = X_{0j}-Z_{0j}A_1 \\
A_3 &= \frac{r_{j21}(x-x_0)+r_{j22}(y_j-y_0)+r_{j23}(-c)}{r_{j31}(x-x_0)+r_{j32}(y_j-y_0)+r_{j33}(-c)} \\
A_4 &= Y_{0j}-Z_{0j}\frac{r_{j21}(x-x_0)+r_{j22}(y_j-y_0)+r_{j23}(-c)}{r_{j31}(x-x_0)+r_{j32}(y_j-y_0)+r_{j33}(-c)} = Y_{0j}-Z_{0j}A_3
\end{aligned}
\tag{3.5}
$$

Accordingly, Equations 3.4 are rewritten as:

$$
\begin{aligned}
X &= A_1.Z + A_2 \\
Y &= A_3.Z + A_4
\end{aligned}
\tag{3.6}
$$

which represent two planes parallel to the *Y* and *X* axes, respectively. Their intersection is a straight-line (a light ray in space). On the other hand, for the right scene, the collinearity equations are:

$$
\begin{bmatrix} x'-x_0 \\ y'_i-y_0 \\ -c \end{bmatrix} = \lambda'_i \, R'^{T}_{i(\omega'_i,\varphi'_i,\kappa'_i)} \begin{bmatrix} X-X'_{0i} \\ Y-Y'_{0i} \\ Z-Z'_{0i} \end{bmatrix}
\tag{3.7}
$$

Recall again that *x'* is constant, and it is equal to *x* if the same scanner is used to acquire both the left and right scenes (Section 2.3.1.4). Using EOP from Equations 3.1, Equations 3.7 can be written as:

$$\begin{bmatrix} x'-x_0 \\ y'_i-y_0 \\ -c \end{bmatrix} = \lambda'_i \, R'^{T}_{i(\omega'_i,\varphi'_i,\kappa'_i)} \begin{bmatrix} X-X'_0-\Delta X' i \\ Y-Y'_0-\Delta Y' i \\ Z-Z'_0-\Delta Z' i \end{bmatrix}$$

$$= \lambda'_i \, R'^{T}_{i(\omega'_i,\varphi'_i,\kappa'_i)} \begin{bmatrix} A_1.Z+A_2-X'_0-\Delta X' i \\ A_3.Z+A_4-Y'_0-\Delta Y' i \\ Z-Z'_0-\Delta Z' i \end{bmatrix} \tag{3.8}$$

$$= \lambda'_i \, R'^{T}_{i(\omega'_i,\varphi'_i,\kappa'_i)} \left(Z \begin{bmatrix} A_1 \\ A_3 \\ 1 \end{bmatrix} - i. \begin{bmatrix} \Delta X' \\ \Delta Y' \\ \Delta Z' \end{bmatrix} + \begin{bmatrix} A_2-X'_0 \\ A_4-Y'_0 \\ -Z'_0 \end{bmatrix} \right)$$

Dividing the first two equations by the last results in the following equations:

$$\frac{x'-x_0}{-c} = \frac{Z(r'_{i11}.A_1+r'_{i21}.A_3+r'_{i31})-i(r'_{i11}.\Delta X'+r'_{i21}.\Delta Y'+r'_{i31}.\Delta Z')+(r'_{i11}.A_2-r'_{i11}.X'_0+r'_{i21}.A_4-r'_{i21}.Y'_0-r'_{i31}.Z'_0)}{Z(r'_{i13}.A_1+r'_{i23}.A_3+r'_{i33})-i(r'_{i13}.\Delta X'+r'_{i23}.\Delta Y'+r'_{i33}.\Delta Z')+(r'_{i13}.A_2-r'_{i13}.X'_0+r'_{i23}.A_4-r'_{i23}.Y'_0-r'_{i33}.Z'_0)}$$

$$\frac{y'_i-y_0}{-c} = \frac{Z(r'_{i12}.A_1+r'_{i22}.A_3+r'_{i32})-i(r'_{i12}.\Delta X'+r'_{i22}.\Delta Y'+r'_{i32}.\Delta Z')+(r'_{i12}.A_2-r'_{i12}.X'_0+r'_{i22}.A_4-r'_{i22}.Y'_0-r'_{i32}.Z'_0)}{Z(r'_{i13}.A_1+r'_{i23}.A_3+r'_{i33})-i(r'_{i13}.\Delta X'+r'_{i23}.\Delta Y'+r'_{i33}.\Delta Z')+(r'_{i13}.A_2-r'_{i13}.X'_0+r'_{i23}.A_4-r'_{i23}.Y'_0-r'_{i33}.Z'_0)} \tag{3.9}$$

Where:

$$R'_{i(\omega'_i,\varphi'_i,\kappa'_i)} = \begin{bmatrix} r'_{i11} & r'_{i12} & r'_{i13} \\ r'_{i21} & r'_{i22} & r'_{i23} \\ r'_{i31} & r'_{i32} & r'_{i33} \end{bmatrix}$$

Let us introduce the constants B_1 to B_9 as follows:

$$
\begin{aligned}
B_1 &= r'_{i11}.A_1 + r'_{i21}.A_3 + r'_{i31} \\
B_2 &= r'_{i11}.\Delta X' + r'_{i21}.\Delta Y' + r'_{i31}.\Delta Z' \\
B_3 &= r'_{i11}.A_2 - r'_{i11}.X'_0 + r'_{i21}.A_4 - r'_{i21}.Y'_0 - r'_{i31}.Z'_0 \\
B_4 &= r'_{i12}.A_1 + r'_{i22}.A_3 + r'_{i32} \\
B_5 &= r'_{i12}.\Delta X' + r'_{i22}.\Delta Y' + r'_{i32}.\Delta Z' \\
B_6 &= r'_{i12}.A_2 - r'_{i12}.X'_0 + r'_{i22}.A_4 - r'_{i22}.Y'_0 - r'_{i32}.Z'_0 \\
B_7 &= r'_{i13}.A_1 + r'_{i23}.A_3 + r'_{i33} \\
B_8 &= r'_{i13}.\Delta X' + r'_{i23}.\Delta Y' + r'_{i33}.\Delta Z' \\
B_9 &= r'_{i13}.A_2 - r'_{i13}.X'_0 + r'_{i23}.A_4 - r'_{i23}.Y'_0 - r'_{i33}.Z'_0
\end{aligned}
\tag{3.10}
$$

Then, Equations 3.9 are rewritten as:

$$\frac{x' - x_0}{-c} = \frac{Z.B_1 - i.B_2 + B_3}{Z.B_7 - i.B_8 + B_9} \tag{3.11}$$

$$\frac{y'_i - y_0}{-c} = \frac{Z.B_4 - i.B_5 + B_6}{Z.B_7 - i.B_8 + B_9} \tag{3.12}$$

Equation 3.11 can be reduced as follows:

$$Z\left[(x' - x_0)B_7 + c.B_1\right] = i\left[(x' - x_0)B_8 + c.B_2\right] + \left[-(x' - x_0)B_9 - c.B_3\right]$$

$$Z = \left[\frac{(x' - x_0)B_8 + c.B_2}{(x' - x_0)B_7 + c.B_1}\right] i + \left[\frac{-(x' - x_0)B_9 - c.B_3}{(x' - x_0)B_7 + c.B_1}\right] \tag{3.13}$$

Terms D_1 and D_2 can be introduced as follows:

$$
\begin{aligned}
D_1 &= \frac{(x' - x_0)B_8 + c.B_2}{(x' - x_0)B_7 + c.B_1} \\
D_2 &= \frac{-(x' - x_0)B_9 - c.B_3}{(x' - x_0)B_7 + c.B_1}
\end{aligned}
\tag{3.14}
$$

Thus, Equation 3.13 is rewritten as:

$$Z = D_1.i + D_2 \tag{3.15}$$

Substituting *Z* from Equation 3.15 into Equation 3.12 results in:

$$\frac{y'_i - y_0}{-c} = \frac{(D_1.i + D_2).B_4 - i.B_5 + B_6}{(D_1.i + D_2).B_7 - i.B_8 + B_9}$$

or,

$$\frac{y'_i - y_0}{-c} = \frac{i.(D_1.B_4 - B_5) + (B_6 + D_2.B_4)}{i.(D_1.B_7 - B_8) + (B_9 + D_2.B_7)}$$

Expanding:

$$\begin{aligned} c.i.(D_1.B_4 - B_5) + c.(B_6 + D_2.B_4) = & -y'_i\,(B_9 + D_2.B_7) + i.y_0(D_1.B_7 - B_8) \\ & + y_0(B_9 + D_2.B_7) - y'_i.i.(D_1.B_7 - B_8) \end{aligned}$$

$$\begin{aligned} y'_i\,[(B_9 + D_2.B_7)] + y'_i.i.[(D_1.B_7 - B_8)] = & \; i.[y_0(D_1.B_7 - B_8) - c(D_1.B_4 - B_5)] \\ & + [y_0(B_9 + D_2.B_7) - c.(B_6 + D_2.B_4)] \end{aligned} \tag{3.16}$$

Let us introduce the terms E_1 to E_4 as follows:

$$\begin{aligned} E_1 &= B_9 + D_2.B_7 \\ E_2 &= D_1.B_7 - B_8 \\ E_3 &= y_0(D_1.B_7 - B_8) - c(D_1.B_4 - B_5) \\ E_4 &= y_0(B_9 + D_2.B_7) - c.(B_6 + D_2.B_4) \end{aligned} \tag{3.17}$$

Use the above terms to rewrite Equation 3.16 as:

$$y'_i.E_1 + y'_i.i.E_2 = i.E_3 + E_4 \tag{3.18}$$

Recall that *i* and y'_i are the scene coordinates in the right scene (see Figure 2.10). Equation 3.18, therefore, represents the locus of potential conjugate points in the right scene; i.e., the equation of the epipolar line in the right scene. It is important to note that y'_i is unknown at image or scan line number *i*. The epipolar curve is a straight line if E_2=0 (if y'_i is a linear function of *i*). Therefore, the term E_2 must be analyzed as follows:

$$\begin{aligned}
E_2 &= D_1.B_7 - B_8 \\
&= \frac{(x'-x_0)B_8 + c.B_2}{(x'-x_0)B_7 + c.B_1}.B_7 - B_8 \\
&= \frac{(x'-x_0)B_8B_7 + c.B_2B_7 - (x'-x_0)B_7B_8 - c.B_1B_8}{(x'-x_0)B_7 + c.B_1} \\
&= \frac{c.B_2B_7 - c.B_1B_8}{(x'-x_0)B_7 + c.B_1} \\
&= \frac{B_2B_7 - B_1B_8}{\frac{(x'-x_0)}{c}B_7 + B_1} \\
&= \frac{(r'_{i11}.\Delta X' + r'_{i21}.\Delta Y' + r'_{i31}.\Delta Z')(r'_{i13}.A_1 + r'_{i23}.A_3 + r'_{i33}) - (r'_{i13}.\Delta X' + r'_{i23}.\Delta Y' + r'_{i33}.\Delta Z')(r'_{i11}.A_1 + r'_{i21}.A_3 + r'_{i31})}{\frac{(x'-x_0)}{c}B_7 + B_1}
\end{aligned}$$

$$\begin{aligned}
E_2\left[\frac{(x'-x_0)}{c}B_7 + B_1\right] &= (r'_{i11}.\Delta X' + r'_{i21}.\Delta Y' + r'_{i31}.\Delta Z')(r'_{i13}.A_1 + r'_{i23}.A_3 + r'_{i33}) \\
&\quad - (r'_{i13}.\Delta X' + r'_{i23}.\Delta Y' + r'_{i33}.\Delta Z')(r'_{i11}.A_1 + r'_{i21}.A_3 + r'_{i31}) \\
&= \Delta X'\,A_1(r'_{i11}\,r'_{i13} - r'_{i11}\,r'_{i13}) + \Delta X'\,A_3(r'_{i11}\,r'_{i23} - r'_{i21}\,r'_{i13}) + \Delta X'(r'_{i11}\,r'_{i33} - r'_{i31}\,r'_{i13}) \\
&\quad + \Delta Y'\,A_1(r'_{i21}\,r'_{i13} - r'_{i11}\,r'_{i23}) + \Delta Y'\,A_3(r'_{i21}\,r'_{i23} - r'_{i21}\,r'_{i23}) + \Delta Y'(r'_{i21}\,r'_{i33} - r'_{i31}\,r'_{i23}) \\
&\quad + \Delta Z'\,A_1(r'_{i31}\,r'_{i13} - r'_{i11}\,r'_{i33}) + \Delta Z'\,A_3(r'_{i31}\,r'_{i23} - r'_{i21}\,r'_{i33}) + \Delta Z'(r'_{i31}\,r'_{i33} - r'_{i31}\,r'_{i33})
\end{aligned}$$

Using the cosine and sine functions of r'_{ij}, the following reductions can be made:

$$\begin{aligned}
r'_{i11}\,r'_{i23} - r'_{i13}\,r'_{i21} &= -\sin\omega'\cos^2\varphi'\cos\kappa' - \cos\omega'\sin\varphi'\sin\kappa' - \sin\omega'\sin^2\varphi'\cos\kappa' \\
&= -\sin\omega'\cos\kappa' - \cos\omega'\sin\varphi'\sin\kappa' \\
&= -r'_{i32}
\end{aligned}$$

$$\begin{aligned}
r'_{i11}\,r'_{i33} - r'_{i13}\,r'_{i31} &= \cos\omega'\cos^2\varphi'\cos\kappa' - \sin\omega'\sin\varphi'\sin\kappa' + \cos\omega'\sin^2\varphi'\cos\kappa' \\
&= \cos\omega'\cos\kappa' - \sin\omega'\sin\varphi'\sin\kappa' \\
&= r'_{i22}
\end{aligned}$$

$$\begin{aligned}
r'_{i21}\,r'_{i13} - r'_{i11}\,r'_{i23} &= \cos\omega'\sin\varphi'\sin\kappa' + \sin\omega'\sin^2\varphi'\cos\kappa' + \sin\omega'\cos^2\varphi'\cos\kappa' \\
&= \sin\omega'\cos\kappa' + \cos\omega'\sin\varphi'\sin\kappa' \\
&= r'_{i32}
\end{aligned}$$

$$\begin{aligned}
r'_{i21}\,r'_{i33} - r'_{i31}\,r'_{i23} &= \cos^2\omega'\cos\varphi'\sin\kappa' + \sin\omega'\cos\omega'\sin\varphi'\cos\varphi'\cos\kappa' + \sin^2\omega'\cos\varphi'\sin\kappa' \\
&\quad - \sin\omega'\cos\omega'\sin\varphi'\cos\varphi'\cos\kappa' \\
&= \cos\varphi'\sin\kappa' \\
&= -r'_{i12}
\end{aligned}$$

$$\begin{aligned} r'_{i31}\,r'_{i13} - r'_{i11}\,r'_{i33} &= \sin\omega'\sin\varphi'\sin\kappa' - \cos\omega'\sin^2\varphi'\cos\kappa' - \cos\omega'\cos^2\varphi'\cos\kappa' \\ &= \sin\omega'\sin\varphi'\sin\kappa' - \cos\omega'\cos\kappa' \\ &= -r'_{i22} \end{aligned}$$

$$\begin{aligned} r'_{i31}\,r'_{i23} - r'_{i21}\,r'_{i33} &= -\sin^2\omega'\cos\varphi'\sin\kappa' + \sin\omega'\cos\omega'\sin\varphi'\cos\varphi'\cos\kappa' - \cos^2\omega'\cos\varphi'\sin\kappa' \\ &\quad - \sin\omega'\cos\omega'\sin\varphi'\cos\varphi'\cos\kappa' \\ &= -\cos\varphi'\sin\kappa' \\ &= r'_{i12} \end{aligned}$$

Therefore, E_2 can be redefined as follows:

$$\begin{aligned} E_2\left[\frac{(x'-x_0)}{c}B_7 + B_1\right] &= \Delta X' A_3(-r'_{i32}) + \Delta X'(r'_{i22}) + \Delta Y' A_1(r'_{i32}) + \Delta Y'(-r'_{i12}) + \Delta Z' A_1(-r'_{i22}) + \Delta Z' A_3(r'_{i12}) \\ &= -\left[r'_{i12}(\Delta Y' - \Delta Z' A_3) - r'_{i22}(\Delta X' - \Delta Z' A_1) + r'_{i32}(\Delta X' A_3 - \Delta Y' A_1)\right] \\ &= -\begin{vmatrix} r'_{i12} & r'_{i22} & r'_{i32} \\ \Delta X' & \Delta Y' & \Delta Z' \\ A_1 & A_3 & 1 \end{vmatrix} \end{aligned} \tag{3.19}$$

Introduce F as follows:

$$F = \frac{(x'-x_0)}{c}B_7 + B_1 \tag{3.20}$$

Equation 3.19 can be rewritten as:

$$E_2\ F = -\begin{vmatrix} r'_{i12} & r'_{i22} & r'_{i32} \\ \Delta X' & \Delta Y' & \Delta Z' \\ A_1 & A_3 & 1 \end{vmatrix} \tag{3.21}$$

Setting E_2 to 0, the condition for having the epipolar curve as a straight line can be expressed as:

$$\begin{vmatrix} r'_{i12} & r'_{i22} & r'_{i32} \\ \Delta X' & \Delta Y' & \Delta Z' \\ A_1 & A_3 & 1 \end{vmatrix} = 0 \tag{3.22}$$

Substituting for A_1 and A_3, the above condition can be rewritten as:

$$\begin{vmatrix} r'_{i12} & r'_{i22} & r'_{i32} \\ \Delta X' & \Delta Y' & \Delta Z' \\ \dfrac{r_{j11}(x-x_0)+r_{j12}(y_j-y_0)+r_{j13}(-c)}{r_{j31}(x-x_0)+r_{j32}(y_j-y_0)+r_{j33}(-c)} & \dfrac{r_{j21}(x-x_0)+r_{j22}(y_j-y_0)+r_{j23}(-c)}{r_{j31}(x-x_0)+r_{j32}(y_j-y_0)+r_{j33}(-c)} & 1 \end{vmatrix} = 0$$

$$\begin{vmatrix} r'_{i12} & r'_{i22} & r'_{i32} \\ \Delta X' & \Delta Y' & \Delta Z' \\ r_{j11}(x-x_0)+r_{j12}(y_j-y_0)+r_{j13}(-c) & r_{j21}(x-x_0)+r_{j22}(y_j-y_0)+r_{j23}(-c) & r_{j31}(x-x_0)+r_{j32}(y_j-y_0)+r_{j33}(-c) \end{vmatrix} = 0$$

$$\begin{vmatrix} r'_{i12} & r'_{i22} & r'_{i32} \\ \Delta X' & \Delta Y' & \Delta Z' \\ X-X_{0j} & Y-Y_{0j} & Z-Z_{0j} \end{vmatrix} = 0$$

This condition can be rewritten as the triple product of three vectors, $\boldsymbol{v_1}$, $\boldsymbol{v_2}$ and $\boldsymbol{v_3}$, as:

$$(\boldsymbol{v_1} \otimes \boldsymbol{v_2}) \circ \boldsymbol{v_3} = 0 \tag{3.23}$$

where:

$$\boldsymbol{v_1} = \begin{bmatrix} r'_{i12} \\ r'_{i22} \\ r'_{i32} \end{bmatrix},$$

$$\boldsymbol{v_2} = \begin{bmatrix} \Delta X' \\ \Delta Y' \\ \Delta Z' \end{bmatrix}, \text{ and}$$

$$\boldsymbol{v_3} = \begin{bmatrix} X-X_{0j} \\ Y-Y_{0j} \\ Z-Z_{0j} \end{bmatrix}$$

Equation 3.23 indicates that these three vectors, shown in Figure 3.1, must be coplanar in order to have the epipolar curve as a straight line.

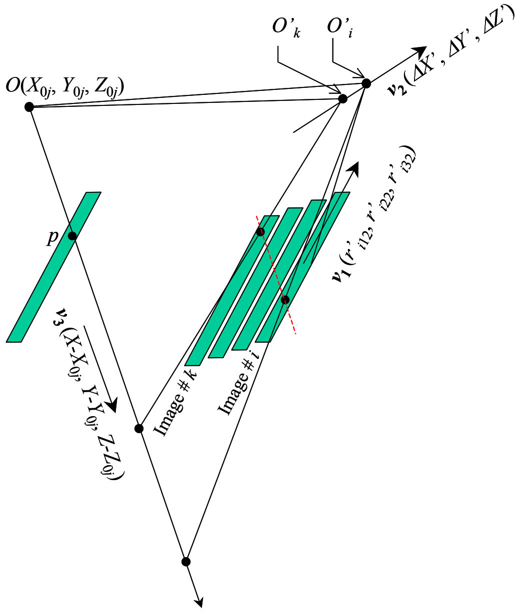

Figure 3.1: Vectors $\boldsymbol{v}_1$, $\boldsymbol{v}_2$, and $\boldsymbol{v}_3$ in Equation 3.23

In reality, it is hardly ever possible to find the above condition valid and absolutely equal to zero. For the case of a general epipolar curve, in order to quantify the straightness of the epipolar curve, the value of E_2 must be compared to the value of E_1. The smaller the ratio of (E_2 / E_1), the epipolar curve will approach straightness.

E_1 can be analyzed as follows:

$$
\begin{aligned}
E_1 &= D_2.B_7 + B_9 \\
&= \frac{-(x'-x_0)B_9 - c.B_3}{(x'-x_0)B_7 + c.B_1}.B_7 + B_9 \\
&= \frac{-(x'-x_0)B_9B_7 - c.B_3B_7 + (x'-x_0)B_7B_9 + c.B_1B_9}{(x'-x_0)B_7 + c.B_1} \\
&= \frac{c.B_1B_9 - c.B_3B_7}{(x'-x_0)B_7 + c.B_1} \\
&= \frac{B_1B_9 - B_3B_7}{\frac{(x'-x_0)}{c}B_7 + B_1} \\
&= \left[\left(r'_{i13}.A_2 - r'_{i13}.X'_0 + r'_{i23}.A_4 - r'_{i23}.Y'_0 - r'_{i33}.Z'_0\right)\left(r'_{i11}.A_1 + r'_{i21}.A_3 + r'_{i31}\right)\right. \\
&\quad \left. -\left(r'_{i11}.A_2 - r'_{i11}.X'_0 + r'_{i21}.A_4 - r'_{i21}.Y'_0 - r'_{i31}.Z'_0\right)\left(r'_{i13}.A_1 + r'_{i23}.A_3 + r'_{i33}\right)\right] / \left[\frac{(x'-x_0)}{c}B_7 + B_1\right]
\end{aligned}
$$

$$
\begin{aligned}
E_1\left[\frac{(x'-x_0)}{c}B_7+B_1\right] &= \left(r'_{i13}.A_2-r'_{i13}.X'_0+r'_{i23}.A_4-r'_{i23}.Y'_0-r'_{i33}.Z'_0\right)\left(r'_{i11}.A_1+r'_{i21}.A_3+r'_{i31}\right)\\
&\quad-\left(r'_{i11}.A_2-r'_{i11}.X'_0+r'_{i21}.A_4-r'_{i21}.Y'_0-r'_{i31}.Z'_0\right)\left(r'_{i13}.A_1+r'_{i23}.A_3+r'_{i33}\right)\\
&= X'_0\ A_1\left(r'_{i11}\ r'_{i13}-r'_{i11}\ r'_{i13}\right)+X'_0\ A_3\left(r'_{i11}\ r'_{i23}-r'_{i21}\ r'_{i13}\right)+X'_0\left(r'_{i11}\ r'_{i33}-r'_{i31}\ r'_{i13}\right)\\
&\quad+Y'_0\ A_1\left(r'_{i21}\ r'_{i13}-r'_{i11}\ r'_{i23}\right)+Y'_0\ A_3\left(r'_{i21}\ r'_{i23}-r'_{i21}\ r'_{i23}\right)+Y'_0\left(r'_{i21}\ r'_{i33}-r'_{i31}\ r'_{i23}\right)\\
&\quad+Z'_0\ A_1\left(r'_{i31}\ r'_{i13}-r'_{i11}\ r'_{i33}\right)+Z'_0\ A_3\left(r'_{i31}\ r'_{i23}-r'_{i21}\ r'_{i33}\right)+Z'_0\left(r'_{i31}\ r'_{i33}-r'_{i31}\ r'_{i33}\right)\\
&\quad+A_1A_2\left(r'_{i11}\ r'_{i13}-r'_{i11}\ r'_{i13}\right)+A_1A_4\left(r'_{i11}\ r'_{i23}-r'_{i21}\ r'_{i13}\right)+A_2A_3\left(r'_{i21}\ r'_{i13}-r'_{i11}\ r'_{i23}\right)\\
&\quad+A_3A_4\left(r'_{i21}\ r'_{i23}-r'_{i21}\ r'_{i23}\right)+A_2\left(r'_{i31}\ r'_{i13}-r'_{i11}\ r'_{i33}\right)+A_4\left(r'_{i31}\ r'_{i23}-r'_{i21}\ r'_{i33}\right)\\
&= X'_0\ A_3\left(-r'_{i32}\right)+X'_0\left(r'_{i22}\right)+Y'_0\ A_1\left(r'_{i32}\right)+Y'_0\left(-r'_{i12}\right)+Z'_0\ A_1\left(-r'_{i22}\right)+Z'_0\ A_3\left(r'_{i12}\right)\\
&\quad+A_1A_4\left(-r'_{i32}\right)+A_2A_3\left(r'_{i32}\right)+A_2\left(-r'_{i22}\right)+A_4\left(r'_{i12}\right)\\
&= r'_{i12}\left(-Y'_0+A_3Z'_0+A_4\right)+r'_{i22}\left(X'_0-A_1Z'_0-A_2\right)+r'_{i32}\left(-A_3X'_0+A_1Y'_0-A_1A_4+A_2A_3\right)\\
&= r'_{i12}\left(-Y'_0+A_3Z'_0+Y_{0j}-A_3Z_{0j}\right)+r'_{i22}\left(X'_0-A_1Z'_0+A_1Z_{0j}-X_{0j}\right)\\
&\quad+r'_{i32}\left(-A_3X'_0+A_1Y'_0-A_1Y_{0j}+A_1A_3Z_{0j}+A_3X_{0j}-A_1A_3Z_{0j}\right)\\
&= -\Big[r'_{i12}\left(Y'_0-Y_{0j}-A_3\left(Z'_0-Z_{0j}\right)\right)-r'_{i22}\left(X'_0-X_{0j}-A_1\left(Z'_0-Z_{0j}\right)\right)\\
&\quad+r'_{i32}\left(A_3\left(X'_0-X_{0j}\right)-A_1\left(Y'_0-Y_{0j}\right)\right)\Big]\\
&= -\begin{vmatrix} r'_{i12} & r'_{i22} & r'_{i32}\\ X'_0-X_{0j} & Y'_0-Y_{0j} & Z'_0-Z_{0j}\\ A_1 & A_3 & 1\end{vmatrix}
\end{aligned}
\tag{3.24}
$$

Substituting for *F* from Equation 3.20 into Equation 3.24, we obtain:

$$
E_1\ F = -\begin{vmatrix} r'_{i12} & r'_{i22} & r'_{i32}\\ X'_0-X_{0j} & Y'_0-Y_{0j} & Z'_0-Z_{0j}\\ A_1 & A_3 & 1\end{vmatrix}
\tag{3.25}
$$

The ratio (E_2 / E_1) can be computed as follows:

$$\frac{E_2}{E_1}=\frac{\begin{vmatrix} r'_{i12} & r'_{22} & r'_{i32} \\ \Delta X' & \Delta Y' & \Delta Z' \\ A_1 & A_3 & 1 \end{vmatrix}}{\begin{vmatrix} r'_{i12} & r'_{i22} & r'_{i32} \\ X'_0-X_{0j} & Y'_0-Y_{0j} & Z'_0-Z_{0j} \\ A_1 & A_3 & 1 \end{vmatrix}} =\frac{\begin{vmatrix} r'_{i12} & r'_{i22} & r'_{i32} \\ \Delta X' & \Delta Y' & \Delta Z' \\ X-X_{0j} & Y-Y_{0j} & Z-Z_{0j} \end{vmatrix}}{\begin{vmatrix} r'_{i12} & r'_{i22} & r'_{i32} \\ X'_0-X_{0j} & Y'_0-Y_{0j} & Z'_0-Z_{0j} \\ X-X_{0j} & Y-Y_{0j} & Z-Z_{0j} \end{vmatrix}} \tag{3.26}$$

In the above derivation, it was assumed that F (in Equations 3.20, 3.21 and 3.25) does not equal zero. In the case where this term equals zero, Equation 3.18 reduces to (i=constant), which means that epipolar lines are straight lines and they coincide with the scene scan lines (rows). This is a special case of SPOT where the vectors $\boldsymbol{v}_1$ and $\boldsymbol{v}_3$ and $\boldsymbol{B}$ are coplanar, as shown in Figure 3.2. In practice, it is rare to find this condition to be valid due to the differences in the scanner locations and rotation angles.

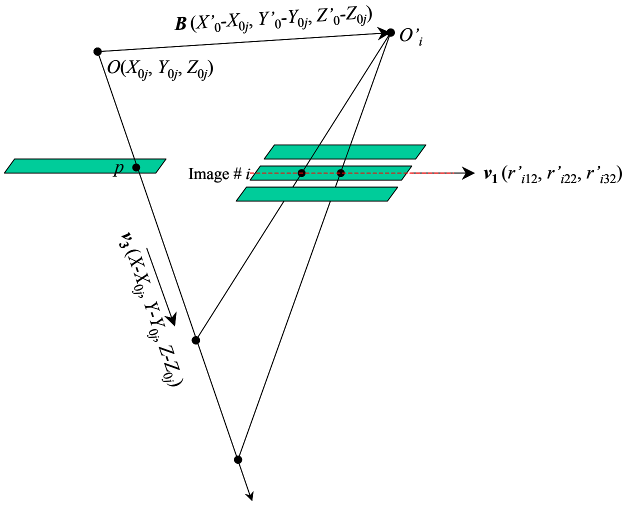

Figure 3.2: Epipolar lines corresponding to the scene rows

In summary, in order to analyze the shape of epipolar lines, the following procedure can be used:

- If F=0 (Equation 3.20), the epipolar lines are straight lines and they will coincide with the scene rows (i=constant), as shown in Figure 3.2.
- If $F \neq 0$, the epipolar lines are not straight lines. In this case, the ratio E_2/E_1, as in Equation 3.23, quantifies the straightness of the epipolar curve.

Recall that epipolar lines in frame images are straight lines in both the raw and normalized images, as discussed in Chapter 2. Therefore, no distortions are introduced in such a process. On the other hand, in linear array scenes, epipolar lines may not be straight, but it is desirable for them to be straight lines in the normalized scenes. Therefore, the evaluation of their non-straightness in the raw scenes will give us an indication of the magnitude of the errors introduced in the normalized scenes.

3.3 EXPERIMENTS

In this section, the straightness of the epipolar lines will be examined. In order to study the epipolar geometry, two scenes are needed. To this end, nine experiments have been performed. Experiments 3.1, 3.2 and 3.3 were simulated to obtain stereo coverage by changing x_i values similar to what was discussed in Section 2.3.1.4 for three-line camera, and from different altitudes. On the other hand, Experiments 3.4, 3.5 and 3.6 were simulated to obtain stereo coverage by changing the pitch angles along track similar to that of IKONOS, and from different altitudes. Finally, Experiments 3.7, 3.8 and 3.9 were simulated to obtain stereo coverage by changing roll angles across-track similar to that of SPOT and again from different altitudes. Table 3.1 summarizes the experiments according to stereo coverage method and altitude. In these experiments, as the scanner's altitude increases, the AFOV was reduced to maintain similar ground coverage.

Table 3.1: Summary of Experiments 3.1 to 3.9

		Altitude		
		1000 m	680 km	822 km
Stereo coverage method	Three-line scanner	Experiment 3.1	Experiment 3.2	Experiment 3.3
	Changing pitch angle	Experiment 3.4	Experiment 3.5	Experiment 3.6
	Changing roll angle	Experiment 3.7	Experiment 3.8	Experiment 3.9

Figure 3.3 shows the footprint of the scenes for the different experiments. The footprints have been identified by projecting the scan lines using their positions and orientations onto a zero-elevation surface plane. It must be noted that the elevation is not required in order to determine the epipolar geometry. However, it has been used here so as to visualize the approximate ground coverage of the scenes at a certain elevation. Five points have been selected in the left scene in each of these experiments, as shown in Figure 3.4. The projection of these points on the zero elevation surface plane is also shown in Figure 3.3. Again, the true elevation values of these points (labeled from 1 to 5) are not required for determining their corresponding epipolar lines. Figure 3.5 shows the corresponding epipolar lines of these points. The epipolar lines were drawn within the extent of the right scenes. Dotted straight lines were added between the beginning and ending points to depict visually the straightness of these epipolar lines. It has been found that neither F (Equation 3.20) nor E_2 (Equation 3.21) equals zero. Therefore, for the general case of a linear array scanner (even with the constant-velocity-constant-attitude trajectory model), the epipolar lines are not straight. In order to quantify the straightness of epipolar lines, Table 3.2 lists the values of E_2/E_1 for the experiments.

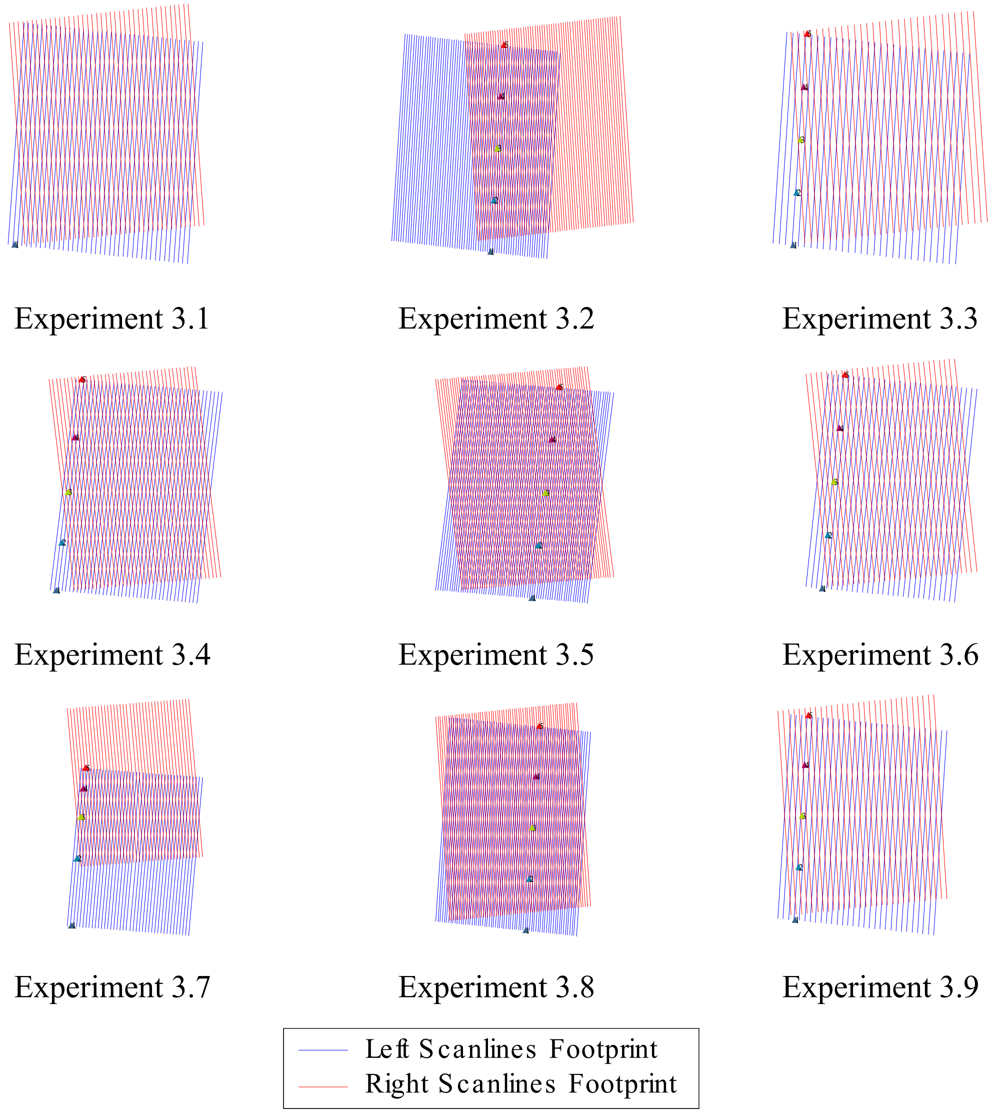

Experiment 3.1 Experiment 3.2 Experiment 3.3

Experiment 3.4 Experiment 3.5 Experiment 3.6

Experiment 3.7 Experiment 3.8 Experiment 3.9

Figure 3.3: Scene footprints for Experiments 3.1 to 3.9 projected to a zero-elevation plane. (Note: Points whose epipolar lines are analyzed are projected onto the same plane.)

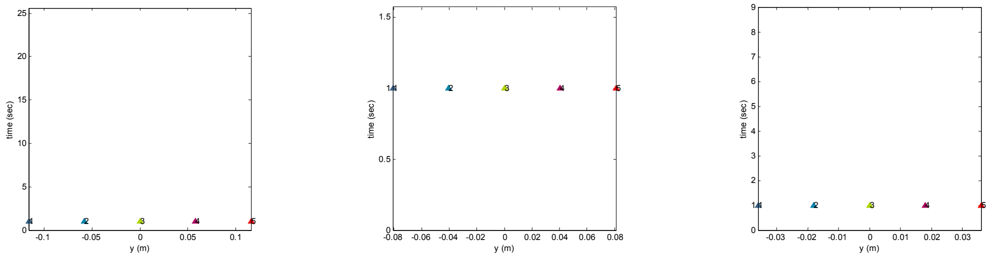

Experiment 3.1 Experiment 3.2 Experiment 3.3

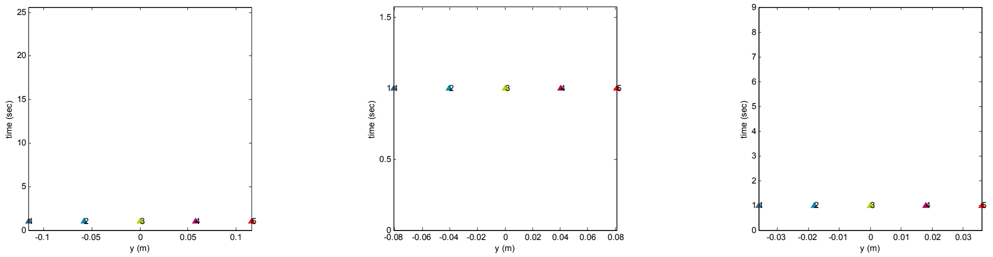

Experiment 3.4 Experiment 3.5 Experiment 3.6

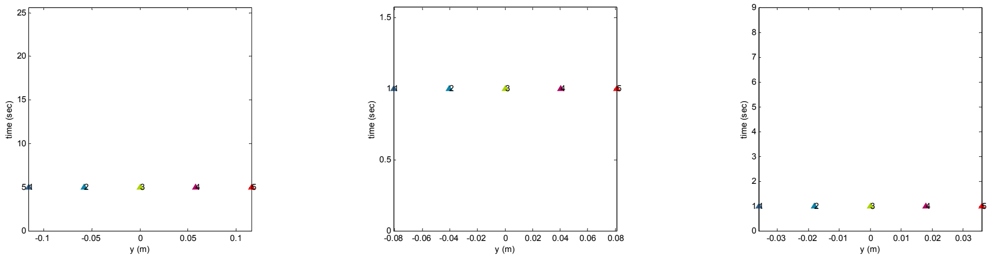

Experiment 3.7 Experiment 3.8 Experiment 3.9

Figure 3.4: Left scenes of Experiments 3.1 to 3.9 including the points whose epipolar lines are analyzed

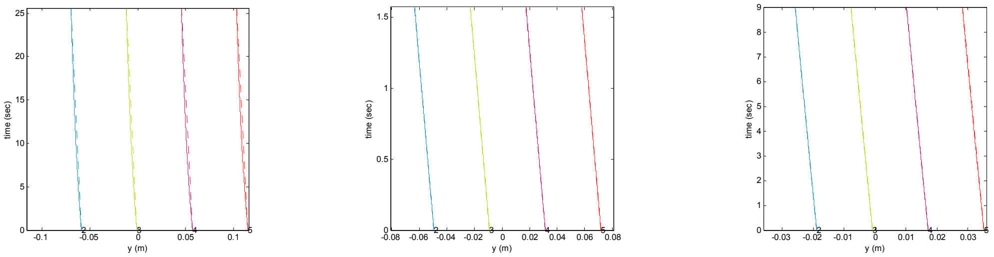

Experiment 3.1 Experiment 3.2 Experiment 3.3

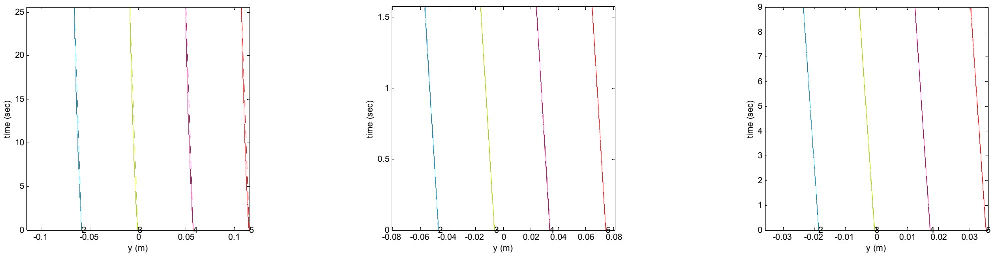

Experiment 3.4 Experiment 3.5 Experiment 3.6

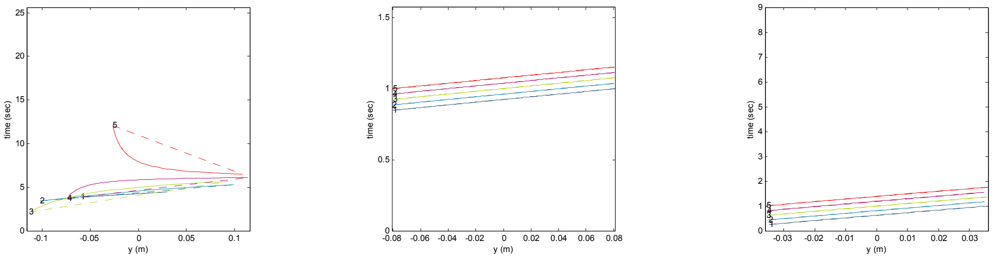

Experiment 3.7 Experiment 3.8 Experiment 3.9

Figure 3.5: Right scenes of Experiments 3.1 to 3.9 including the epipolar lines for the selected points

Table 3.2: Values of E_2/E_1 for various points in Experiments 3.1 to 3.9

Point number	Experiment								
	3.1	3.2	3.3	3.4	3.5	3.6	3.7	3.8	3.9
1	0.031	0.0052	0.0043	0.03084	0.00515	0.00426	-0.012	-0.076	-0.062
2	0.031	0.0052	0.0043	0.03083	0.00515	0.00426	-0.114	-0.077	-0.063
3	0.031	0.0052	0.0043	0.03082	0.00515	0.00426	-0.144	-0.077	-0.065
4	0.031	0.0052	0.0043	0.03081	0.00515	0.00426	-0.158	-0.077	-0.066
5	0.031	0.0052	0.0043	0.03080	0.00515	0.00426	-0.167	-0.078	-0.067
Mean ±Std	**0.031** **±0.000**	**0.0052** **±0.0000**	**0.0043** **±0.0000**	**0.03082** **±0.00002**	**0.00515** **±0.00000**	**0.00426** **±0.0000**	**-0.119** **±0.0632**	**-0.077** **±0.0006**	**-0.065** **±0.002**

Examining the standard deviation of E_2/E_1 of the selected points in each experiment, as listed in Table 3.2, it is noticeable that E_2/E_1 values do not change from point to point in the scene in Experiments 3.1 to 3.6. This means that these epipolar lines, even if they are not straight lines, are changing in a similar fashion. On the other hand, the standard deviations of E_2/E_1 values in Experiments 3.7 to 3.9 are relatively large, which consequently produces a high variation in the shapes of the epipolar lines. This is confirmed by an extreme example, Experiment 3.7, as shown in Figure 3.5. Therefore, it can be concluded that stereo coverage regimes similar to that of three-line camera or IKONOS are superior, in terms of shape variation of epipolar lines, to that of SPOT.

Examining the average values of E_2/E_1 as listed in Table 3.2, it is noticeable that E_2/E_1 decreases as the AFOV decreases, for the same stereo coverage type. Moreover, stereo coverage similar to IKONOS or three-line cameras gives smaller average values than that of SPOT at the same altitude. This can be confirmed by a comparison of the average values of Experiments 3.1, 3.4 and 3.7; those of Experiment 3.2, 3.5 and 3.8, and finally those of Experiments 3.3, 3.6 and 3.9.

It is important to note that the value of E_2/E_1 can give an indication of the general behavior of the epipolar line, but not necessarily within the extent of the scene.

3.4 SUMMARY

It has been concluded that, for the constant-velocity-constant-attitude EOP model, the epipolar line is found to be a non-straight line in general. In addition, a quantitative analysis of its non-straightness was introduced.

An analysis of alternative stereo-coverage possibilities revealed that along-track stereo observation using pitch angles along with the use of three-line scanners is superior to across-track stereo coverage using roll angles, as they introduce straighter epipolar lines. Moreover, as the flying height increases and the angular field of view decreases, epipolar lines become straighter. Such conclusions motivate us to investigate the epipolar resampling of space-borne scenes such as IKONOS.

However, as the rigorous model produces non-straight epipolar lines, an alternative model will be sought. Parallel projection was chosen as an alternative model; it is discussed in detail, including the rationale behind its selection, in Chapter 4.

CHAPTER 4: PARALLEL PROJECTION

4.1 INTRODUCTION

In Chapter 3, the geometry of epipolar lines in constant-velocity-constant-attitude linear array scanner scenes was studied. However, it is desirable to have scenes with straight epipolar lines, which is the condition for straightforward resampling of imagery according to epipolar geometry. Therefore, the amount of deviation from straightness associated with epipolar lines in raw scenes can be considered as an indication of the level of difficulty in transforming these scenes into normalized ones.

In this chapter, parallel projection, rather than the rigorous perspective model, is used to model, or to approximate, the relationship between corresponding scene and object space points. The chapter begins with the motivation and main reasons behind using the parallel projection. Following an explanation of its concept, the mathematical model of parallel projection is derived, and various cases of parallel projection are discussed and tested.

4.2 MOTIVATION

The parallel projection approximates the mathematical relation between the scene and object space coordinates using fewer parameters. This characteristic makes it appealing to many researchers and applications (Okamoto, 1992; and Okamoto et al., 1992; Okamoto et al., 1996; Ono et al., 1996; Okamoto and Fraser, 1998; Ono et al., 1999; Fraser, 2000; Hattori et al., 2000; Ono et al., 2000). A brief explanation of the reasons for choosing such a model are listed below:

- The very narrow AFOV of some sensors (such as IKONOS) can result in having almost parallel projection in the scanning direction. Figure 4.1 shows a schematic drawing to illustrate this concept. Figure 4.1a is the actual perspective geometry of a scan line, while Figure 4.1b shows a parallel projection of the same area. The two parts of the figure have been drawn separately to show the difference between the two types of projection. As the AFOV gets smaller, the difference between the recorded 1-D images in Figure 4.1a and b become insignificant except for scale.

- The constant attitude of the scanner during scene capture, as indicated by constant ω, φ, *and* κ angles in Equations 3.1, leads to parallel scan lines. Consequently, the resulting 1-D images and their ground strips will be parallel as shown in Figure 4.2a. This fact, together with the small AFOV, establishes the projection direction, as shown in Figure 4.2b.
- Building upon the above two reasons, a constant-velocity (straight-line constant-speed) trajectory makes the assumption of parallel projection more reasonable. Figure 4.3 shows a scene generated with a straight-line constant-speed trajectory of the scanner that has very small AFOV and constant attitude. It can be proven that parallel lines will be mapped as parallel lines. In addition, ratios between points *A*, *B* and, *C* will be preserved in the scene space if the scanner sweeps equal areas in equal time intervals; i.e., if the scanner moves with constant speed. On the other hand, Figure 4.4 shows a scanner that is not moving in a straight line. In this case, straight lines in the object space will not be mapped as straight lines in the scene space. This is one of the motivations for studying the epipolar geometry of the constant-velocity trajectory model in Chapter 3. It is important to mention that similar assumptions were made for deriving the SDLT model (Wang, 1999).

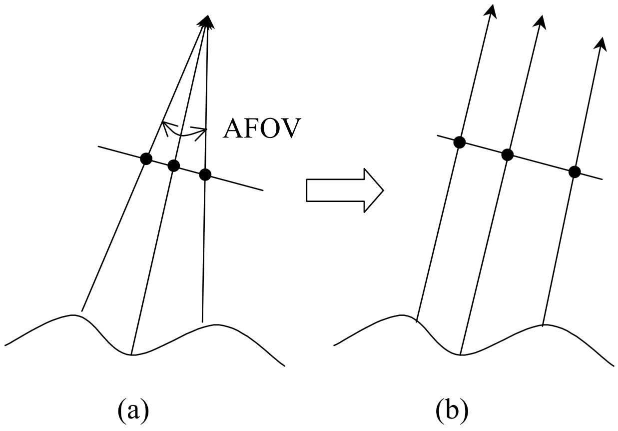

Figure 4.1: (a) Perspective projection and (b) parallel projection

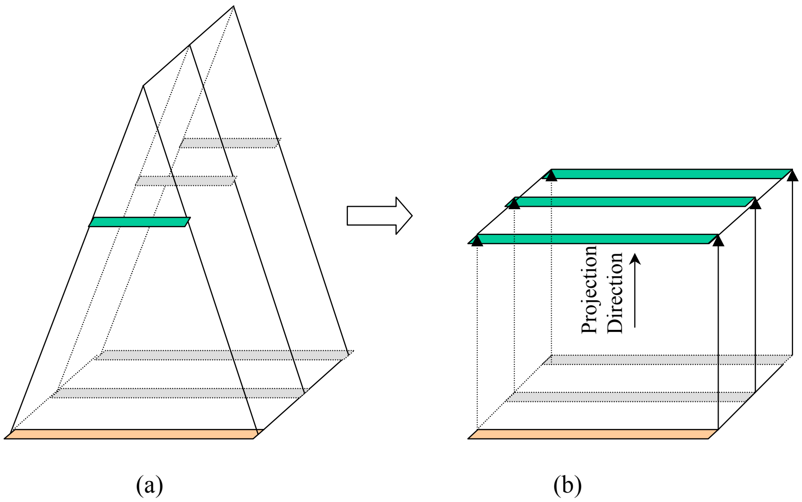

Figure 4.2: Parallel 1-D images and parallel ground strips (a), together with narrow AFOV, set up the direction of parallel projection (b)

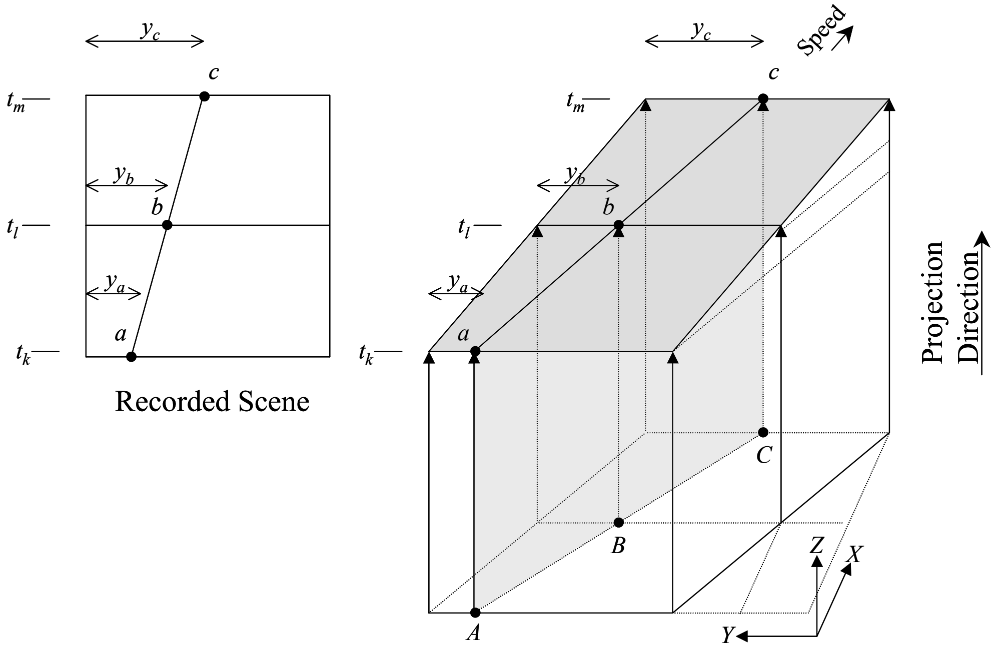

Figure 4.3: Straight line is projected as straight line, using a straight-line trajectory scanner

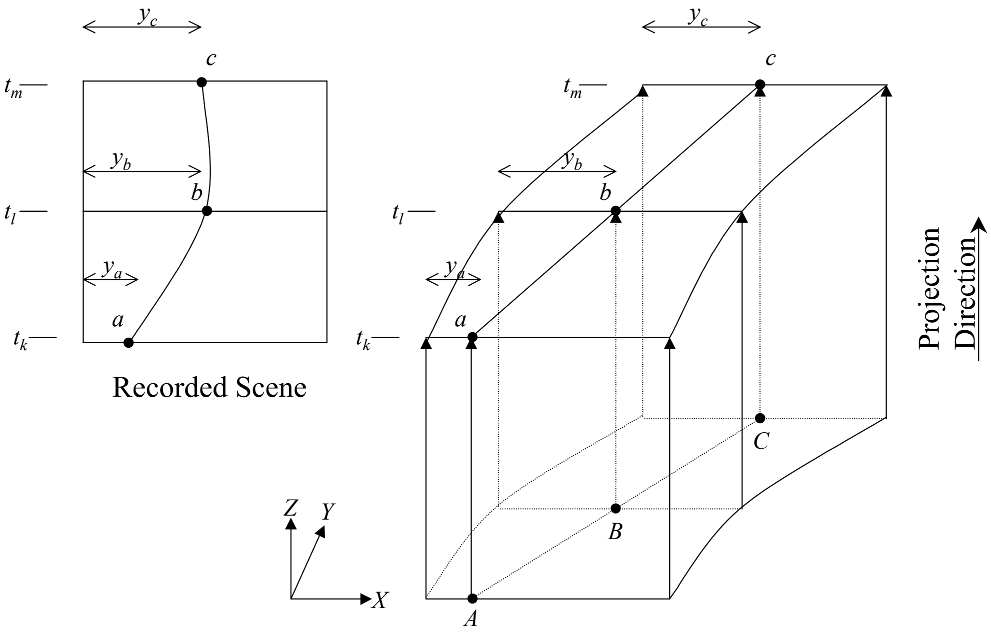

Figure 4.4: Straight line is projected as non-straight line in a non-straight line trajectory scanner

4.3 CONCEPT OF PARALLEL PROJECTION

Parallel projection can be defined using two surfaces. Points in one surface are projected onto the other with parallel projection rays, as shown in Figure 4.5. Therefore, three components are required: two surfaces and a unit direction in space. Examples of parallel projections are shown in Figure 4.6.

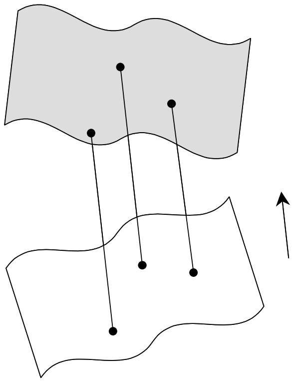

Figure 4.5: Concept of parallel projection between two surfaces

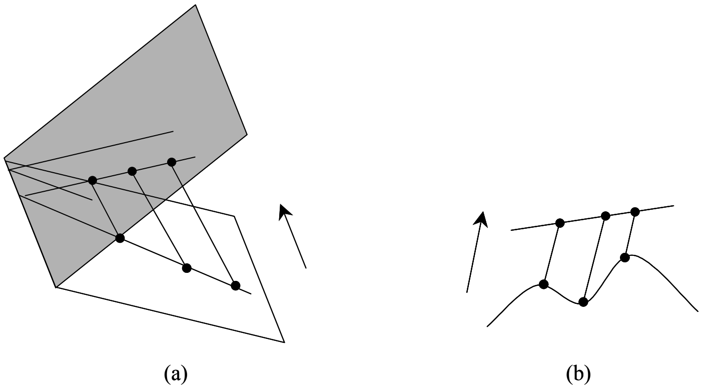
(a) (b)

Figure 4.6: Examples of parallel projection

Figure 4.6a shows parallel projection between two planar surfaces. In this case, the following observations can be made:

- Straight lines in one of the planes are projected as straight lines in the other plane;
- Parallel straight lines in one of the planes are projected as parallel straight lines in the other plane; and
- Distance ratios between points along a straight line in one of the planes are preserved between corresponding projected points in the other plane.

The above three conditions comprise the requirements for an Affine transformation; it can be concluded that parallel projection between planar surfaces is an Affine transformation. The mathematical derivation will be provided in Sections 4.4.3 and 4.5.2. On the other hand, not all Affine transformations are parallel projections. The reason is that, in parallel projection between planes, there is one line (the intersection of the two planes) along which the scale is unity while, in the general Affine transformation, this criterion is not necessarily maintained. Therefore, parallel projections are a subclass of the Affine transformation.

Figure 4.6b shows a profile of parallel projection between planar and non-planar surfaces. It can be easily seen that this projection is not an Affine transformation. One of the reasons is that distance ratios are not maintained between the original and projected surfaces.

The mathematical model of parallel projection between non-planar and planar surfaces - i.e., between the object space and scene space - will be derived in Section 4.4. In Section 4.5, parallel projection between non-planar and two planar surfaces (i.e., two scenes) will be analyzed.

4.4 PARALLEL PROJECTION BETWEEN NON-PLANAR AND PLANAR SURFACES

4.4.1 Mathematical Model

Considering Figure 4.7, O is the origin of the object coordinate system with axes X, Y, and Z. Point O can be selected to be the origin of the scene coordinate system whose axes are u, v and w. Let point P $(X, Y, Z)^T$ in the object space be mapped to $(u, v, 0)^T$ in the scene coordinate system. The unit projection vector with respect to the object coordinate system is $(L, M, N)^T$, where:

$$N = \sqrt{1 - L^2 - M^2} \tag{4.1}$$

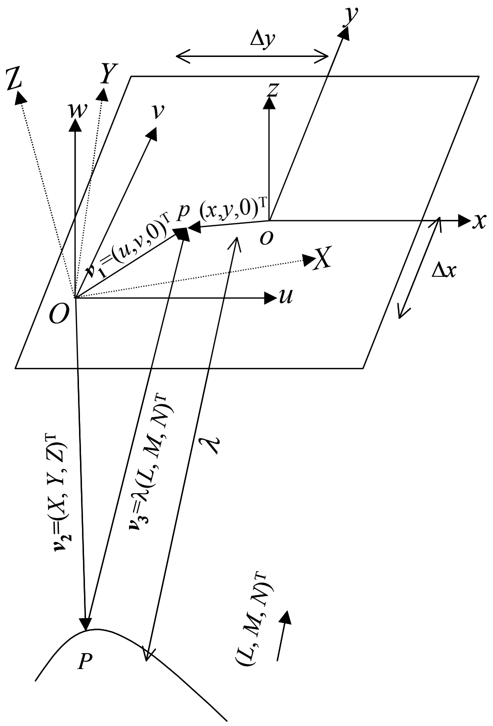

Figure 4.7: Mathematical model of parallel projection to a planar surface

Vectors $\boldsymbol{v}_1$, $\boldsymbol{v}_2$ and $\boldsymbol{v}_3$ can be introduced as follows:

$\boldsymbol{v}_1 = \begin{bmatrix} u \\ v \\ 0 \end{bmatrix}$ scene point coordinates with respect to the scene coordinate system;

$\boldsymbol{v}_2 = OP = \begin{bmatrix} X \\ Y \\ Z \end{bmatrix}$ corresponding object point coordinates with respect to the object coordinate system; and

$\boldsymbol{v}_3 = \lambda \begin{bmatrix} L \\ M \\ N \end{bmatrix}$ vector connecting scene and object points with respect to the object coordinate system.

where λ is the distance between the object point P and its scene point p. Its value changes from one point to another.

From Figure 4.7, the following vector summation equation can be written:

$$\boldsymbol{v}_1 = R^T \boldsymbol{v}_2 + R^T \boldsymbol{v}_3 \tag{4.2}$$

where R is the rotation matrix between the scene and object coordinate systems, based on the rotation angles ω, φ, and κ around X, Y, and Z axes, respectively. The vectors $\boldsymbol{v}_2$ and $\boldsymbol{v}_3$ are pre-multiplied with R^{T} so that they are referenced to the scene coordinate system. Substituting the components of the vectors $\boldsymbol{v}_1$, $\boldsymbol{v}_2$ and $\boldsymbol{v}_3$ in equation 4.2 results in:

$$\begin{bmatrix} u \\ v \\ 0 \end{bmatrix} = R^T \begin{bmatrix} X \\ Y \\ Z \end{bmatrix} + \lambda R^T \begin{bmatrix} L \\ M \\ N \end{bmatrix} \tag{4.3}$$

It is important to note that O was chosen to be the origin of the scene coordinate system as shown in Figure 4.7. Therefore, scene axes u, v and w can be shifted with the three shift values Δx, Δy and Δz, to obtain a parallel scene coordinate system whose axes are x, y, z, respectively. However, due to the nature of parallel projection, the same image is obtained if a different Δz value is chosen; i.e., if another parallel scene plane is chosen. Therefore, the three shift parameters are dependent, and consequently only two shift values Δx and Δy within the scene plane can be adopted, as seen in Figure 4.7.

A scale s can be applied to the recorded scene to ensure a smaller scene than the actual object space. Applying the scale value s and the two shift values Δx and Δy to the scene coordinates (u, v, 0) in Equations 4.3 results in:

$$\begin{bmatrix} x \\ y \\ 0 \end{bmatrix} = s\begin{bmatrix} u \\ v \\ 0 \end{bmatrix} + \begin{bmatrix} \Delta x \\ \Delta y \\ 0 \end{bmatrix}$$

$$= s\left(\lambda . R^T \begin{bmatrix} L \\ M \\ N \end{bmatrix} + R^T \begin{bmatrix} X \\ Y \\ Z \end{bmatrix} \right) + \begin{bmatrix} \Delta x \\ \Delta y \\ 0 \end{bmatrix}$$

Therefore, the mathematical model of the parallel projection between planar (the scene) and non-planar (the object space) surfaces is expressed as follows:

$$\begin{bmatrix} x \\ y \\ 0 \end{bmatrix} = s.\lambda . R^T \begin{bmatrix} L \\ M \\ N \end{bmatrix} + s.R^T \begin{bmatrix} X \\ Y \\ Z \end{bmatrix} + \begin{bmatrix} \Delta x \\ \Delta y \\ 0 \end{bmatrix} \tag{4.4}$$

Therefore, the eight parameters describing this parallel projection are:

- Two components of the direction vector (L, M);
- Three rotation angles of the scene plane (ω, φ, κ);
- Two shift values (Δx, Δy); and
- Scale value (s),

and will be called "scene parallel projection parameters". N, the third component of the projection vector, can be determined using Equation 4.1, and λ can be found using the third equation of Equations 4.4, which is computed in Equation 4.6. In summary, the non-linear form of the parallel projection model includes four equations (Equations 4.4 and 4.1) and contains ten parameters (the parallel projection parameters together with N and λ). In the following section, a linear form of the parallel projection model is derived

4.4.2 Alternative Linear Mathematical Model

Equations 4.4 can be written as:

$$\begin{aligned}
x &= s.\lambda\left(r_{11}L + r_{21}M + r_{31}N\right) + s\left(r_{11}X + r_{21}Y + r_{31}Z\right) + \Delta x \\
y &= s.\lambda\left(r_{12}L + r_{22}M + r_{32}N\right) + s\left(r_{12}X + r_{22}Y + r_{32}Z\right) + \Delta y \\
0 &= s.\lambda\left(r_{13}L + r_{23}M + r_{33}N\right) + s\left(r_{13}X + r_{23}Y + r_{33}Z\right) + 0
\end{aligned} \tag{4.5}$$

From the third equation, λ can be computed as follows:

$$\lambda = -\frac{r_{13}X + r_{23}Y + r_{33}Z}{r_{13}L + r_{23}M + r_{33}N} \tag{4.6}$$

Substituting this value of λ into the first and second equations of Equations 4.5 results in:

$$\begin{aligned}
x &= -s\frac{r_{13}X + r_{23}Y + r_{33}Z}{r_{13}L + r_{23}M + r_{33}N}\left(r_{11}L + r_{21}M + r_{31}N\right) + s\left(r_{11}X + r_{21}Y + r_{31}Z\right) + \Delta x \\
y &= -s\frac{r_{13}X + r_{23}Y + r_{33}Z}{r_{13}L + r_{23}M + r_{33}N}\left(r_{12}L + r_{22}M + r_{32}N\right) + s\left(r_{12}X + r_{22}Y + r_{32}Z\right) + \Delta y
\end{aligned}$$

Rearranging, the above equations can be rewritten as:

$$\begin{aligned}
x &= s\left(r_{11} - \frac{r_{13}\left(r_{11}L + r_{21}M + r_{31}N\right)}{r_{13}L + r_{23}M + r_{33}N}\right)X + s\left(r_{21} - \frac{r_{23}\left(r_{11}L + r_{21}M + r_{31}N\right)}{r_{13}L + r_{23}M + r_{33}N}\right)Y \\
&\quad + s\left(r_{31} - \frac{r_{33}\left(r_{11}L + r_{21}M + r_{31}N\right)}{r_{13}L + r_{23}M + r_{33}N}\right)Z + \Delta x \\
y &= s\left(r_{12} - \frac{r_{13}\left(r_{12}L + r_{22}M + r_{32}N\right)}{r_{13}L + r_{23}M + r_{33}N}\right)X + s\left(r_{22} - \frac{r_{23}\left(r_{12}L + r_{22}M + r_{32}N\right)}{r_{13}L + r_{23}M + r_{33}N}\right)Y \\
&\quad + s\left(r_{32} - \frac{r_{33}\left(r_{12}L + r_{22}M + r_{32}N\right)}{r_{13}L + r_{23}M + r_{33}N}\right)Z + \Delta y
\end{aligned} \tag{4.7}$$

Let us assign U and V values as follows:

$$\begin{aligned} U &= \frac{r_{11}L + r_{21}M + r_{31}N}{r_{13}L + r_{23}M + r_{33}N} \\ V &= \frac{r_{12}L + r_{22}M + r_{32}N}{r_{13}L + r_{23}M + r_{33}N} \end{aligned} \tag{4.8}$$

Consequently, Equations 4.7 can be rewritten as:

$$\begin{aligned} x &= s(r_{11} - r_{13}U)X + s(r_{21} - r_{23}U)Y + s(r_{31} - r_{33}U)Z + \Delta x \\ y &= s(r_{12} - r_{13}V)X + s(r_{22} - r_{23}V)Y + s(r_{32} - r_{33}V)Z + \Delta y \end{aligned} \tag{4.9}$$

More concisely, Equations 4.9 can be written in the following form:

$$\begin{aligned} x &= A_1X + A_2Y + A_3Z + A_4 \\ y &= A_5X + A_6Y + A_7Z + A_8 \end{aligned} \tag{4.10}$$

Where:

$$\begin{aligned} A_1 &= s(r_{11} - r_{13}U) \\ A_2 &= s(r_{21} - r_{23}U) \\ A_3 &= s(r_{31} - r_{33}U) \\ A_4 &= \Delta x \\ A_5 &= s(r_{12} - r_{13}V) \\ A_6 &= s(r_{22} - r_{23}V) \\ A_7 &= s(r_{32} - r_{33}V) \\ A_8 &= \Delta y \end{aligned} \tag{4.11}$$

Equations 4.10 are linear functions between the scene coordinates (*x*, *y*) and the object coordinates (*X*, *Y*, *Z*), which constitute a **2-D Affine transformation** (Okamoto, 1992; and Okamoto et al., 1992; Okamoto et al., 1996; Ono et al., 1996; Okamoto and Fraser, 1998; Ono et al., 1999; Fraser, 2000; Hattori et al., 2000). One has to note that the 2-D Affine transformation involves two equations and eight parameters (A_1 to A_8), which is consistent with the non-linear parallel projection model (four equations and ten parameters).

Comparing Equations 4.10 and 4.4, the former equations are more suitable if point correspondences (control points) in both the scene and object space are available. In this case, the 2-D Affine parameters can be determined using a least-squares adjustment (if more than four control points are available) without the need for linearizing the model and obtaining approximations of the parameters through an iterative process. In conclusion, with the existence of control points, the 2-D Affine model is superior in terms of efficiency of computations. However, it is worth mentioning that navigation data, if available, are easier to incorporate using the non-linear model (Equations 4.4) since the mathematical relationship between the parallel projection and the navigation parameters can be established. This will be discussed in Section 5.4, Chapter 5.

4.4.3 Special Case: Parallel Projection between Two Planar Surfaces

An interesting special case occurs when the parallel projection is between two planar surfaces: that is, between scene and planar object space. In this case, Z in Equations 4.10 can be replaced using the plane equation ($aX+bY+c$) as:

$$\begin{aligned} x &= A_1X + A_2Y + A_3(aX + bY + c) + A_4 \\ y &= A_5X + A_6Y + A_7(aX + bY + c) + A_8 \end{aligned}$$

$$\begin{aligned} x &= (A_1 + aA_3)X + (A_2 + bA_3)Y + (A_4 + cA_3) \\ y &= (A_5 + aA_7)X + (A_6 + bA_7)Y + (A_8 + cA_7) \end{aligned}$$

$$\begin{aligned} x &= a_1X + a_2Y + a_3 \\ y &= a_4X + a_5Y + a_6 \end{aligned} \tag{4.12}$$

Where:

$$\begin{aligned} a_1 &= A_1 + aA_3 \\ a_2 &= A_2 + bA_3 \\ a_3 &= A_4 + cA_3 \\ a_4 &= A_5 + aA_7 \\ a_5 &= A_6 + bA_7 \\ a_6 &= A_8 + cA_7 \end{aligned}$$

Equations 4.12 define the standard Affine transformation, Figure 4.6a.

4.4.4 Transformation from 2-D Affine Parameters to Scene Parallel Projection Parameters

It is important to note that the parameters in Equations 4.4 are more related to the navigation data (EOP of the sensor) than those in Equations 4.10. In addition, they will be used for epipolar resampling, as will be explained in Chapter 6. Therefore, it is important to derive the transformation from 2-D Affine parameters to scene parallel projection parameters, while the inverse transformation has been previously established (Equations 4.8 and 4.11).

Δx and *Δy* can be computed directly from Equations 4.11. To solve for the direction vector (*L*, *M*, *N*), Equations 4.8 can be rewritten as:

$$\begin{aligned} L(r_{11} - U.r_{13}) + M(r_{21} - U.r_{23}) + N(r_{31} - U.r_{33}) = 0 \\ L(r_{12} - V.r_{13}) + M(r_{22} - V.r_{23}) + N(r_{32} - V.r_{33}) = 0 \end{aligned}$$

Multiplying the above equations by *s* results in:

$$\begin{aligned} LA_1 + MA_2 + NA_3 = 0 \\ LA_5 + MA_6 + NA_7 = 0 \end{aligned} \qquad (4.13)$$

Rearranging and dividing the first by the second equations of Equations 4.13 results in:

$$\frac{LA_1 + MA_2}{LA_5 + MA_6} = \frac{A_3}{A_7} \qquad (4.14)$$

$$M = L\frac{A_1A_7 - A_3A_5}{A_3A_6 - A_2A_7} \qquad (4.15)$$

The first line of Equations 4.13 can be rewritten as:

$$N^2 = \frac{(LA_1 + MA_2)^2}{A_3^2} \tag{4.16}$$

Substituting Equation 4.16 into Equation 4.1 and rearranging results in:

$$L^2 + L^2 \frac{A_1^2}{A_3^2} + M^2 + M^2 \frac{A_2^2}{A_3^2} + 2LM \frac{A_1 A_2}{A_3^2} = 1 \tag{4.17}$$

Using Equations 4.15 And 4.17, *L* can be computed as follows:

$$L = \pm \frac{A_3}{\sqrt{\left(\frac{A_1A_7 - A_3A_5}{A_3A_6 - A_2A_7}\right)^2 \left(A_2^2 + A_3^2\right) + \left(\frac{A_1A_7 - A_3A_5}{A_3A_6 - A_2A_7}\right) 2A_1A_2 + A_1^2 + A_3^2}} \tag{4.18}$$

After *L* is obtained from Equation 4.18, *M* is directly solved using Equation 4.15. To avoid the sign ambiguity in *L* and *M*, *N* has to be computed from Equations 4.13 and not from Equations 4.1 or 4.16. From Equation 4.1, it is assumed that *N* is always positive (i.e., the direction vector points upwards). Therefore, the sign of *N* that is obtained from Equations 4.13 can be used to resolve for the sign ambiguities in *L* and *M*.

To determine the scale factor *s*, let us define T_1, T_2 and T_3 as follows:

$$\begin{aligned} T_1 &= A_1^2 + A_2^2 + A_3^2 \\ T_2 &= A_5^2 + A_6^2 + A_7^2 \\ T_3 &= A_1A_5 + A_2A_6 + A_3A_7 \end{aligned} \tag{4.19}$$

Substituting for the values of A_1, A_2, A_3, A_5, A_6, and A_7 from Equations 4.11 into Equations 4.19 results in:

$$
\begin{aligned}
T_1 &= s^2\left[\left(r_{11}^2 + r_{21}^2 + r_{31}^2\right) + U^2\left(r_{13}^2 + r_{23}^2 + r_{33}^2\right) - 2U\left(r_{11}r_{13} + r_{21}r_{23} + r_{31}r_{33}\right)\right] \\
T_2 &= s^2\left[\left(r_{12}^2 + r_{22}^2 + r_{32}^2\right) + V^2\left(r_{13}^2 + r_{23}^2 + r_{33}^2\right) - 2U\left(r_{12}r_{13} + r_{22}r_{23} + r_{32}r_{33}\right)\right] \\
T_3 &= s^2\left[\left(r_{11}r_{12} + r_{21}r_{22} + r_{31}r_{32}\right) + UV\left(r_{13}^2 + r_{23}^2 + r_{33}^2\right) - V\left(r_{11}r_{13} + r_{21}r_{23} + r_{31}r_{33}\right)\right. \\
&\qquad \left. - U\left(r_{12}r_{13} + r_{22}r_{23} + r_{32}r_{33}\right)\right]
\end{aligned}
\tag{4.20}
$$

Using the orthonormality properties of rotation matrices (Equations A.11, A.12, A.13, A.17, A.18 and A.19, Appendix A), the values of T_1, T_2 and T_3 can be written as follows:

$$
\begin{aligned}
T_1 &= s^2\left(1 + U^2\right) \\
T_2 &= s^2\left(1 + V^2\right) \\
T_3 &= s^2\left(UV\right)
\end{aligned}
\tag{4.21}
$$

Dividing the first and second equations of Equations 4.21 by the third one, scale s is eliminated and the following ratios are obtained:

$$
\frac{T_1}{T_3} = \frac{1 + U^2}{UV} \tag{4.22}
$$

$$
\frac{T_2}{T_3} = \frac{1 + V^2}{UV} \tag{4.23}
$$

Equation 4.22 can be rewritten as:

$$
V = \frac{T_3}{T_1}\frac{\left(1 + U^2\right)}{U} \tag{4.24}
$$

Substituting the value of V into Equation 4.23 results in:

$$
U^4\left(T_3^2 - T_1T_2\right) + U^2\left(2T_3^2 + T_1^2 - T_1T_2\right) + \left(T_3^2\right) = 0 \tag{4.25}
$$

Which is a quadratic form in U^2. Now, let us define A, B and C as follows:

$$\begin{aligned} A &= T_3^2 - T_1T_2 \\ B &= 2T_3^2 + T_1^2 - T_1T_2 \\ C &= T_3^2 \end{aligned} \tag{4.26}$$

Consequently, the solution of U^2 will be as follows:

$$U^2 = \frac{-B \pm \sqrt{B^2 - 4AC}}{2A} \tag{4.27}$$

Experimentally, it is found that the positive solution of the square root of Equation 4.27 yields a value of U^2 that is always negative, which is a rejected solution. On the other hand, the negative sign of the square root always produces a positive value of U^2, and is accepted as a solution.

Moreover, the experiments showed that if $L > 0$, then the value of U equals the positive square root of U^2. Otherwise, it equals the negative square root of U^2.

After resolving the ambiguity in the value of U, Equation 4.24 is then used to compute V. Finally, s is computed from the following equation, which is derived from the first equation of Equations 4.21:

$$s = \sqrt{\frac{T_1}{1+U^2}} \tag{4.28}$$

To solve for the rotation angles, substituting for r_{11} and r_{13}, the A_1-equation of Equations 4.11 can be rewritten as:

$$A_1 = s(\cos\varphi \cos\kappa - U \sin\varphi)$$

Rearranging, the above equation can be rewritten as:

$$\cos\kappa = \frac{U\sin\varphi + \frac{A_1}{s}}{\cos\varphi} \tag{4.29}$$

Referring to Figure 4.8, sin(*κ*) can be derived from cos(*κ*) as follows:

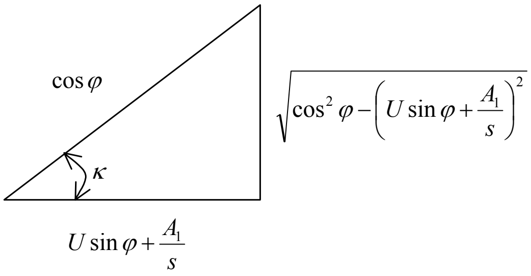

Figure 4.8: From cos(*κ*) to sin(*κ*)

$$\sin\kappa = \frac{\sqrt{\cos^2\varphi - U^2\sin^2\varphi - \frac{A_1^2}{s^2} - 2\frac{A_1}{s}U\sin\varphi}}{\cos\varphi} \tag{4.30}$$

Squaring both sides results in:

$$\sin^2\kappa = \frac{\cos^2\varphi - U^2\sin^2\varphi - \frac{A_1^2}{s^2} - 2\frac{A_1}{s}U\sin\varphi}{\cos^2\varphi} \tag{4.31}$$

A_5-equation of Equations 4.11, substituting for r_{12} and r_{13}, can be rewritten as:

$$A_5 = s(-\cos\varphi\sin\kappa - V\sin\varphi)$$

$$\sin\kappa = \frac{-V\sin\varphi + \frac{A_5}{s}}{\cos\varphi} \tag{4.32}$$

Squaring both sides results in:

$$\sin^2\kappa = \frac{V^2\sin^2\varphi + \frac{A_5^2}{s^2} + 2\frac{A_5}{s}V\sin\varphi}{\cos^2\varphi} \tag{4.33}$$

Equating the right side of Equations 4.31 and 4.33, and exploiting the fact that ($\cos^2\varphi = 1 - \sin^2\varphi$) result in:

$$\sin^2\varphi\left(U^2 + V^2 + 1\right) + \sin\varphi\left(2U\frac{A_1}{s} + 2V\frac{A_5}{s}\right) + \left(\frac{A_1^2}{s^2} + \frac{A_5^2}{s^2} - 1\right) = 0 \tag{4.34}$$

which is a quadratic form in sin(φ). Let us define *D*, *E* and *F* as follows:

$$\begin{aligned} D &= U^2 + V^2 + 1 \\ E &= 2U\frac{A_1}{s} + 2V\frac{A_5}{s} \\ F &= \frac{A_1^2}{s^2} + \frac{A_5^2}{s^2} - 1 \end{aligned} \tag{4.35}$$

Substituting again in Equation 4.34 yields:

$$\sin\varphi = \frac{-E \pm \sqrt{E^2 - 4DF}}{2D} \tag{4.36}$$

Experimentally, it is found that, when $L > 0$, the positive square root in Equation 4.36 gives the correct value of sin(φ). Otherwise, the negative square root gives the correct value of sin(φ).

It is important to note that the range of φ is only from -π/2 to +π/2. Therefore, if sin(φ) is positive, the value of φ will range from 0 to +π/2; otherwise, it will change from -π/2 to 0.

The value of κ can range from -π to +π, and hence both Equations 4.29 and 4.32 must be used to solve for κ.

The A_2-equation and A_3-equation of Equations 4.11, substituting for r_{21}, r_{23} , r_{22} and r_{23}, can be explicitly expressed as:

$$\begin{aligned} A_2 &= s(\cos\omega(\sin\kappa) + \sin\omega(\sin\varphi\cos\kappa + U\cos\varphi)) \\ A_3 &= s(\cos\omega(-\sin\varphi\cos\kappa - U\cos\varphi) + \sin\omega(\sin\kappa)) \end{aligned}$$

Rearranging these two equations results in:

$$\begin{bmatrix} \sin\kappa & \sin\varphi\cos\kappa + U\cos\varphi \\ -\sin\varphi\cos\kappa - U\cos\varphi & \sin\kappa \end{bmatrix} \begin{bmatrix} \cos\omega \\ \sin\omega \end{bmatrix} = \begin{bmatrix} \frac{A_2}{s} \\ \frac{A_3}{s} \end{bmatrix}$$

Sin(ω) can be computed as follows:

$$\sin\omega = \frac{\frac{A_2}{s}\sin\varphi\cos\kappa + \frac{A_2}{s}U\cos\varphi + \frac{A_3}{s}\sin\kappa}{\sin^2\kappa + (\sin\varphi\cos\kappa + U\cos\varphi)^2} \tag{4.37}$$

The range of ω varies from -π/2 to +π/2 and can be exclusively determined using the sin(ω) expression of Equation 4.37.

Finally, the procedure for transforming the 2-D Affine parameters to the scene parallel projection parameters is summarized as follows:

1. Use the fourth and eighth equations of Equations 4.11 to solve for Δx and Δy, respectively.

2. Use Equation 4.18 to solve for L, then Equation 4.15 to solve for M and, finally, Equation 4.13 to solve for N.

3. Compute T_1, T_2 and T_3 using Equations 4.19.

4. Use Equation 4.27 to solve for U, Equation 4.24 to solve for V, and Equation 4.28 to solve for s.

5. Use Equation 4.36 to solve for φ, then both of the Equations 4.29 and 4.32 to solve for κ and, finally, Equation 4.37 to solve for ω.

4.5 PARALLEL PROJECTION FROM NON-PLANAR SURFACE TO TWO PLANAR SCENES.

4.5.1 Mathematical Model

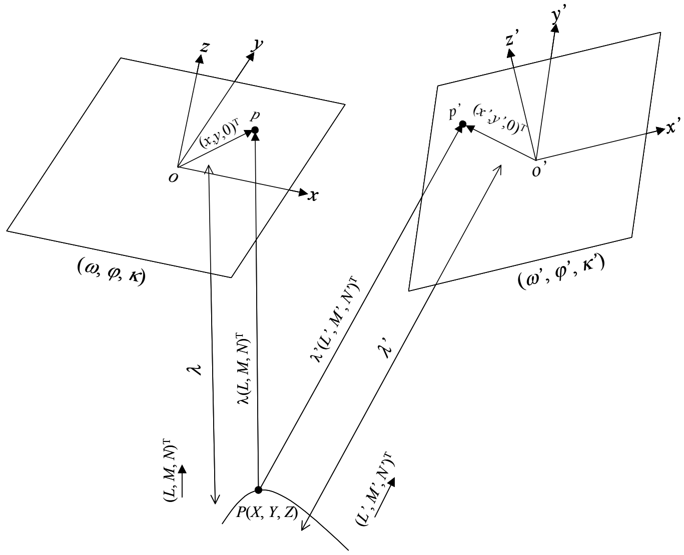

Figure 4.9: Parallel projection from object space to two scenes

Ono et al. (1999) proved that, by using 2-D Affine model, epipolar lines become straight lines. In this section, epipolar line parameters will be derived from scene parallel projection parameters (or 2-D Affine parameters). Recall that the transformation between scene parallel projection parameters and 2-D Affine parameters has already been established in the previous section.

Figure 4.9 shows two scenes in general positions and attitudes. Object space point *P* is imaged in the left and right scenes as point *p* and *p'*, respectively, through the direction vectors $(L, M, N)^{\mathrm{T}}$ and $(L', M', N')^{\mathrm{T}}$, respectively.

Two sets of equations relating the object space point to the two scene points can be rewritten, similar to Equations 4.4, as follows:

$$\begin{bmatrix} x' \\ y' \\ 0 \end{bmatrix} = s'.\lambda'.R'^{T}.\begin{bmatrix} L' \\ M' \\ N' \end{bmatrix} + s'.R'^{T}.\begin{bmatrix} X \\ Y \\ Z \end{bmatrix} + \begin{bmatrix} \Delta x' \\ \Delta y' \\ 0 \end{bmatrix}$$

where:

(x', y') are the scene coordinates of the corresponding point p' in the right scene;

λ' is spatial distance between point *P* and its image on the right scene p';

R' is the rotation matrix of the right scene coordinate system with respect to the object coordinate system, defined by the three angles $(\omega', \varphi', \kappa')$;

(L', M', N') is the direction vector for the parallel projection of the right scene; and

$(L', M', \omega', \varphi', \kappa', \Delta x', \Delta y', s')$ are the right scene parallel projection parameters.

Rearranging, the above equations can be rewritten as:

$$\begin{bmatrix} X \\ Y \\ Z \end{bmatrix} = \frac{1}{s}R\begin{bmatrix} x - \Delta x \\ y - \Delta y \\ 0 \end{bmatrix} - \lambda\begin{bmatrix} L \\ M \\ N \end{bmatrix}$$

$$\begin{bmatrix} X \\ Y \\ Z \end{bmatrix} = \frac{1}{s'}R'\begin{bmatrix} x' - \Delta x' \\ y' - \Delta y' \\ 0 \end{bmatrix} - \lambda'\begin{bmatrix} L' \\ M' \\ N' \end{bmatrix}$$

Equating the object coordinates (*X*, *Y*, *Z*) in the above equations results in:

$$\frac{1}{s}R\begin{bmatrix} x-\Delta x \\ y-\Delta y \\ 0 \end{bmatrix} - \lambda\begin{bmatrix} L \\ M \\ N \end{bmatrix} = \frac{1}{s'}R'\begin{bmatrix} x'-\Delta x' \\ y'-\Delta y' \\ 0 \end{bmatrix} - \lambda'\begin{bmatrix} L' \\ M' \\ N' \end{bmatrix}$$

$$\begin{bmatrix} x \\ y \\ 0 \end{bmatrix} = \begin{bmatrix} \Delta x \\ \Delta y \\ 0 \end{bmatrix} + s.\lambda.R^T\begin{bmatrix} L \\ M \\ N \end{bmatrix} + \frac{s}{s'}R^T R'\begin{bmatrix} x'-\Delta x' \\ y'-\Delta y' \\ 0 \end{bmatrix} - s.\lambda'.R^T\begin{bmatrix} L' \\ M' \\ N' \end{bmatrix} \tag{4.38}$$

Equations 4.38 express the relation between the left and right scene coordinates, which is equivalent to the coplanarity condition for images captured according to perspective projection (Refer to Section 2.2.2.2 in Chapter 2).

Another way to express this relation is to use the linear model (2-D Affine) for each of the scenes, as follows:

$$\begin{aligned} x &= A_1X + A_2Y + A_3Z + A_4 \\ y &= A_5X + A_6Y + A_7Z + A_8 \end{aligned} \tag{4.39}$$

$$\begin{aligned} x' &= A'_1\,X + A'_2\,Y + A'_3\,Z + A'_4 \\ y' &= A'_5\,X + A'_6\,Y + A'_7\,Z + A'_8 \end{aligned} \tag{4.40}$$

Where, A_1 to A_8 are the 2-D Affine parameters for the left scene, and A'_1 to A'_8 are the 2-D Affine parameters for the right scene.

Equations 4.39 can be rewritten as:

$$\begin{aligned} \begin{bmatrix} X \\ Y \end{bmatrix} &= \begin{bmatrix} A_1 & A_2 \\ A_5 & A_6 \end{bmatrix}^{-1}\begin{bmatrix} x - A_3Z - A_4 \\ y - A_7Z - A_8 \end{bmatrix} \\ &= \begin{bmatrix} A_1 & A_2 \\ A_5 & A_6 \end{bmatrix}^{-1}\begin{bmatrix} x \\ y \end{bmatrix} - \begin{bmatrix} A_1 & A_2 \\ A_5 & A_6 \end{bmatrix}^{-1}\begin{bmatrix} A_3 \\ A_7 \end{bmatrix}Z - \begin{bmatrix} A_1 & A_2 \\ A_5 & A_6 \end{bmatrix}^{-1}\begin{bmatrix} A_4 \\ A_8 \end{bmatrix} \end{aligned}$$

Substituting in Equations 4.40 produces:

$$
\begin{aligned}
\begin{bmatrix} x' \\ y' \end{bmatrix} &= \begin{bmatrix} A'_1 & A'_2 \\ A'_5 & A'_6 \end{bmatrix}\begin{bmatrix} X \\ Y \end{bmatrix} + \begin{bmatrix} A'_3 \\ A'_7 \end{bmatrix} Z + \begin{bmatrix} A'_4 \\ A'_8 \end{bmatrix} \\
&= \begin{bmatrix} A'_1 & A'_2 \\ A'_5 & A'_6 \end{bmatrix}\left(\begin{bmatrix} A_1 & A_2 \\ A_5 & A_6 \end{bmatrix}^{-1}\begin{bmatrix} x \\ y \end{bmatrix} - \begin{bmatrix} A_1 & A_2 \\ A_5 & A_6 \end{bmatrix}^{-1}\begin{bmatrix} A_3 \\ A_7 \end{bmatrix} Z - \begin{bmatrix} A_1 & A_2 \\ A_5 & A_6 \end{bmatrix}^{-1}\begin{bmatrix} A_4 \\ A_8 \end{bmatrix} \right) \\
&\quad + \begin{bmatrix} A'_3 \\ A'_7 \end{bmatrix} Z + \begin{bmatrix} A'_4 \\ A'_8 \end{bmatrix} \\
&= \left(\begin{bmatrix} A'_1 & A'_2 \\ A'_5 & A'_6 \end{bmatrix}\begin{bmatrix} A_1 & A_2 \\ A_5 & A_6 \end{bmatrix}^{-1} \right)\begin{bmatrix} x \\ y \end{bmatrix} + \left(\begin{bmatrix} A'_3 \\ A'_7 \end{bmatrix} - \begin{bmatrix} A'_1 & A'_2 \\ A'_5 & A'_6 \end{bmatrix}\begin{bmatrix} A_1 & A_2 \\ A_5 & A_6 \end{bmatrix}^{-1}\begin{bmatrix} A_3 \\ A_7 \end{bmatrix} \right) Z \\
&\quad + \left(\begin{bmatrix} A'_4 \\ A'_8 \end{bmatrix} - \begin{bmatrix} A'_1 & A'_2 \\ A'_5 & A'_6 \end{bmatrix}\begin{bmatrix} A_1 & A_2 \\ A_5 & A_6 \end{bmatrix}^{-1}\begin{bmatrix} A_4 \\ A_8 \end{bmatrix} \right)
\end{aligned}
$$

The above equations can be rewritten as:

$$
\begin{bmatrix} x' \\ y' \end{bmatrix} = \begin{bmatrix} B_1 & B_2 \\ B_5 & B_6 \end{bmatrix}\begin{bmatrix} x \\ y \end{bmatrix} + \begin{bmatrix} B_3 \\ B_7 \end{bmatrix} Z + \begin{bmatrix} B_4 \\ B_8 \end{bmatrix}
$$

$$
\begin{aligned}
x' &= B_1 x + B_2 y + B_3 Z + B_4 \\
y' &= B_5 x + B_6 y + B_7 Z + B_8
\end{aligned}
\tag{4.41}
$$

Where:

$$
\begin{aligned}
\begin{bmatrix} B_1 & B_2 \\ B_5 & B_6 \end{bmatrix} &= \begin{bmatrix} A'_1 & A'_2 \\ A'_5 & A'_6 \end{bmatrix}\begin{bmatrix} A_1 & A_2 \\ A_5 & A_6 \end{bmatrix}^{-1} \\
\begin{bmatrix} B_3 \\ B_7 \end{bmatrix} &= \begin{bmatrix} A'_3 \\ A'_7 \end{bmatrix} - \begin{bmatrix} A'_1 & A'_2 \\ A'_5 & A'_6 \end{bmatrix}\begin{bmatrix} A_1 & A_2 \\ A_5 & A_6 \end{bmatrix}^{-1}\begin{bmatrix} A_3 \\ A_7 \end{bmatrix} \\
\begin{bmatrix} B_4 \\ B_8 \end{bmatrix} &= \begin{bmatrix} A'_4 \\ A'_8 \end{bmatrix} - \begin{bmatrix} A'_1 & A'_2 \\ A'_5 & A'_6 \end{bmatrix}\begin{bmatrix} A_1 & A_2 \\ A_5 & A_6 \end{bmatrix}^{-1}\begin{bmatrix} A_4 \\ A_8 \end{bmatrix}
\end{aligned}
$$

From the first equation of Equations 4.41, *Z* is computed as:

$$Z = \frac{1}{B_3}x' - \frac{B_1}{B_3}x - \frac{B_2}{B_3}y - \frac{B_4}{B_3}$$

Substituting in the second equation of Equations 4.41 results in:

$$\begin{aligned} y' &= B_5 x + B_6 y + B_7\left(\frac{1}{B_3}x' - \frac{B_1}{B_3}x - \frac{B_2}{B_3}y - \frac{B_4}{B_3}\right) + B_8 \\ &= \left(\frac{B_7}{B_3}\right)x' + \left(B_5 - \frac{B_7 B_1}{B_3}\right)x + \left(B_6 - \frac{B_7 B_4}{B_3}\right)y + \left(B_8 - \frac{B_7 B_4}{B_3}\right) \\ y' &= C_1 x' + C_2 x + C_3 y + C_4 \end{aligned} \qquad (4.42)$$

Where:

$$C_1 = \frac{B_7}{B_3}$$

$$C_2 = B_5 - \frac{B_7 B_1}{B_3}$$

$$C_3 = B_6 - \frac{B_7 B_4}{B_3}$$

$$C_4 = B_8 - \frac{B_7 B_4}{B_3}$$

which is similar to the equation derived by Ono et al. (1999). Before analyzing Equation 4.42, it is important to recall the definition of the epipolar line for a point in a scene as the locus of all possible conjugate points in the other scene, based on the orientation parameters. Therefore, for a given point (x, y) in the left image, Equation 4.42 becomes a linear function in x' and y', which is the equation of the locus of the conjugate point in the right scene, and consequently the equation of the corresponding epipolar line in the right scene. One must note that epipolar lines become straight lines by adopting parallel projection.

In the following sections, two special cases of the parallel projection, which will be used in epipolar resampling (Chapter 6), are developed.

4.5.2 Special Case: Same Direction Vector and Two Planar Scenes

This case is important for projecting the scene into a different plane, which is a part of the epipolar resampling approach (as will be explained in Section 6.3, Chapter 6). Figure 4.10 shows two scenes that are constructed from parallel projection using the same direction vector $(L, M, N)^T$.

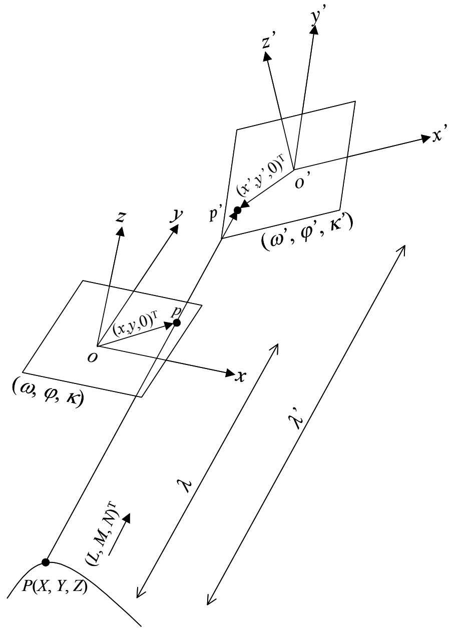

Figure 4.10: Parallel projection from object space to two planar scenes along the same direction

Equations 4.38 can be written for this special case as:

$$\begin{bmatrix} x \\ y \\ 0 \end{bmatrix} = \begin{bmatrix} \Delta x \\ \Delta y \\ 0 \end{bmatrix} + s(\lambda - \lambda')R^T \begin{bmatrix} L \\ M \\ N \end{bmatrix} + \frac{s}{s'} R^T R' \begin{bmatrix} x' - \Delta x' \\ y' - \Delta y' \\ 0 \end{bmatrix}$$

$$\begin{bmatrix} x \\ y \\ 0 \end{bmatrix} = \begin{bmatrix} \Delta x \\ \Delta y \\ 0 \end{bmatrix} + s.\Delta\lambda.R^T \begin{bmatrix} L \\ M \\ N \end{bmatrix} + S.M^T \begin{bmatrix} x' - \Delta x' \\ y' - \Delta y' \\ 0 \end{bmatrix} \tag{4.43}$$

Where:

$$\Delta\lambda = \lambda - \lambda'$$

$$S = \frac{s}{s'}$$

$$M^T = R^T R' = \begin{bmatrix} m_{11} & m_{21} & m_{31} \\ m_{12} & m_{22} & m_{32} \\ m_{13} & m_{23} & m_{33} \end{bmatrix}$$

Equations 4.43 can be written as:

$$\begin{aligned} x &= \Delta x + s.\Delta\lambda\left(r_{11}L + r_{21}M + r_{31}N\right) + S\left(m_{11}\left(x' - \Delta x'\right) + m_{21}\left(y' - \Delta y'\right)\right) \\ y &= \Delta y + s.\Delta\lambda\left(r_{12}L + r_{22}M + r_{32}N\right) + S\left(m_{12}\left(x' - \Delta x'\right) + m_{22}\left(y' - \Delta y'\right)\right) \\ 0 &= 0 + s.\Delta\lambda\left(r_{13}L + r_{23}M + r_{33}N\right) + S\left(m_{13}\left(x' - \Delta x'\right) + m_{23}\left(y' - \Delta y'\right)\right) \end{aligned} \tag{4.44}$$

Δλ can be derived from the third equation of Equation 4.44 as follows:

$$\begin{aligned} \Delta\lambda &= -\frac{S\left(m_{13}\left(x' - \Delta x'\right) + m_{23}\left(y' - \Delta y'\right)\right)}{s\left(r_{13}L + r_{23}M + r_{33}N\right)} \\ &= -\frac{\left(m_{13}\left(x' - \Delta x'\right) + m_{23}\left(y' - \Delta y'\right)\right)}{s'\left(r_{13}L + r_{23}M + r_{33}N\right)} \\ &= -\left(\frac{m_{13}}{s'\left(r_{13}L + r_{23}M + r_{33}N\right)}\right)x' - \left(\frac{m_{23}}{s'\left(r_{13}L + r_{23}M + r_{33}N\right)}\right)y' + \left(\frac{m_{13}\Delta x' + m_{23}\Delta y'}{s'\left(r_{13}L + r_{23}M + r_{33}N\right)}\right) \end{aligned}$$

Substituting the value of *Δλ* in the first and second equations of Equations 4.44 results in:

$$\begin{aligned} x &= \left(S\left(m_{11} - \frac{m_{13}\left(r_{11}L + r_{21}M + r_{31}N\right)}{\left(r_{13}L + r_{23}M + r_{33}N\right)}\right)\right)x' + \left(S\left(m_{21} - \frac{m_{23}\left(r_{11}L + r_{21}M + r_{31}N\right)}{\left(r_{13}L + r_{23}M + r_{33}N\right)}\right)\right)y' \\ &\quad + \left(\Delta x + S\left(\frac{\left(m_{13}\Delta x' + m_{23}\Delta y'\right)\left(r_{11}L + r_{21}M + r_{31}N\right)}{\left(r_{13}L + r_{23}M + r_{33}N\right)} - \left(m_{11}\Delta x' + m_{21}\Delta y'\right)\right)\right) \\ y &= \left(S\left(m_{12} - \frac{m_{13}\left(r_{12}L + r_{22}M + r_{32}N\right)}{\left(r_{13}L + r_{23}M + r_{33}N\right)}\right)\right)x' + \left(S\left(m_{22} - \frac{m_{23}\left(r_{12}L + r_{22}M + r_{32}N\right)}{\left(r_{13}L + r_{23}M + r_{33}N\right)}\right)\right)y' \\ &\quad + \left(\Delta y + S\left(\frac{\left(m_{13}\Delta x' + m_{23}\Delta y'\right)\left(r_{12}L + r_{22}M + r_{32}N\right)}{\left(r_{13}L + r_{23}M + r_{33}N\right)} - \left(m_{12}\Delta x' + m_{22}\Delta y'\right)\right)\right) \end{aligned} \tag{4.45}$$

The above equations as can be rewritten as:

$$\begin{aligned} x &= b_1 x' + b_2 y' + b_3 \\ y &= b_4 x' + b_5 y' + b_6 \end{aligned} \tag{4.46}$$

Where:

$$\begin{aligned}
b_1 &= S\left(m_{11} - \frac{m_{13}\left(r_{11}L + r_{21}M + r_{31}N\right)}{\left(r_{13}L + r_{23}M + r_{33}N\right)} \right) \\
b_2 &= S\left(m_{21} - \frac{m_{23}\left(r_{11}L + r_{21}M + r_{31}N\right)}{\left(r_{13}L + r_{23}M + r_{33}N\right)} \right) \\
b_3 &= \Delta x + S\left(\frac{\left(m_{13}\Delta x' + m_{23}\Delta y'\right)\left(r_{11}L + r_{21}M + r_{31}N\right)}{\left(r_{13}L + r_{23}M + r_{33}N\right)} - \left(m_{11}\Delta x' + m_{21}\Delta y'\right) \right) \\
b_4 &= S\left(m_{12} - \frac{m_{13}\left(r_{12}L + r_{22}M + r_{32}N\right)}{\left(r_{13}L + r_{23}M + r_{33}N\right)} \right) \\
b_5 &= S\left(m_{22} - \frac{m_{23}\left(r_{12}L + r_{22}M + r_{32}N\right)}{\left(r_{13}L + r_{23}M + r_{33}N\right)} \right) \\
b_6 &= \Delta y + S\left(\frac{\left(m_{13}\Delta x' + m_{23}\Delta y'\right)\left(r_{12}L + r_{22}M + r_{32}N\right)}{\left(r_{13}L + r_{23}M + r_{33}N\right)} - \left(m_{12}\Delta x' + m_{22}\Delta y'\right) \right)
\end{aligned} \tag{4.47}$$

It is important to note that b_1 to b_6 are constants. Therefore, Equations 4.46 represent a standard Affine transformation. By comparing Equations 4.46 to Equations 4.12, the former is a parallel projection between two planar scenes, while the latter is a parallel projection between a scene plane and planar object space. In both cases, the mathematical model is standard Affine, because they represent projections between planar surfaces.

4.5.3 Special Case: Two Planar Scenes Along the Same Projection Plane

Figure 4.11 shows the special case of the parallel projection, where the two scenes belong to the same projection plane. The two scenes are considered to have the same ω and φ orientations, while having different κ orientations (κ for the left scene and κ' for the right scene).

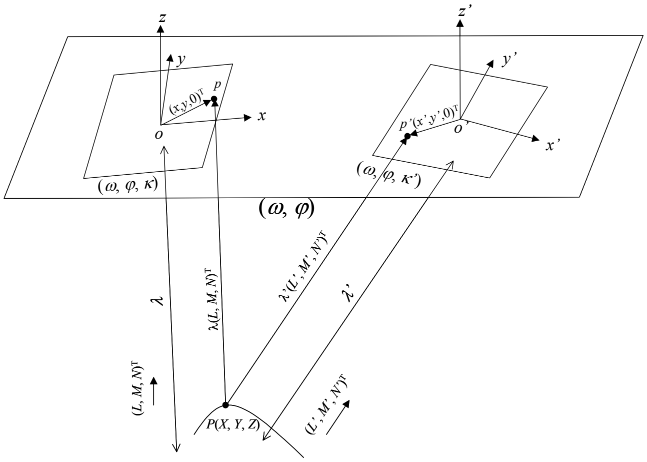

Figure 4.11: Parallel projection from object space to two scenes having the same orientation

The rotation matrices R and R' of the left and right scenes can be written as:

$$R = \begin{bmatrix} r_{11} & r_{12} & r_{13} \\ r_{21} & r_{22} & r_{23} \\ r_{31} & r_{32} & r_{33} \end{bmatrix}$$

$$= R_{\omega} R_{\varphi} R_{\kappa}$$

$$= \begin{bmatrix} 1 & 0 & 0 \\ 0 & \cos\omega & -\sin\omega \\ 0 & \sin\omega & \cos\omega \end{bmatrix} \begin{bmatrix} \cos\varphi & 0 & \sin\varphi \\ 0 & 1 & 0 \\ -\sin\varphi & 0 & \cos\varphi \end{bmatrix} \begin{bmatrix} \cos\kappa & -\sin\kappa & 0 \\ \sin\kappa & \cos\kappa & 0 \\ 0 & 0 & 1 \end{bmatrix}$$

$$R' = \begin{bmatrix} r'_{11} & r'_{12} & r'_{13} \\ r'_{21} & r'_{22} & r'_{23} \\ r'_{31} & r'_{32} & r'_{33} \end{bmatrix}$$

$$= R_{\omega} R_{\varphi} R_{\kappa'}$$

$$= \begin{bmatrix} 1 & 0 & 0 \\ 0 & \cos\omega & -\sin\omega \\ 0 & \sin\omega & \cos\omega \end{bmatrix} \begin{bmatrix} \cos\varphi & 0 & \sin\varphi \\ 0 & 1 & 0 \\ -\sin\varphi & 0 & \cos\varphi \end{bmatrix} \begin{bmatrix} \cos\kappa' & -\sin\kappa' & 0 \\ \sin\kappa' & \cos\kappa' & 0 \\ 0 & 0 & 1 \end{bmatrix}$$

$R^{T}R'$ can be computed as follows:

$$\begin{aligned}
R^T R' &= \left(R_\omega R_\varphi R_\kappa\right)^T \left(R_\omega R_\varphi R_{\kappa'}\right) \\
&= R_\kappa^T R_\varphi^T R_\omega^T R_\omega R_\varphi R_{\kappa'} \\
&= R_\kappa^T R_\varphi^T R_\varphi R_{\kappa'} \\
&= R_\kappa^T R_{\kappa'} \\
&= \begin{bmatrix} \cos\kappa & \sin\kappa & 0 \\ -\sin\kappa & \cos\kappa & 0 \\ 0 & 0 & 1 \end{bmatrix} \begin{bmatrix} \cos\kappa' & -\sin\kappa' & 0 \\ \sin\kappa' & \cos\kappa' & 0 \\ 0 & 0 & 1 \end{bmatrix} \\
&= \begin{bmatrix} \cos\kappa\cos\kappa' + \sin\kappa\sin\kappa' & \sin\kappa\cos\kappa' - \cos\kappa\sin\kappa' & 0 \\ -\left(\sin\kappa\cos\kappa' - \cos\kappa\sin\kappa'\right) & \cos\kappa\cos\kappa' + \sin\kappa\sin\kappa' & 0 \\ 0 & 0 & 1 \end{bmatrix} \\
&= \begin{bmatrix} \cos(\kappa'-\kappa) & -\sin(\kappa'-\kappa) & 0 \\ \sin(\kappa'-\kappa) & \cos(\kappa'-\kappa) & 0 \\ 0 & 0 & 1 \end{bmatrix} \\
&= \begin{bmatrix} \cos\Delta\kappa & -\sin\Delta\kappa & 0 \\ \sin\Delta\kappa & \cos\Delta\kappa & 0 \\ 0 & 0 & 1 \end{bmatrix} \\
&= R_{\Delta\kappa}
\end{aligned}$$

where, remembering the orthonormality properties of rotation matrices (see Appendix A):

$$R_\omega^T R_\omega = R_\varphi^T R_\varphi = I \text{ and}$$

$$\Delta\kappa = \kappa' - \kappa$$

Substituting the expressions of $R^{\mathrm{T}}R'$ and $\Delta\kappa$ in Equations 4.38, the three equations can be rewritten as:

$$\begin{aligned}
x &= \Delta x + s.\lambda\left(r_{11}L + r_{21}M + r_{31}N\right) + \frac{s}{s'}\left((x'-\Delta x')\cos\Delta\kappa - (y'-\Delta y')\sin\Delta\kappa\right) \\
&\quad - s.\lambda'\left(r_{11}L' + r_{21}M' + r_{31}N'\right) \\
y &= \Delta y + s.\lambda\left(r_{12}L + r_{22}M + r_{32}N\right) + \frac{s}{s'}\left((x'-\Delta x')\sin\Delta\kappa + (y'-\Delta y')\cos\Delta\kappa\right) \\
&\quad - s.\lambda'\left(r_{12}L' + r_{22}M' + r_{32}N'\right) \\
0 &= 0 + s.\lambda\left(r_{13}L + r_{23}M + r_{33}N\right) + 0 - s.\lambda'\left(r_{13}L' + r_{23}M' + r_{33}N'\right)
\end{aligned} \tag{4.48}$$

The third equation of Equations 4.48 can be written as:

$$\lambda = \frac{r_{13}L'+r_{23}M'+r_{33}N'}{r_{13}L+r_{23}M+r_{33}N}\lambda' \tag{4.49}$$

Substituting the value of λ from Equation 4.49 into the first and second equations of Equations 4.48 results in:

$$\begin{aligned}
x &= \left(\frac{s}{s'}\cos\Delta\kappa\right)x'+\left(-\frac{s}{s'}\sin\Delta\kappa\right)y'+\left(s\left(r_{11}L+r_{21}M+r_{31}N\right)\frac{r_{13}L'+r_{23}M'+r_{33}N'}{r_{13}L+r_{23}M+r_{33}N}-s\left(r_{11}L'+r_{21}M'+r_{31}N'\right)\right)\lambda' \\
&+\left(\Delta x-\frac{s}{s'}\left(\Delta x'\cos\Delta\kappa-\Delta y'\sin\Delta\kappa\right)\right) \\
y &= \left(\frac{s}{s'}\sin\Delta\kappa\right)x'+\left(\frac{s}{s'}\cos\Delta\kappa\right)y'+\left(s\left(r_{12}L+r_{22}M+r_{32}N\right)\frac{r_{13}L'+r_{23}M'+r_{33}N'}{r_{13}L+r_{23}M+r_{33}N}-s\left(r_{12}L'+r_{22}M'+r_{32}N'\right)\right)\lambda' \\
&+\left(\Delta y-\frac{s}{s'}\left(\Delta x'\sin\Delta\kappa+\Delta y'\cos\Delta\kappa\right)\right)
\end{aligned}$$

These equations can be rewritten as:

$$\begin{aligned}
x &= c_1x'+c_2y'+c_3\lambda'+c_4 \\
y &= c_5x'+c_6y'+c_7\lambda'+c_8
\end{aligned} \tag{4.50}$$

Where:

$$\begin{aligned}
c_1 &= \frac{s}{s'}\cos\Delta\kappa \\
c_2 &= -\frac{s}{s'}\sin\Delta\kappa \\
c_3 &= s\left(r_{11}L+r_{21}M+r_{31}N\right)\frac{r_{13}L'+r_{23}M'+r_{33}N'}{r_{13}L+r_{23}M+r_{33}N}-s\left(r_{11}L'+r_{21}M'+r_{31}N'\right) \\
c_4 &= \Delta x-\frac{s}{s'}\left(\Delta x'\cos\Delta\kappa-\Delta y'\sin\Delta\kappa\right) \\
c_5 &= \frac{s}{s'}\sin\Delta\kappa \\
c_6 &= \frac{s}{s'}\cos\Delta\kappa \\
c_7 &= s\left(r_{12}L+r_{22}M+r_{32}N\right)\frac{r_{13}L'+r_{23}M'+r_{33}N'}{r_{13}L+r_{23}M+r_{33}N}-s\left(r_{12}L'+r_{22}M'+r_{32}N'\right) \\
c_8 &= \Delta y-\frac{s}{s'}\left(\Delta x'\sin\Delta\kappa+\Delta y'\cos\Delta\kappa\right)
\end{aligned} \tag{4.51}$$

It is important to note that *λ'* in Equations 4.50 can vary from one point to another. It can be computed from the first equation as:

$$\lambda' = \frac{1}{c_3}x - \frac{c_1}{c_3}x' - \frac{c_2}{c_3}y' - \frac{c_4}{c_3}$$

Substituting the value of *λ'* into the second equation of Equations 4.50 results in:

$$\begin{aligned} y &= c_5x' + c_6y' + c_7\left(\frac{1}{c_3}x - \frac{c_1}{c_3}x' - \frac{c_2}{c_3}y' - \frac{c_4}{c_3}\right) + c_8 \\ &= \left(\frac{c_7}{c_3}\right)x + \left(c_5 - \frac{c_1c_7}{c_3}\right)x' + \left(c_6 - \frac{c_2c_7}{c_3}\right)y' + \left(c_8 - \frac{c_4c_7}{c_3}\right) \\ y' &= \left(\frac{c_1c_7 - c_5c_3}{c_6c_3 - c_2c_7}\right)x' + \left(\frac{-c_7}{c_6c_3 - c_2c_7}\right)x + \left(\frac{c_3}{c_6c_3 - c_2c_7}\right)y + \left(\frac{c_4c_7 - c_8c_3}{c_6c_3 - c_2c_7}\right) \end{aligned}$$

The above equation can be rewritten as:

$$y' = C'_1\,x' + C'_2\,x + C'_3\,y + C'_4 \tag{4.52}$$

Where:

$$\begin{aligned} C'_1 &= \frac{c_1c_7 - c_5c_3}{c_6c_3 - c_2c_7} \\ C'_2 &= \frac{-c_7}{c_6c_3 - c_2c_7} \\ C'_3 &= \frac{c_3}{c_6c_3 - c_2c_7} \\ C'_4 &= \frac{c_4c_7 - c_8c_3}{c_6c_3 - c_2c_7} \end{aligned} \tag{4.53}$$

It is important to notice that Equation 4.52 is similar to Equation 4.42, except for the physical meaning of the involved parameters. More explicitly, parameters C_1 to C_4 in Equation 4.42 relate two scenes with general orientations, while parameters C'_1 to C'_4 in Equation 4.52 relate two scenes along the same projection plane. Therefore, if the two scenes are known to share the same plane, Equation 4.52 can be used – otherwise, Equation 4.42 has to be used. However, both equations are valid and can be used to determine the epipolar lines knowing the orientation parameters or point correspondences.

4.6 EXPERIMENTS

In this section, the mathematical models for parallel projection between object space and one scene (Experiments 4.1 and 4.2), and between object space and two scenes (Experiments 4.3 to 4.8) are verified.

Two surfaces are simulated, having parameters as listed in Table 4.1. Surface I is non-planar, while Surface II is planar. In addition, four sets of parallel projection parameters (Parameters 1 to 4) are simulated, as listed in Table 4.2. Scenes are generated based on object space points (Surface I and II) and parallel projection parameters (Parameters 1 to 4) using Equations 4.4. Table 4.3 lists the configuration of the experiments. It is important to mention that scene parallel projection parameters are chosen in such a way that Parameters 1 and 2 result in stereopair in general position and orientation, while Parameters 1 and 3 form two scenes along the same parallel projection direction (same L and M). Finally, Parameters 1 and 4 result in a stereopair sharing a common plane (same ω and φ).

Table 4.1: Simulated surfaces used in the experiments

Surface	Surface I	Surface II
Number of points	500	500
Minimum X (m)	-5500.0	-5500.0
Maximum X (m)	5500.0	5500.0
Minimum Y (m)	-5500.0	-5500.0
Maximum Y (m)	5500.0	5500.0
Trend direction (main slope) in X direction (%)	0.0	0.0
Trend direction (main slope) in Y direction (%)	0.0	0.0
Height variation	yes	no
Wave Amplitude (m)	100.0	-
Wave length in X direction (m)	5000.0	-
Wave length in Y direction (m)	5000.0	-

Table 4.2: Simulated parallel projection parameters used in the experiments

	Parameters 1	Parameters 2	Parameters 3	Parameters 4
L	-0.2	0.1	-0.2	0.1
M	-0.1	0.2	-0.1	0.2
ω°	5.0	-10.0	-10.0	5.0
φ°	3.0	-20.0	-20.0	3.0
κ°	-5.0	5.0	5.0	5.0
Δx (m)	0.0	0.01	0.01	0.01
Δy (m)	0.0	-0.01	-0.01	-0.01
s	2.0E-5	2.0E-5	2.0E-5	2.0E-5

Table 4.3: Surface and parameter configurations of the experiments

Experiment	Involved surface	Involved parallel projection parameters for the first scene	Involved parallel projection parameters for the second scene
Exp. 4.1	Surface I	Parameters 1	-
Exp. 4.2	Surface II	Parameters 1	-
Exp. 4.3	Surface I	Parameters 1	Parameters 2
Exp. 4.4	Surface II	Parameters 1	Parameters 2
Exp. 4.5	Surface I	Parameters 1	Parameters 3
Exp. 4.6	Surface II	Parameters 1	Parameters 3
Exp. 4.7	Surface I	Parameters 1	Parameters 4
Exp. 4.8	Surface II	Parameters 1	Parameters 4

Figure 4.12 shows the configuration of the object surface and the scene footprint of Experiments 4.1 and 4.2. The corresponding scenes are shown in Figure 4.13. Ten relatively well-distributed GCP are selected in each experiment, seen as triangular symbols in the figures, to compute the 2-D Affine parameters (Equations 4.10). Table 4.4 summarizes the results of the least-squares adjustment. As shown in this table, the normal equation matrix, as in the case of Experiment 4.1, is not singular, and has a rank of eight. Therefore, the eight 2-D Affine parameters (A_1 to A_8), are estimated based on the 10 GCP, (redundancy of 12). The variance components and the estimated parameters are listed in Table 4.4. In addition, the residuals at the GCP are not significantly different from zero. Note that no noise was introduced into the scene coordinates. Applying the transformation of the estimated 2-D Affine parameters, as indicated in Section 4.4.4, the derived scene parallel projection parameters, in Table 4.4, are exactly the same as the original values used in the simulation, as shown in Table 4.2.

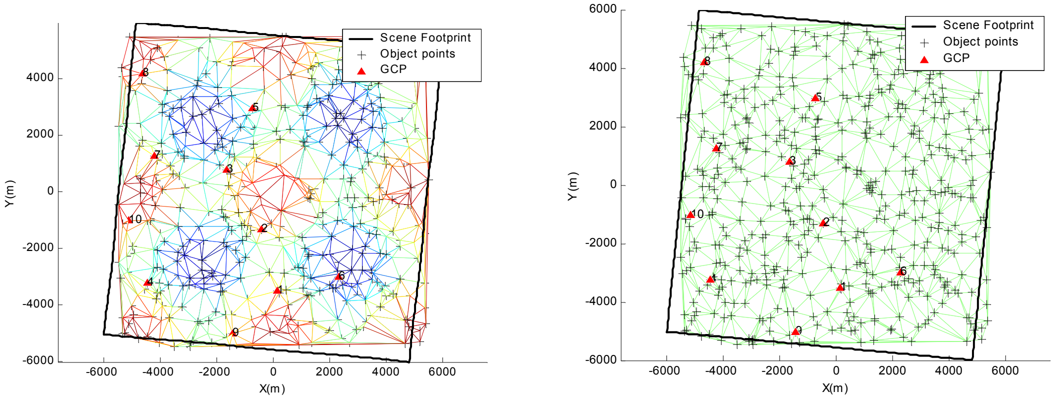

(a) (b)

Figure 4.12: Configuration of Experiments 4.1 (a), and 4.2 (b), as 2-D views of the object space footprint, including GCP, and the footprint of the scenes

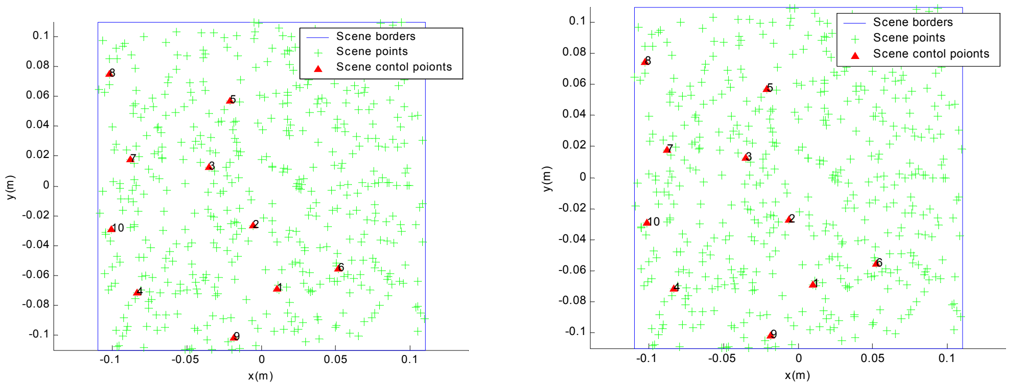

(a) (b)

Figure 4.13: Recorded scenes of Experiments 4.1 (a), 4.2 (b), including the GCP in the scene space

Table 4.4: Results of Experiments 4.1 and 4.2

Experiment number		Exp. 4.1	Exp. 4.2
Rank of normal equations matrix (of Equations 4.10)		8	6
Mathematical model		2-D Affine	Standard Affine
Estimated 2-DAffine/ Standard Affine parameters	σ_0	8.25E-16	6.43E-16
	A_1	2.02E-05	2.02E-05
	A_2	-2.09E-06	-2.09E-06
	A_3	3.92E-06	0
	A_4	1.39E-17	6.94E-17
	A_5	1.78E-06	1.78E-06
	A_6	1.98E-05	1.98E-05
	A_7	2.40E-06	0
	A_8	-6.25E-17	2.22E-16
Derived Scene parallel projection parameters	L	-0.2	-
	M	-0.1	-
	ω°	5	-
	φ°	3	-
	κ°	-5	-
	Δx (m)	0	0
	Δy (m)	0	0
	s	2.0E-5	2.0E-5

On the other hand, the normal equation matrix has been found to be singular, as in the case of Experiment 4.2, because the object space is planar. Therefore, in these experiments, the relationship between the object and scene points is no longer 2-D Affine. Instead, it is standard Affine. Therefore, the A_3 and A_7 parameters are fixed (set to 0) and the least-squares adjustment is repeated. Standard Affine parameters are estimated, as listed in Table 4.4 together with the variance component. It is important to notice that the transformation procedure outlined in Section 4.4.4 cannot be used to obtain the scene parallel orientation parameters since eight independent parameters cannot be obtained from only six parameters. Only Δx, Δy and s can be computed, as listed in the Table 4.4.

To proceed with testing the mathematical models relating two scenes, scenes of Experiments 4.3 to 4.8 are simulated using the parameters listed in Table 4.3. Configurations of these experiments are shown in Figure 4.14 and the recorded scenes in Figures 4.15 and 4.16. Ten points are selected, shown in red circles, to test the mathematical models. It is important to note that Equations 4.41 contain Z values together with the scene coordinates of the points. Therefore, these points have to be vertical GCP. Based on these points, parameters B_1 to B_8, in Equations 4.41 are estimated in a least-squares adjustment. The results are listed in Table 4.5. In experiments 4.3, 4.5 and 4.7, the normal equation matrix is non-singular. Therefore, the parameters can be estimated based on the 10 points, ensuring a redundancy of 12. On the other hand, the normal equation matrix in Experiments 4.4, 4.6 and 4.8 is singular because the object surface is planar. By fixing B_3 and B_7 – that is, setting them to zero - the other parameters can be estimated, comprising a standard Affine transformation. One should note that correspondence is a function of the height, in the case of non-planar object space. On the other hand, if the object space is planar, correspondence can be obtained without knowing the height of the points, as the mathematical relationship between conjugate points reduces to a case of the standard Affine transformation.

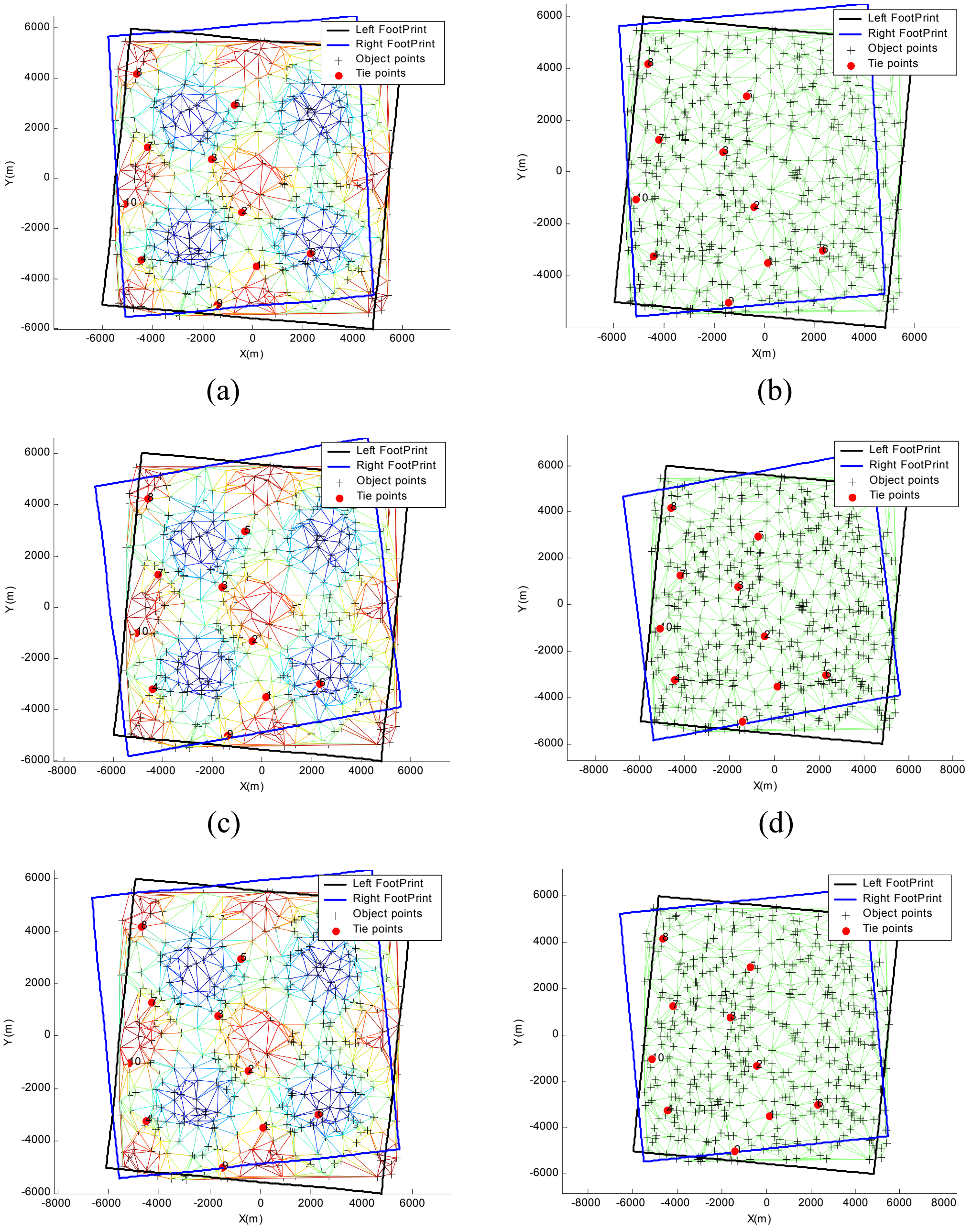

(a) (b)

(c) (d)

(e) (f)

Figure 4.14: Footprint of Experiments 4.3 (a), 4.4 (b), 4.5 (c), 4.6 (d), 4.7 (e) and 4.8 (f), as 2-D views of the object space footprint, including vertical GCP in red circles, and footprint of the scenes

First scene Second scene

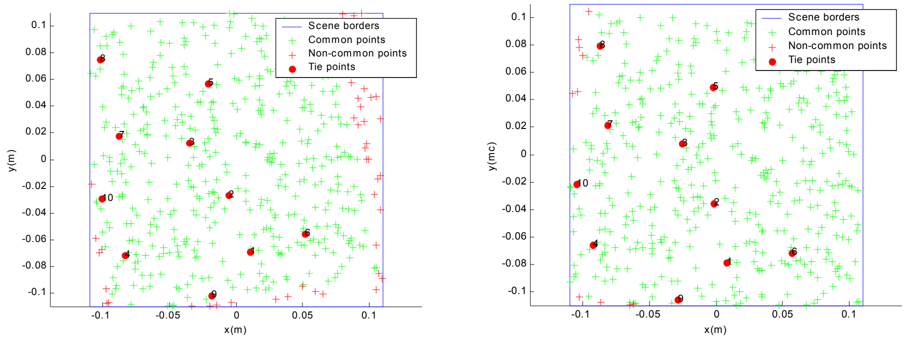

Experiment 4.3

(a) (b)

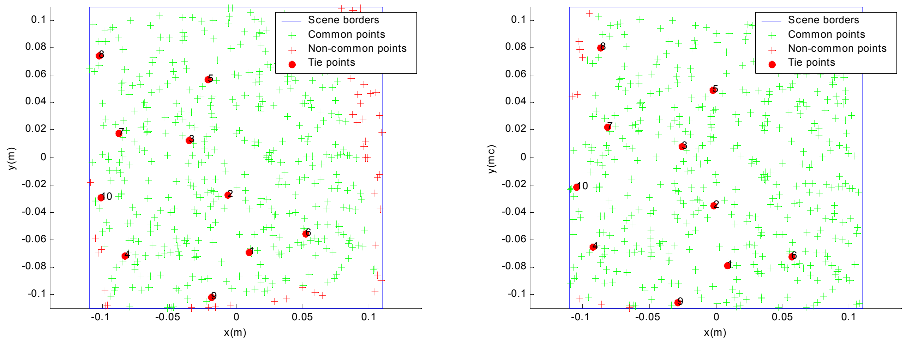

Experiment 4.4

(c) (d)

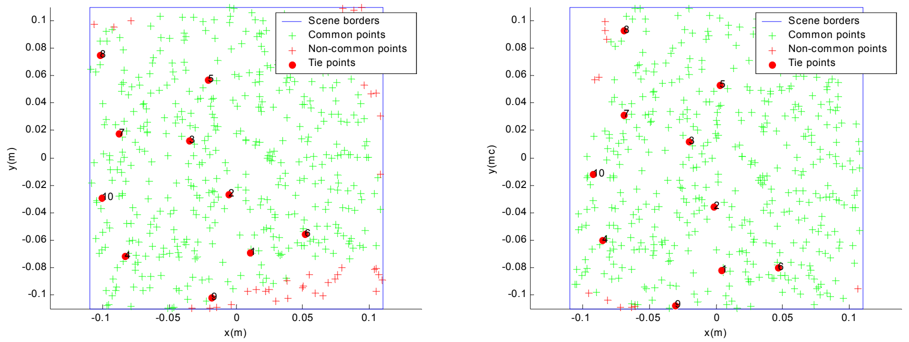

Experiment 4.5

(e) (f)

Figure 4.15: Recorded scenes of Experiments 4.3 to 4.5, including the tie points used in parameter estimation

First scene Second scene

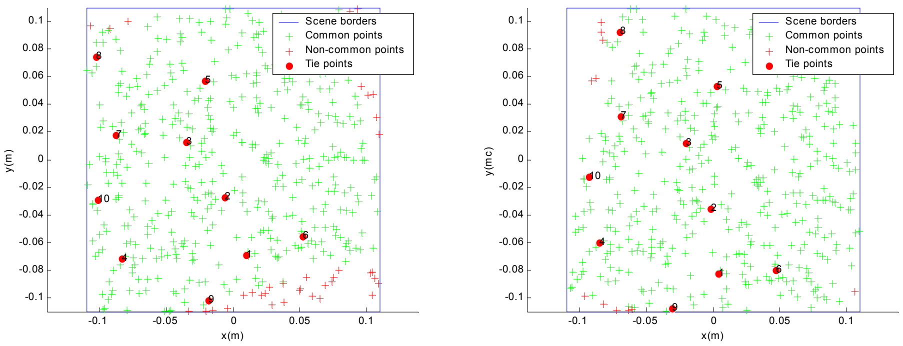

Experiment 4.6

(g) (h)

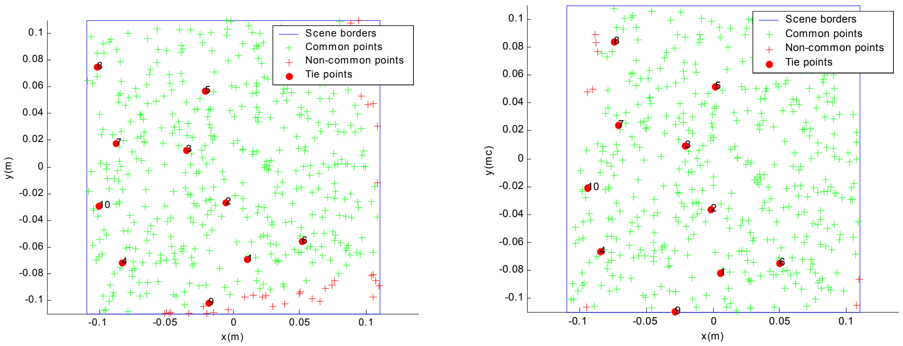

Experiment 4.7

(i) (j)

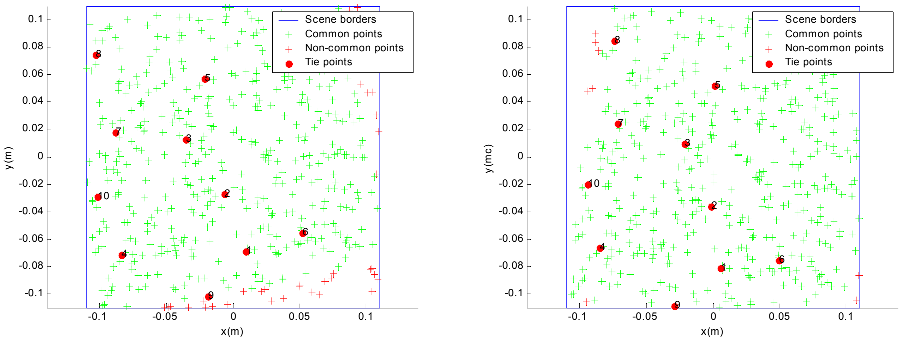

Experiment 4.8

(k) (l)

Figure 4.16: Recorded scenes of Experiments 4.6 to 4.8, including the tie points used in parameter estimation

Table 4.5: Results of implementing Equations 4.41 in Experiments 4.3 to 4.8

Experiment number		Exp. 4.3	Exp. 4.4	Exp. 4.5	Exp. 4.6	Exp. 4.7	Exp. 4.8
Rank of normal equations matrix (Equations 4.41)		8	6	8	6	8	6
Mathematical model		Equations 4.41	Standard Affine	Equations 4.41	Standard Affine	Equations 4.41	Standard Affine
Estimated B_i parameters (Eq. 4.41)/ Standard Affine parameters	σ_0	1.24E-15	8.47E-16	9.12E-16	8.51E-16	9.94E-16	7.66E-16
	B_1	1.07632	1.07632	0.947645	0.947645	0.964854	0.964854
	B_2	0.180713	0.180713	0.227643	0.227643	0.201225	0.201225
	B_3	-7.19E-06	0	-4.07E-19	0	-6.70E-06	0
	B_4	0.01	0.01	0.01	0.01	0.01	0.01
	B_5	-0.17072	-0.17072	-0.26902	-0.26902	-0.19042	-0.19042
	B_6	0.970039	0.970039	1.00589	1.00589	1.00798	1.00798
	B_7	-5.49E-06	0	-1.56E-18	0	-5.63E-06	0
	B_8	-0.01	-0.01	-0.01	-0.01	-0.01	-0.01

In Experiments 4.3 to 4.8, the parameters of Equation 4.42, which describe the epipolar line in one scene for a given point in the other scene, are estimated based on ten relatively well-distributed GCP. These points result in ten equations containing four unknowns (C_1 to C_4), ensuring a redundancy of six. The estimated parameters and the corresponding variance components are listed in Table 4.6. This model is not valid for all cases of object space and for all cases of scene parallel projection parameters used in the experiments. In Experiments 4.4, 4.6 and 4.8, the two scenes were related through planar object space and, therefore, related through a standard Affine transformation. In addition, the two scenes in Experiment 4.5 - although the object space is non-planar - are also related through a standard Affine transformation as they have the same projection vector. Therefore, only in the case of non-planar object space and scenes in general orientation (as in Experiment 4.3) or scenes belonging to the same plane (as in Experiment 4.7) can the model of Equation 4.42 be used.

Table 4.6: Results of implementing Equations 4.42 in Experiments 4.3 to 4.8

Experiment number		Exp. 4.3	Exp. 4.4	Exp. 4.5	Exp. 4.6	Exp. 4.7	Exp. 4.8
Rank of normal equations matrix (Equations 4.42)		4	3	3	3	4	3
Estimated C_i parameters (Eq. 4.42)	σ_0	8.68E-14	-	-	-	1.98E-13	-
	C_1	0.763987	-	-	-	0.840365	-
	C_2	-0.99301	-	-	-	-1.00125	-
	C_3	0.831977	-	-	-	0.83888	-
	C_4	-0.01764	-	-	-	-0.0184	-

The inability to derive the parameters describing the epipolar line for Experiments 4.4, 4.5, 4.6 and 4.8 is attributed to the fact that the relationship between conjugate points can be expressed by a standard Affine transformation. In other words, the epipolar lines reduce to single points since the conjugate point can be identified; that is, the locus of conjugate points is 0-D.

Parameters C_1 to C_4, in Equation 4.42, relate the coordinates of the scenes studied. Therefore, in order to generate normalized scenes, where no y-parallax exists, these parameters should be analyzed and utilized, as will be discussed in Chapter 6. Moreover, it is important to remember that all of the mathematical models and transformations, which were derived in this chapter, are based on parallel projection. However, real scenes are generated according to the rigorous perspective model. Therefore, perspective-to-parallel transformation is the subject of the next chapter.

4.7 SUMMARY

In this chapter, parallel projection has been introduced in terms of its motivations, assumptions and underlying concept. The mathematical model for parallel projection and the associated parameters were derived through a non-linear model using scene parallel projection parameters and a linear model using 2-D Affine parameters. The mathematical relationship between these two sets of parameters was derived and verified. The suitability of these models can be summarized as follows:

- The linear model is suitable in the cases where GCP are available. The GCP are used to directly estimate the 2-D Affine parameters.
- The non-linear model is suitable in the cases where scanner navigation data are available. The scene parallel projection parameters can be derived based on the navigation data, as what will be discussed in Section 5.4, Chapter 5.

The mathematical relationship between two scenes, in general positions/orientations as well as in special cases, generated according to parallel projection, was also derived. The equation of the epipolar line in scenes generated according to parallel projection was derived and its character confirmed as a straight line. It was concluded that, for flat terrain, epipolar lines reduce to points and the mathematical relationship between the associated scenes is a standard Affine transformation.

After discussing the epipolar geometry of scenes generated according to parallel projection, Chapter 5 deals with the necessary transformation of scenes generated according to perspective geometry to comply with the parallel projection model.

CHAPTER 5: PERSPECTIVE TO PARALLEL PROJECTION

5.1 INTRODUCTION

The mathematical model associated with scenes captured according to parallel projection has been discussed in great detail in Chapter 4. The geometry of epipolar lines in these scenes has been discussed, and it has been established that the perspective geometry associated with high altitude imaging systems with narrow AFOV is very similar to parallel projection geometry. However, the captured scenes from such sensors have to be modified to become closer to parallel projection.

In this chapter, the means to transform scenes from perspective-to-parallel projection is established. First, scale modification along the scanning direction is presented in Section 5.2, which entails altering the scene coordinates to compensate for the transformation from perspective to parallel projection. The effect of non-planar object space on the quality of such a transformation is also discussed. Section 5.3 deals with the possible ways of obtaining the roll angles that are required for perspective-to-parallel transformation. To address cases where scanner navigation data (scanner EOP) are available, deriving scene parallel projection parameters is discussed in Section 5.4. Finally, experimental results are presented in Section 5.5.

5.2 SCALE MODIFICATION ALONG THE SCAN LINE

As discussed in Chapter 4, scale is uniform throughout scenes captured according to parallel projection. However, scale may be non-uniform in perspective projection. As discussed in Chapter 3, there exist three imaging configurations for stereo coverage: by changing the pitch angle along the flying direction (similar to that of IKONOS); changing the roll angle across the flying direction (similar to that of SPOT); or by using three-line scanners (similar to that of MOMS and ADS40). For these types, scale modification along the scanning direction, in order to achieve uniform scale along the scan line, is discussed in Sections 5.2.1, 5.2.2, and 5.2.3.

5.2.1 Scale Modification for Scenes Whose Stereo Coverage is Achieved by changing the Pitch Angle Along the Track

Figure 5.1 depicts a scan line oriented with a pitch angle, η, along the flying direction. It shows the footprint as it is defined by the intersection of the plane through the perspective center and the scan line with the object space. The scale of any point can be defined by dividing the image vector with the object vector. Considering a point in the object space along the optical axis, the length of the image vector is c and the length of the object vector is $H/\cos(\eta)$, where H is the flying height above the average elevation. Therefore, its scale, s, can be expressed as:

$$s = \frac{c}{H/\cos(\eta)} \tag{5.1}$$

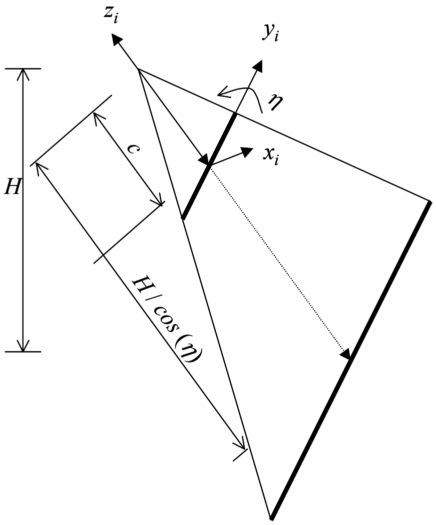

Figure 5.1: Scale uniformity along the scan line for scenes whose stereo coverage is achieved by changing the pitch angle, η, along the track

If the footprint is parallel to the scan line, this scale value is constant for all points along the scan line. Therefore, for such imaging configuration and horizontal flat terrain, uniform scale exists for all points along the scan line, and consequently no scale modification is required. A zero roll angle across the flight direction is assumed.

5.2.2 Scale Modification for Three-Line Scanner Scenes

A three-line scanner is shown in Figure 5.2. Scale can be computed by dividing the length of the image vector by that of the corresponding object vector. Therefore, for the nadir-looking scanner, the scale along the optical axis, s, can be computed as:

$$s = \frac{c}{H} \tag{5.2}$$

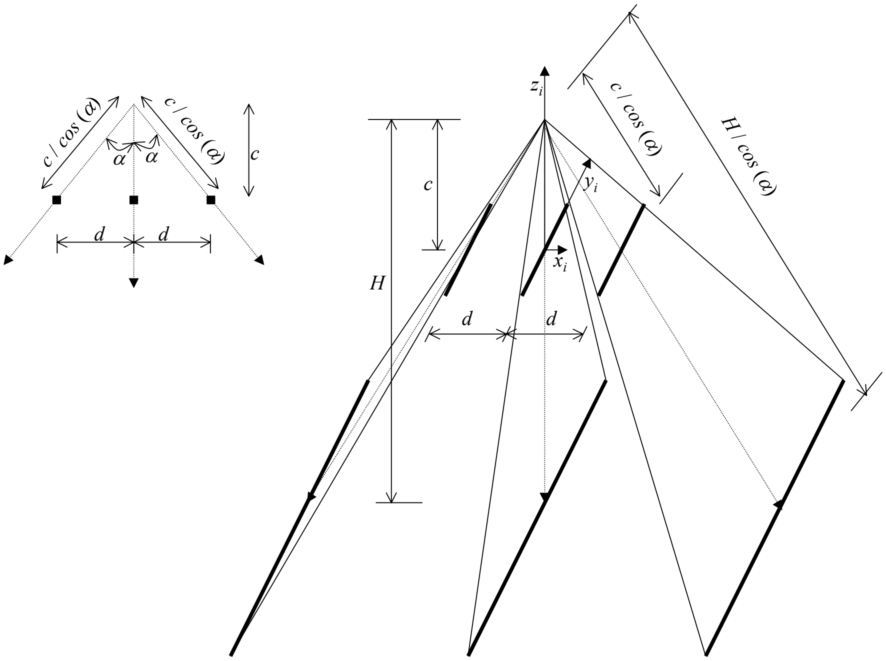

Figure 5.2: Scale uniformity along the scan lines of three-line scanners

For forward- and backward-looking scanners, scale can be computed by dividing the length of the image vector (c / cos α) by the length of the object vector (H / cos α), which results in the same scale value as that computed in Equation 5.2.

Similar to the discussion in Section 5.2.1, assuming zero roll angle across the flight direction and flat horizontal terrain, scale is uniform along each scan line (that is, nadir, forward-, and backward-looking scanners), and consequently no scale modification is required.

5.2.3 Scale Modification for Scenes Whose Stereo Coverage is Achieved Across-Track using Roll Angles

Tilting the scanner across the track using roll angle results in non-uniform scale along the scanning direction. Scale modification of coordinates, generated according to perspective geometry, to comply with parallel projection, has been established (Okamoto et al., 1992; Okamoto et al., 1996; Okamoto and Fraser, 1998; Ono et al., 1999; Hattori et al., 2000; Ono et al., 2000). Such a transformation will be discussed together with the underlying assumptions in this section.

Figure 5.3 shows the case of a 1-D scanner, represented by b_1d_1 and the corresponding perspective center O. Therefore, AFOV can be computed as:

$$\mathrm{AFOV} = 2\arctan\left(\frac{a_1b_1}{c}\right) = 2\arctan\left(\frac{a_1d_1}{c}\right) \tag{5.3}$$

where:

a_1 is the intersection of the optical axis with the scan line; and

c is the principal distance of the sensor involved.

Assuming an average elevation (H) as shown in Figure 5.3, points a_1, b_1, and d_1, which are mapped through perspective projection, represent points A, B, and D, respectively in the object space. If the optical axis is chosen to represent the parallel projection direction, then the object space points A, B, and D will be mapped as points a_2, b_2, and d_2, respectively, before applying a scale. For purposes of illustration, the same object points are also projected onto plane E, which is parallel to the image plane and passing through point A. The object points will be mapped into plane E as points A_1, B_1, and D_1 through perspective projection and as points A_2, B_2, and D_2 through parallel projection.

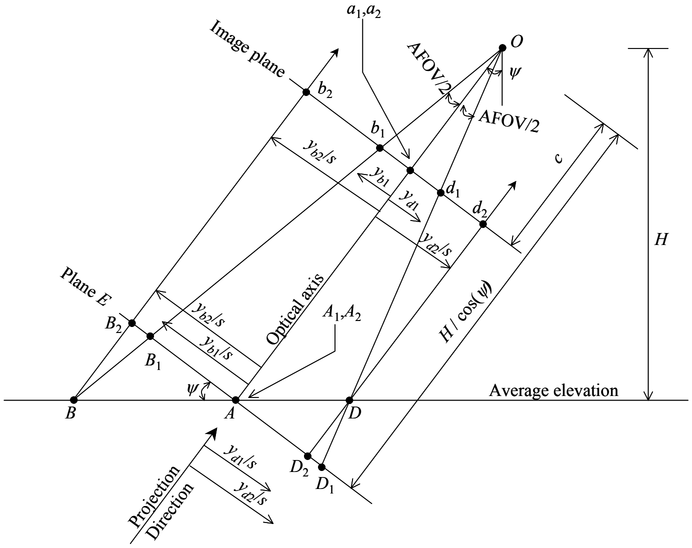

Figure 5.3: Scale non-uniformity along the scan line for SPOT scenes

Points a_1 and a_2 are identical because they belong to the optical axis, which is chosen as the parallel projection direction. Similarly, A_1 and A_2 are identical. Distances A_1B_1 and a_1b_1, which are mapped in a perspective projection, are related through the scale of point A (Equation 5.4). Similarly, distances A_1D_1 and a_1d_1, are related through the same scale, which is the scale between the plane E and the image.

$$s = \frac{c}{H/\cos(\psi)} = \frac{a_1 b_1}{A_1 B_1} = \frac{a_1 d_1}{A_1 D_1} \tag{5.4}$$

where:

s is the scale of point A; and

ψ is the scanner roll angle.

It is preferred to have similar scales for the perspective and parallel projections. Thus, plane E is chosen to compare the coordinates of the two projections. Any point P in the object space within the AFOV is mapped into plane E as points P_1 and P_2 in perspective and parallel projections, respectively (see Figure 5.4).

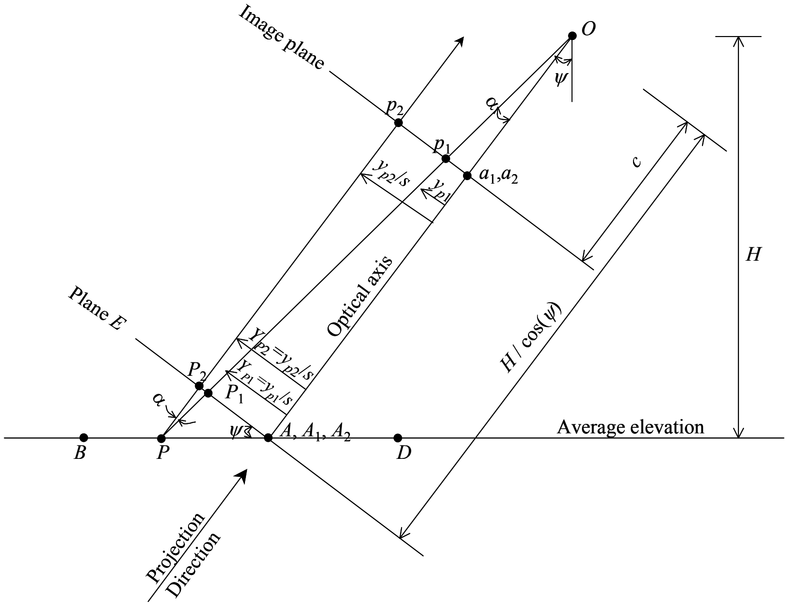

Figure 5.4: Perspective to parallel transformation of point P in a SPOT scene

In Figure 5.4, light ray OP makes an angle α with the optical axis. As the ray Pp_2 is parallel to the optical axis, the angle P_1PP_2 equals α. The tangent of angle α can be derived from the two triangles P_1PP_2 and OA_1P_1 as:

$$\tan(\alpha)=\frac{Y_{P2}-Y_{P1}}{PP_2}=\frac{Y_{P1}}{H/\cos(\psi)} \tag{5.5}$$

Moreover, the tangent of the roll angle, ψ, can be derived from triangle A_1PP_2 as:

$$\tan(\psi)=\frac{PP_2}{Y_{P2}} \tag{5.6}$$

Combining Equations 5.5 and 5.6 results in:

$$\frac{Y_{P2}-Y_{P1}}{Y_{P2}\tan(\psi)}=\frac{Y_{P1}}{H/\cos(\psi)}$$

Rearranging, the above equation can be rewritten as:

$$Y_{P2}=Y_{P1}\frac{H}{H-Y_{P1}\sin(\psi)}$$

It is important to remember that Y_{p1} and Y_{p2} are the coordinates of the perspective and parallel projections, respectively, on plane *E*. Y_{p1} must be scaled down to the image plane using the scale factor *s* (Equation 5.4). It is preferred to have similar scales for parallel and perspective projections. Therefore, *s* is chosen for scaling down the parallel projection points. Substituting for Y_{p2} by y_{p2}/s and for Y_{p1} by y_{p1}/s results in:

$$\frac{y_{P2}}{s}=\frac{y_{P1}}{s}\frac{H}{H-\frac{y_{P1}}{s}\sin(\psi)}$$

Where y_{p1} and y_{p2} are the coordinates of the perspective and parallel projections, respectively, in the image plane. Rearranging, the above equation can be written as:

$$y_{P2}=y_{P1}\frac{H}{H-\frac{y_{P1}}{s}\sin(\psi)}$$

Substituting for *H* from Equation 5.4 results in:

$$y_{P2}=y_{P1}\frac{\frac{c.\cos(\psi)}{s}}{\frac{c.\cos(\psi)}{s}-\frac{y_{P1}}{s}\sin(\psi)}$$

Rearranging, the above equation can be rewritten as:

$$y_{P2} = y_{P1} \frac{1}{1 - \frac{y_{P1}}{c} \tan(\psi)} \tag{5.7}$$

Equation 5.7 represents the transformation from perspective to the parallel projection along the scan line (Okamoto et al., 1992; Okamoto et al., 1996; Okamoto and Fraser, 1998; Ono et al., 1999; Hattori et al., 2000; Ono et al., 2000). It is important to note that the scale s, which depends on the average elevation, is not required for a transformation such as this. It must also be mentioned that this equation is valid for other stereo coverage methods such as IKONOS or three-line scanners, if the roll angle, ψ, which may differ from zero, is available. Therefore, Equation 5.7 is a general formula describing the perspective-to-parallel transformation for linear array scanner scenes. This equation assumes a knowledge of the roll angle, which can be available directly from scanner orientation angles (as will be discussed in Section 5.3.1). On the other hand, in cases where it is not available, GCP can be used to indirectly estimate the roll angle (as will be discussed in Section 5.3.2). However, let us first discuss some of the assumptions that were made during the derivation of Equation 5.7.

One of the main assumptions in the previous derivation is having flat horizontal terrain. Therefore, it is important to quantify the introduced error due to possible deviation from this assumption. Figure 5.5 shows point P that has a perspective projection of P_1 on plane E, and which is below the average elevation by a distance ΔZ. If point P is assumed to have an elevation similar to the average elevation, then the parallel projected point will be P_2 on plane E. However, the true parallel projection point is P_3. Therefore, an error of P_2P_3 (or ΔY_{23}) has been introduced. An error such as this may be expressed as a function of ΔZ in the following derivation.

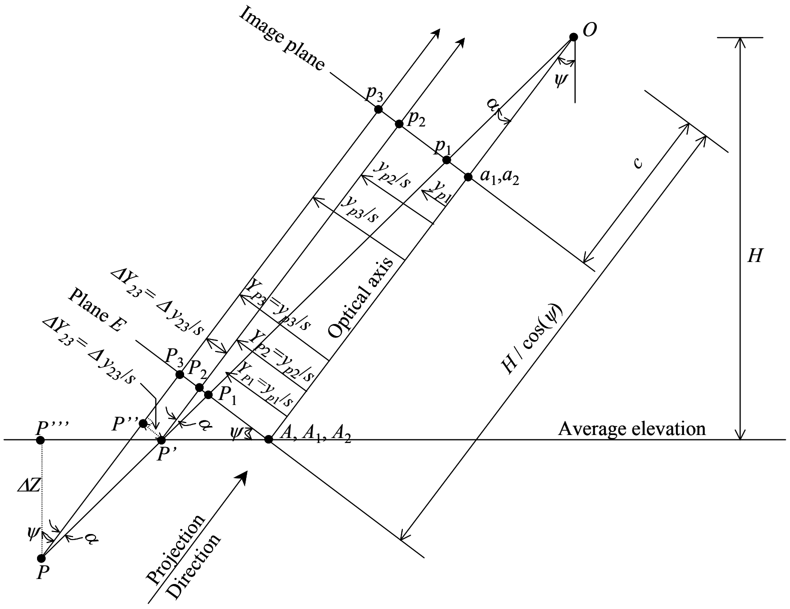

Figure 5.5: Effect of non-flatness of terrain on the perspective to parallel transformation for SPOT scene

The length *PP'* can be expressed in triangles *PP'P''* and *PP'P'''* as:

$$PP' = \frac{\Delta Y_{23}}{\sin(\alpha)} = \frac{\Delta Z}{\cos(\psi + \alpha)}$$

Therefore:

$$\Delta Y_{23} = \Delta Z \frac{\sin(\alpha)}{\cos(\psi + \alpha)}$$

Substituting for ΔY_{23} by $\Delta y_{23}/s$ results in:

$$\Delta y_{23} = s.\Delta Z \frac{\sin(\alpha)}{\cos(\psi + \alpha)} \tag{5.8}$$

Equation 5.8 expresses the introduced error by assuming an average elevation instead of the true elevation while transforming from perspective to parallel projection. The derived formula, Equation 5.8, is similar to that derived by Ono et al. (1999). For SPOT scenes, $\psi = 26°$, $c = 1.082$m, and $H = 822$km; therefore, $s = 1.18e\text{-}6$, from Equation 5.4. For a point at the end of the scan line, $\alpha = 1.9°$, an elevation error of $\Delta Z = 113$m introduces error Δy_{23} of 5.0 μm. For IKONOS and three-line scanners, Equation 5.8 reduces to:

$$\Delta y_{23} = s.\Delta Z \tan(\alpha) \tag{5.9}$$

For IKONOS scenes, $\eta = 22.5°$, $c = 10$m, and $H = 680$km; then $s = 1.35e\text{-}5$, from Equation 5.1. For a point at the end of the scan line, $\alpha = 0.46°$, an elevation error of $\Delta Z = 46$m introduces error Δy_{23} having a magnitude of 5.0 μm.

5.3 DERIVING THE ROLL ANGLE

A knowledge of the roll angle is required to perform a perspective-to-parallel correction, as expressed in Equation 5.7. Two alternatives can be used, depending on the availability of data. Knowing the scanner rotation angles, the roll angle can be derived directly (Section 5.3.1). On the other hand, if GCP are available, they can be used to indirectly estimate the roll angle, as discussed in Section 5.3.2.

5.3.1 Deriving the Roll Angle Directly using the Scanner Rotation Angles

The roll angle can be determined if the scanner rotation angles are available. Similar to Equation A.35, Appendix A, vector $\mathbf{y}_i$, (unit vectors along the scanner direction with respect to the object coordinate system) can be expressed as (see Figure 5.6):

$$\mathbf{y}_i = \begin{bmatrix} r_{i12} \\ r_{i22} \\ r_{i32} \end{bmatrix} \tag{5.10}$$

which is the second column of the rotation matrix associated with the i^{th} scan line.

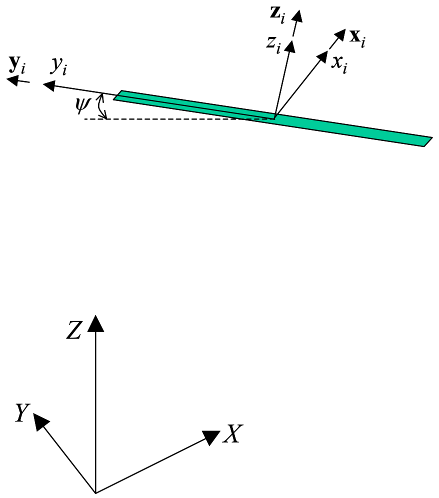

Figure 5.6: Unit vectors $\mathbf{x}_i$, $\mathbf{y}_i$ and $\mathbf{z}_i$, along the scanner axes x_i, y_i and z_i, respectively. Roll angle, ψ, as the vertical angle of vector $\mathbf{y}_i$ with respect to the ground coordinate system

The roll angle may be defined as inclination of the vector $\mathbf{y}_i$, Figure 5.6, to the horizontal plane. As vector $\mathbf{y}_i$ has unit length, its components, r_{i12}, r_{i22}, and r_{i32} represent the directional cosines with respect to the X-, Y- and Z- axes, respectively. Therefore, The roll angle ψ can be computed as:

$$\psi = \frac{\pi}{2} - \arccos(r_{i32}) \tag{5.11}$$

Substituting r_{i32} with its explicit value based on the scanner orientation angles, ω_i, φ_i, κ_i:

$$\psi = \frac{\pi}{2} - \arccos[\sin(\omega_i)\cos(\kappa_i) + \cos(\omega_i)\sin(\varphi_i)\sin(\kappa_i)] \tag{5.12}$$

From Equation 5.12, it becomes clear that the roll angle is different from the scanner orientation angle ω_i. The rotation angles and the associated rotation matrix adopted in this dissertation are described in Appendix A, Equations A.3.

5.3.2 Indirect Estimation of the Roll Angle using GCP

In Equation 5.7, y_{p2} represents the y-coordinate according to parallel projection, which is identical to y in Equations 4.10. Equating these coordinates yields:

$$\frac{y_{P1}}{1-\frac{y_{P1}}{C}\tan(\psi)} = A_5X + A_6Y + A_7Z + A_8$$

Rearranging gives the following:

$$y_{P1} = \frac{A_5X + A_6Y + A_7Z + A_8}{1+\frac{\tan(\psi)}{C}\left(A_5X + A_6Y + A_7Z + A_8\right)} \tag{5.13}$$

Observe that y_{p1} represents the y-coordinate according to perspective geometry, which can be measured directly from the raw scene. Having at least five GCP, together with the knowledge of the scanner principal distance, the 2-D Affine parameters, A_5 to A_8, together with the roll angle, ψ, can be determined. Having more than 5 GCP, the parameters can be estimated in a least-squares adjustment. Such an adjustment requires linearization of Equation 5.13 using approximate values for the unknown parameters, which can be computed from the linear model (Equations 4.10).

The next Section deals with cases where the scanner navigation data are available. For such cases, scene parallel projection parameters can be derived directly.

5.4 MATHEMATICAL RELATIONSHIP BETWEEN NAVIGATION PARAMETERS (SCANNER EOP) AND PARALLEL PROJECTION PARAMETERS

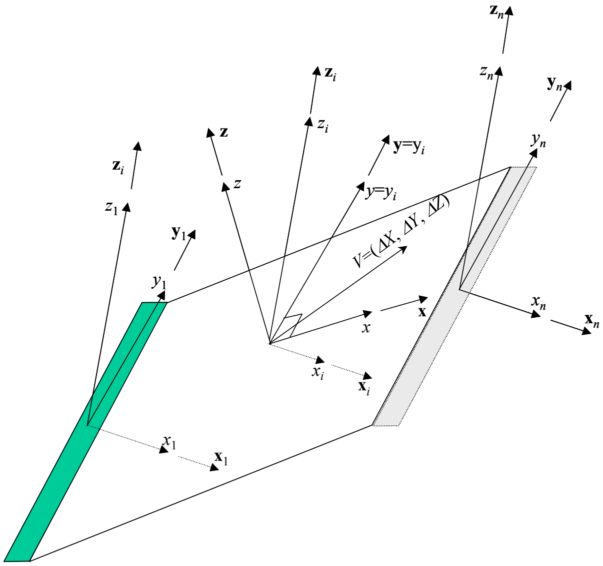

Figure 5.7: Orientation vectors and axes of the line scanner and the scene

In this section, scene parallel projection parameters (L, M, ω, φ, κ, Δx, Δy, s) will be derived using the navigation parameters, which are the parameters expressing the scanner EOP, as described in Equations 3.1. Similar to Equations A.30 and A.24, Appendix A, vectors $\mathbf{x}_i$ and $\mathbf{z}_i$, which are unit vectors along the image coordinate axes with respect to the object coordinate system, (see Figures 5.6 and 5.7) can be expressed as:

$$\mathbf{x}_i = \begin{bmatrix} r_{i11} \\ r_{i21} \\ r_{i31} \end{bmatrix} \tag{5.14}$$

$$\mathbf{z}_i = \begin{bmatrix} r_{i13} \\ r_{i23} \\ r_{i33} \end{bmatrix} \tag{5.15}$$

where r_{i11} to r_{i33} are the elements of the rotation matrix associated with the i^{th} scan line. These vectors, together with the $\mathbf{y}_i$ vector (Equation 5.10) will be utilized in the following subsections to derive the scene parallel projection parameters. Since a scanner moving with constant attitude (Equations 3.1) is assumed, these vectors do not change their values within the scene.

5.4.1 Projection Vector (*L*, *M*, *N*)

Because of the assumption of constant rotation angles for the whole scene, the projection vector will not change from one scan line to the next. The optical axis for scan line number i is expressed as $(-r_{i13}, -r_{i23}, -r_{i33})^T$ pointing downwards, in the opposite direction to $\mathbf{z}_i$. Therefore, the unit projection vector can be expressed as:

$$\begin{bmatrix} L \\ M \\ N \end{bmatrix} = \mathbf{z}_i = \begin{bmatrix} r_{i13} \\ r_{i23} \\ r_{i33} \end{bmatrix} \tag{5.16}$$

5.4.2 Scene Rotation Angles (ω, φ, κ)

It is important to note that x_i-, y_i-, and z_i-axes of the i^{th} scan line (whose orientation vectors are $\mathbf{x}_i$, $\mathbf{y}_i$, and $\mathbf{z}_i$) may differ from the x-, y-, and z-axes of the scene. This can be seen in Figure 5.6 where the velocity vector, V, does not lie within the plane formed by the x_i- and y_i-axes of the scan line. Because scene and scanner coordinate systems might differ from one other, orientation angles of the scene axes (ω, φ, κ) may differ from those associated with the scanner axes (ω_i, φ_i, κ_i). The scene orientation angles (ω, φ, κ) and the corresponding rotation matrix, R, can be derived after defining the scene coordinate system and its relation to the ground coordinate system.

The scene plane can be expressed using the velocity vector, V, and the orientation vector $\mathbf{y}_i$ along the y_i axis. After defining the scene plane, two perpendicular scene axes (x- and y-axes) must be introduced. The y-axis can be chosen to be the same as the direction of y_i-axis, as shown in Figure 5.7. The following procedure can be used to determine the unit vectors ($\mathbf{x}$, $\mathbf{y}$, $\mathbf{z}$) along scene axes:

- Determine vector **z**, which is the normal to the scene plane, as the normalized cross product between the two vectors V and $\mathbf{y}_i$ as:

$$\mathbf{z} = \frac{V \times \mathbf{y}_i}{\left|V \times \mathbf{y}_i\right|} = \frac{1}{\sqrt{\left(r_{i32}\Delta Y - r_{i22}\Delta Z\right)^2 + \left(r_{i12}\Delta Z - r_{i32}\Delta X\right)^2 + \left(r_{i22}\Delta X - r_{i12}\Delta Y\right)^2}} \begin{bmatrix} r_{i32}\Delta Y - r_{i22}\Delta Z \\ r_{i12}\Delta Z - r_{i32}\Delta X \\ r_{i22}\Delta X - r_{i12}\Delta Y \end{bmatrix} \tag{5.17}$$

- Determine vector **x** as the normalized cross product of vectors **y** and **z**. Since **y** and **z** are unit and orthogonal vectors, vector **x** can be written as:

$$\mathbf{x} = \frac{\mathbf{y} \times \mathbf{z}}{\left|\mathbf{y} \times \mathbf{z}\right|} = \frac{\mathbf{y} \times \mathbf{z}}{\left|\mathbf{y}\right|.\left|\mathbf{z}\right| \sin\left(\pi / 2\right)} = \mathbf{y} \times \mathbf{z}$$

$$\mathbf{x} = \frac{1}{\sqrt{\left(r_{i32}\Delta Y - r_{i22}\Delta Z\right)^2 + \left(r_{i12}\Delta Z - r_{i32}\Delta X\right)^2 + \left(r_{i22}\Delta X - r_{i12}\Delta Y\right)^2}} . \begin{bmatrix} r_{i22}^2\Delta X + r_{i32}^2\Delta X - r_{i12}r_{i22}\Delta Y - r_{i12}r_{i32}\Delta Z \\ r_{i12}^2\Delta Y + r_{i32}^2\Delta Y - r_{i12}r_{i22}\Delta X - r_{i22}r_{i32}\Delta Z \\ r_{i12}^2\Delta Z + r_{i22}^2\Delta Z - r_{i12}r_{i32}\Delta X - r_{i22}r_{i32}\Delta Y \end{bmatrix} \tag{5.18}$$

Thus, the rotation matrix, R, between the object and scene coordinate systems can be written as:

$$R = \begin{bmatrix} \mathbf{x} & \mathbf{y} & \mathbf{z} \end{bmatrix} \tag{5.19}$$

5.4.3 Scene Scale (*s*)

Scale along the scanning direction can be computed by intersecting the optical axis with the average elevation surface. The collinearity equations can then be written as:

$$\begin{bmatrix} X - X_0 \\ Y - Y_0 \\ Z_{av} - Z_0 \end{bmatrix} = \frac{1}{s} R_i \begin{bmatrix} 0 \\ 0 \\ -c \end{bmatrix}$$

Therefore, the third equation can be rewritten as:

$$Z_{av} - Z_{0i} = \frac{1}{s} r_{i33} \left(-c \right) \tag{5.20}$$

Rearranging, the scale s can be expressed as:

$$s = r_{i33} \frac{c}{Z_{0i} - Z_{av}} \tag{5.21}$$

where:

Z_{av} is the average elevation;

Z_{0i} is the Z–coordinate of the perspective center of the image number i; and

Z_{0i} - Z_{av} is the flying height above the average elevation, H.

It is important to note that the origin of the scene coordinate system is chosen in the middle of the scene. Therefore, i in Equation 5.21 represents the middle scanned image, i.e., ($i = n/2$), where n is the number of scanned images in the scene. Recall that in the constant-velocity-constant-attitude case (Equations 3.1) the scanner's position, with respect to the object coordinate system, may change from one exposure station to another.

5.4.4 Scene Shifts (Δx, Δy)

Scene shifts can be computed using Equations 4.4, by setting the origin of the scene coordinate system to the origin of the coordinate system of the middle image. This can be achieved by substituting the vector $(X, Y, Z)^T$ with the vector $(X_{0i}, Y_{0i}, Z_{0i})^T$, where i is the middle image, and by setting the scene coordinates x and y to zero. Therefore, Equations 4.4 can be rewritten as:

$$\begin{bmatrix} 0 \\ 0 \\ 0 \end{bmatrix} = s.\lambda.R^T \begin{bmatrix} L \\ M \\ N \end{bmatrix} + s.R^T \begin{bmatrix} X_{0i} \\ Y_{0i} \\ Z_{0i} \end{bmatrix} + \begin{bmatrix} \Delta x \\ \Delta y \\ 0 \end{bmatrix}$$

Expanding, the above equations can be rewritten as:

$$\begin{aligned} 0 &= s.\lambda(r_{11}L + r_{21}M + r_{31}N) + s(r_{11}X_{0i} + r_{21}Y_{0i} + r_{31}Z_{0i}) + \Delta x \\ 0 &= s.\lambda(r_{12}L + r_{22}M + r_{32}N) + s(r_{12}X_{0i} + r_{22}Y_{0i} + r_{32}Z_{0i}) + \Delta y \\ 0 &= s.\lambda(r_{13}L + r_{23}M + r_{33}N) + s(r_{13}X_{0i} + r_{23}Y_{0i} + r_{33}Z_{0i}) + 0 \end{aligned} \tag{5.22}$$

Equations 5.22 contain three unknowns (*Δx*, *Δy*, *λ*). Therefore, *λ* can be computed using the third equation as:

$$\lambda = -\frac{r_{13}X_{0i} + r_{23}Y_{0i} + r_{33}Z_{0i}}{r_{13}L + r_{23}M + r_{33}N}$$

Substituting this value of *λ* into the first and second equations of Equations 5.22 results in:

$$\begin{aligned} \Delta x = {} & s\left(\frac{r_{13}(r_{11}L + r_{21}M + r_{31}N)}{r_{13}L + r_{23}M + r_{33}N} - r_{11} \right) X_{0i} + s\left(\frac{r_{23}(r_{11}L + r_{21}M + r_{31}N)}{r_{13}L + r_{23}M + r_{33}N} - r_{21} \right) Y_{0i} \\ & + s\left(\frac{r_{33}(r_{11}L + r_{21}M + r_{31}N)}{r_{13}L + r_{23}M + r_{33}N} - r_{31} \right) Z_{0i} \\ \Delta y = {} & s\left(\frac{r_{13}(r_{12}L + r_{22}M + r_{32}N)}{r_{13}L + r_{23}M + r_{33}N} - r_{12} \right) X_{0i} + s\left(\frac{r_{23}(r_{12}L + r_{22}M + r_{32}N)}{r_{13}L + r_{23}M + r_{33}N} - r_{22} \right) Y_{0i} \\ & + s\left(\frac{r_{33}(r_{12}L + r_{22}M + r_{32}N)}{r_{13}L + r_{23}M + r_{33}N} r_{32} \right) Z_{0i} \end{aligned} \tag{5.23}$$

which is the final expression for computing the scene shifts (*Δx*, *Δy*).

Next section deals with experimental results to analyze/verify the mathematical transformations and relationships derived in this chapter.

5.5 EXPERIMENTS

In this section, synthetic data are generated according to the rigorous perspective model, where object space points are back-projected into the scene space. The mathematical relationship between the navigation data and scene parallel projection parameters (Section 5.4) are then tested. Scene parallel projection parameters are used to produce 2-D Affine parameters (Section 4.4.2, Chapter 4). In addition, another set of 2-D Affine parameters are indirectly estimated based on GCP. Comparison of the derived parameters is performed in the object space. The perspective-to-parallel transformation (Equation 5.7) is also tested using the directly derived roll angle (see Section 5.3.1) and the indirectly estimated roll angle (see Section 5.3.2).

Object space points are simulated and back-projected into scene stereopair using the rigorous perspective projection model. Scanner IOP and EOP are listed in Table 5.1. It is assumed that the scanner's trajectory and orientation comply with the constant-velocity-constant-attitude EOP model.

Table 5.1: EOP and IOP parameters used for the simulation

Left Scanner Parameters		Right Scanner Parameters	
IOP	EOP	IOP	EOP
Principal point (x_0, y_0) =(0.0, 0.0) m Principal distance c = 10.0 m x = 0.0 m Scene size= 13480 × 13480 pixels Pixel size = 12 μm Scene time = 1.57 sec	Scanner position at time 0 = (X_0 ,Y_0, Z_0) = (-288.3, 59.5, 680.0) km Scanner Velocity = (ΔX, ΔY, ΔZ) = (7.0, 0.0, 0.0) km/s Scanner orientation angles = (ω, φ, κ) =(-5.0°, -22.5°, 0.0°)	Principal point (x_0, y_0) =(0.0, 0.0) m Principal distance c = 10.0 m x = 0.0 m Scene size= 13480 × 13480 pixels Pixel size = 12 μm Scene time = 1.57 sec	Scanner position at time 0 = (X'_0 ,Y'_0, Z'_0) = 277.3, -59.5, 680.0) km Scanner Velocity = ($\Delta X'$, $\Delta Y'$, $\Delta Z'$) = (7.0, 0.0, 0.0) km/s Scanner orientation angles = (ω', φ', κ') =(5.0°, 22.5°, 0.0°)

Twenty-five object space points covering an area of 11km by 11km are simulated with an average elevation of zero and a height variation of ±1000m. This is achieved by randomly selecting Z values with zero mean and a standard deviation of 1000 m. Figure 5.8a shows the distribution of the object points and the footprint of the left and right scenes. Left and right scenes are shown in Figures 5.8b and 5.8c, respectively. Among the object points, sixteen points are used as GCP shown as red triangles in Figure 5.8, while nine points are used as check points shown as green circles in the same figure.

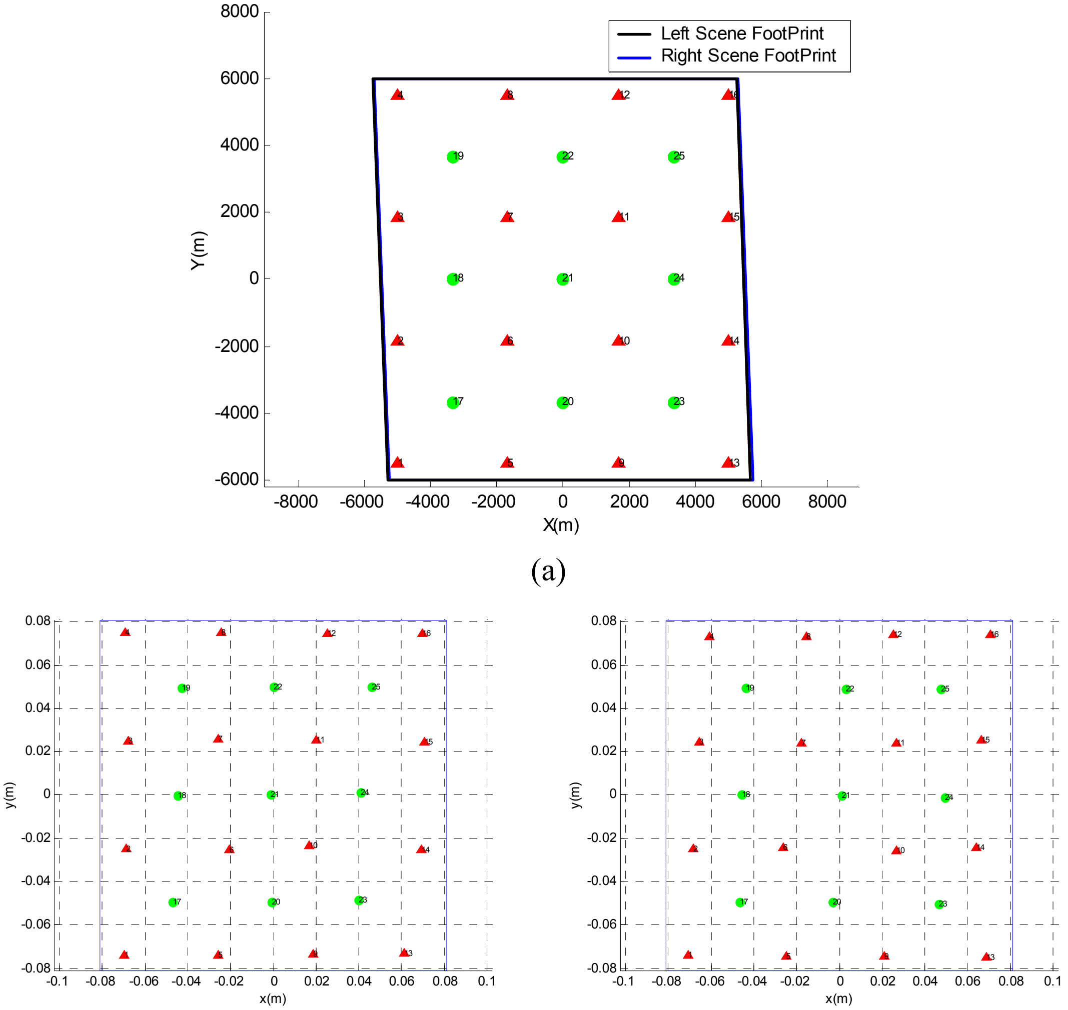

(a)

(b)

(c)

Figure 5.8: Object space points together with scene footprint (a), and the left and right scene points, (b) and (c), respectively

Using scene EOP (navigation data) in addition to IOP and average elevation, scene parallel projection parameters are derived, as explained in Section 5.4 (see Table 5.2). The roll angles, which are also derived based on the scanner orientation (Equation 5.12), are also listed in Table 5.2.

Table 5.2: Derived scene parallel projection parameters and roll angle

		Left Scene	Right Scene
Parallel Projection Parameters	L	-0.38268	0.382683
	M	0.080521	-0.08052
	$\omega°$	-5	5
	$\varphi°$	0	0
	$\kappa°$	0	0
	Δx (m)	0.000326	-0.00033
	Δy (m)	0	0
	s	1.35E-05	1.35E-05
Roll angle, $\psi°$		-5.0	-5

Using the derived scene parallel projection parameters, 2-D Affine parameters are derived, as explained in Section 4.4.2 (see Table 5.3).

Table 5.3: Derived 2-D Affine parameters

		Left Scene	Right Scene
2-D Affine Parameters	A_1	1.353E-05	1.353E-05
	A_2	4.887E-07	4.886E-07
	A_3	5.585E-06	-5.585E-06
	A_4	0.00032598	-0.00032598
	A_5	0	0
	A_6	1.348E-05	1.348E-05
	A_7	-1.180E-06	1.180E-06
	A_8	0	0

Some attention must be given to the quality of the derived 2-D Affine parameters and the roll angles. Space intersection is chosen as a means of examining their quality in the object space. In this case, the 2-D Affine parameters for both left and right scenes, along with left and right scene coordinates, are used. Therefore, for each scene point, two sets of 2-D Affine equations, Equations 4.10, are written. For each pair of tie points, four equations can be written containing 3 unknowns, the object coordinates of the point. Thus, the object coordinates can be solved for, in a least-squares adjustment. The errors can then be computed in the object space between the estimated coordinates and the original coordinates used in the simulation. The mean and standard deviation of the error values are computed, as shown in Table 5.4.

Table 5.4: Mean and standard deviation of the error values of the directly estimated object space points with and without Perspective-To-Parallel (PTP) correction for Experiments 5.1 to 5.3

	Errors, m		
	$Mean_{XY} \pm Std_{XY}$	$Mean_{Z} \pm Std_{Z}$	Mean ± Std
Without PTP	0.582 ± 3.427	0.944 ± 0.853	1.109 ± 3.532
With PTP	0.590 ± 3.466	0.023 ± 0.194	0.591 ± 3.472

In the above experiment, the Perspective-To-Parallel (PTP) transformation is also tested, based on the derived roll angle, as explained in Section 5.2.3. The effect of performing a PTP transformation in terms of reduction of the *Z*-component of the errors can be seen. It can then be concluded that omitting such a correction results in larger errors in the derived height values.

For the same synthetic data, the 2-D Affine parameters are indirectly estimated using GCP (Equations 4.10). Three sets of results were obtained: without PTP correction; with PTP correction using the directly determined roll angle (the true roll angle); and with PTP correction using the estimated roll angle (Equation 5.13). However, the task of solving for the parameters in Equation 5.13 has a stability problem. Therefore, a coordinate normalization is performed prior to the estimation; Tao and Hu (2001) address a similar problem dealing with rational functions. The estimated 2-D Affine Parameters and the estimated roll angles are listed in Table 5.5. Among the 20 object points, 16 points (seen as red triangles in Figure 5.8) are used as GCP in the parameter estimation. The other nine points, shown as green circles, are used as check points.

Table 5.5: Indirectly estimated 2-D Affine parameters and roll angles using GCP

		Left Scene			Right Scene		
		Without PTP	With PTP (true roll angle)	With PTP (estimated roll angle)	Without PTP	With PTP (true roll angle)	With PTP (estimated roll angle)
$\hat{\sigma}_0$, pixels		3.47	2.61	2.60	3.95	2.63	2.58
ψ°		0.00000	-5.00000	-4.63434	0.00000	5.00000	6.09394
2-D Affine Parameters	A_1	1.353E-05	1.353E-05	1.353E-05	1.353E-05	1.353E-05	1.353E-05
	A_2	4.884E-07	4.884E-07	4.884E-07	4.884E-07	4.884E-07	4.884E-07
	A_3	5.583E-06	5.583E-06	5.583E-06	-5.583E-06	-5.583E-06	-5.583E-06
	A_4	0.0003258	0.0003258	0.0003258	-0.0003258	-0.0003258	-0.0003258
	A_5	4.949E-09	4.808E-09	4.818E-09	4.535E-09	4.811E-09	4.872E-09
	A_6	1.348E-05	1.348E-05	1.348E-05	1.348E-05	1.348E-05	1.348E-05
	A_7	-1.195E-06	-1.185E-06	-1.186E-06	1.184E-06	1.174E-06	1.172E-06
	A_8	1.619E-05	-7.794E-06	-6.032E-06	-3.499E-05	-1.128E-05	-6.056E-06

As seen in Table 5.5, the square root of the estimated variance component, $\hat{\sigma}_0$, is the smallest by using the estimated roll angles for PTP correction. On the other hand, omitting PTP correction results in the largest estimated variance component. In addition, the estimated roll angles (as indicated in Equation 5.13, Section 5.3.2) differ from the true roll angles derived using the navigation data (as indicated in Equation 5.12, Section 5.3.1). The difference is attributed to the assumption made in Section 5.2.3 of a flat terrain. On the other hand, it can be seen that using the estimated roll angles gives better results, in terms of the smallest variance component. In order to evaluate the quality of the estimated 2-D Affine parameters, a space intersection is performed based on the estimated parameters and the coordinates of the points in both left and right scenes, as explained earlier. The estimated object coordinates are then compared to the true values and the errors associated with the points in Tables 5.6.

Table 5.6: Mean and standard deviation of the error values of the indirectly estimated object space GCP and check points

		Errors, m		
		$\text{Mean}_{XY} \pm \text{Std}_{XY}$	$\text{Mean}_{Z} \pm \text{Std}_{Z}$	Mean ± Std
GCP	Without PTP	0.000 ± 1.675	0.000 ± 0.858	0.000 ± 1.882
	With PTP (true roll angle)	0.000 ± 1.699	0.000 ± 0.070	0.000 ± 1.701
	With PTP (estimated roll angle)	0.000 ± 1.685	0.000 ± 0.015	0.000 ± 1.685
Check points	Without PTP	0.674 ± 1.666	0.472 ± 0.486	0.823 ± 1.736
	With PTP (true roll angle)	0.683 ± 1.720	0.030 ± 0.039	0.684 ± 1.721
	With PTP (estimated roll angle)	0.552 ± 1.690	0.002 ± 0.008	0.552 ± 1.690

As shown in Table 5.6, no bias can be seen in the estimation of object coordinates of the GCP. Again, a smaller Z-value of the standard deviation of the errors is achieved using the indirectly estimated roll angle, compared to those using the derived roll angles from the navigation data. The same conclusions can be drawn for the check points (see Table 5.6) except for the existence of bias values. A comparison of Tables 5.6 and 5.4 reveals the suitability of indirect methods (that is, using GCP) compared to the direct methods (that is, using navigation data).

5.6 SUMMARY

In this chapter, the scale modification along the scan line (perspective to parallel transformation) was introduced to alter the scene coordinates generated according to perspective geometry, so as to be closer to the model of a parallel projection. The mathematical model for such a transformation was introduced for scenes whose stereo coverage is achieved across-track through the use of roll angles, as in SPOT scenes, for example. It was found that, for scenes whose stereo coverage is achieved along track using pitch angles (e.g., IKONOS scenes) and those achieved using three-line scanners, no scale modification is required, assuming a zero roll angle.

The mathematical relationship between navigation parameters (scanner EOP) and scene parallel projection parameters was established. At this stage, it is important to mention that the scene parallel projection parameters (L, M, ω, φ, κ, Δx, Δy, s) can be derived in many ways:

- By using navigation data (scanner EOP) directly, without using GCP, as described in Section 5.4.
- By using GCP in Equation 4.4, which represents a non-linear model. Therefore, linearization and approximate values are required for solution by means of an iterative least-squares adjustment.
- By using GCP in Equation 4.10 (a linear model) to obtain the 2D Affine parameters. Then, a transformation from 2D Affine parameters to scene parallel projection parameters can be performed, as described in Section 4.4.4.

Similarly, the roll angle, ψ, can be derived directly using the scanner rotation angles (Section 5.3.1) or estimated indirectly using GCP (see Section 5.3.2). Experiments revealed that the estimated roll angles using GCP produce the smallest errors in the 2-D Affine model, as well as in the object space. It is important to mention that the PTP correction assumes flat terrain.

Up to this point in the development of the wider methodology of this dissertation, the transformation and mathematical relationships between the perspective projection model and the parallel projection model have been established. In Chapter 6, an epipolar resampling approach of linear array scanner scenes according to parallel projection is developed. The perspective-to-parallel transformation discussed in this chapter is, therefore, a pre-requisite for the resampling process in the next chapter.

CHAPTER 6: EPIPOLAR RESAMPLING OF LINEAR ARRAY SCANNER SCENES

6.1 INTRODUCTION

This chapter deals with the epipolar resampling of linear array scanner scenes using the parallel projection model. First, interpretation of the epipolar line parameters will be discussed in Section 6.2. Based on this interpretation, target functions are derived to minimize y-parallax (P_y) in the normalized scenes. An example will then be presented to show the importance of having GCP in epipolar resampling to ensure a linear relationship between x-parallax (P_x) and height (Z). The purpose of Section 6.3 is to develop approaches for epipolar resampling based on the knowledge accumulated throughout this research. Finally, experimental results using synthetic data as well as real data are presented in Section 6.4.

6.2 EPIPOLAR LINE DERIVATION AND PARAMETER UTILIZATION

In this section, a general form of the epipolar line equation is presented. The parameters describing the epipolar line are then analyzed and utilized in order to reduce the y-parallax of the scenes for the purpose of epipolar resampling.

6.2.1 Derivation of Epipolar Line Parameters

Equation 4.42 represents an epipolar line in a scene captured according to parallel projection. Conceptually, this equation describes the mathematical relationship between the coordinates of conjugate points in a stereopair. It is clear that Equation 4.42 represents a straight line in either the left or the right scene; this equation also implies that the epipolar lines are parallel. In other words, for two points (x_1, y_1) and (x_2, y_2) in the left scene, the corresponding epipolar lines in the right scene are represented by ($y' = C_1 x' + C_2 x_1 + C_3 y_1 + C_4$) and ($y' = C_1 x' + C_2 x_2 + C_3 y_2 + C_4$), respectively; that is, they have the same slope, C_1. There is only a shift between these lines along the *y'* direction with the amount of $C_2(x_1-x_2) + C_3(y_1-y_2)$. Similarly, for any two points in the right scene, the corresponding epipolar lines in the left scene will have the same orientation.

However, Equation 4.42 does not represent all straight-line cases in the scene. In other words, singularity will exist for lines parallel to *y'* since C_1 is undefined ($\tan \pi/2 = \infty$). For such cases, *x'* and *y'* can be switched and Equation 4.42 can be rewritten as:

$$x' = C_1' y' + C_2' x + C_3' y + C_4' \tag{6.1}$$

In this representation, lines parallel to the *y'* direction will have no singularity because all the parameters in this equation will have finite values. However, lines parallel to *x'* will have singularity and require working with Equation 4.42. The orientation of the epipolar lines is not known beforehand; that is, it is not known whether the epipolar lines are horizontal or vertical. Therefore, similar to the approach suggested by Habib (1999), Equations 4.42 or 6.1 can be rewritten as:

$$-\frac{C_2}{C_4}x - \frac{C_3}{C_4}y - \frac{C_1}{C_4}x' + \frac{1}{C_4}y' = 1$$

$$G_1 x + G_2 y + G_3 x' + G_4 y' = 1 \tag{6.2}$$

where:

$$G_1 = -\frac{C_2}{C_4}$$

$$G_2 = -\frac{C_3}{C_4}$$

$$G_3 = -\frac{C_1}{C_4}$$

$$G_4 = \frac{1}{C_4}$$

Equation 6.2 represents a more general case, since it represents all straight-lines in the left and right scenes - that is, regardless of their orientation. The parameters in Equation

6.2 can be *directly* computed from the navigation data according to what has been explained in Chapters 4 and 5. This can be achieved by first computing scene parallel projection parameters (see Section 5.3), then by determining the 2-D Affine parameters (Section 4.4.2). Finally, the epipolar line parameters can be derived as discussed in Section 4.5.1 by adapting Equation 6.2.

Alternatively, G_1 to G_4 can be *indirectly* derived using point correspondences (i.e., conjugate points) in the left and right scenes. Then, the estimated parameters can be used to resample the subject scenes according to epipolar geometry. First, at least four tie points are required to determine the parameters, G_1 to G_4, as each point-pair produces one equation of the form in Equation 6.2. It is important to mention that a deficient normal equation matrix signifies the fact that the object space is a planar surface. In such a case, the epipolar lines are reduced to points, similar to what was discussed in Chapter 4.

Regardless of the method of deriving G_1 to G_4, these parameters can be used to establish the necessary transformation for resampling scenes according to epipolar geometry. The next section deals with two different scenarios for utilizing the epipolar line parameters for the purpose of resampling the scenes according to epipolar geometry.

6.2.2 Utilizing Epipolar Line Parameters for Normalized Scene Generation

Scenes resampled according to epipolar geometry should satisfy the following two conditions:

- The epipolar lines should be aligned along the rows of the resampled scenes.
- Conjugate epipolar lines should be aligned along the same row in the final scenes. In other words, there is no P_y between conjugate points in overlapping scenes.

Therefore, each scene needs to be rotated through a different angle (e.g., θ for the left scene and θ' for the right scene) in order to make the epipolar lines parallel to the x and x' axes of the left and right scenes, respectively. However, such rotations do not guarantee that conjugate epipolar lines have the same *y* and *y'* values. Consequently, scale and shift parameters must be applied for this purpose. Such implementation can follow either one of the following two scenarios.

6.2.2.1 Scenario I

In this scenario, the scale and the shift values are applied to only one of the scenes (e.g., the right scene). Therefore, the transformation of the right scene includes rotation, scale and shift, while the transformation of the left scene includes only rotation. These transformations involve four parameters. Adopting such a strategy, the following transformations can be written:

$$\begin{bmatrix} x_n \\ y_n \end{bmatrix} = \begin{bmatrix} \cos(\theta) & \sin(\theta) \\ -\sin(\theta) & \cos(\theta) \end{bmatrix} \begin{bmatrix} x \\ y \end{bmatrix} \tag{6.3}$$

$$\begin{bmatrix} x_n' \\ y_n' \end{bmatrix} = S \begin{bmatrix} \cos(\theta') & \sin(\theta') \\ -\sin(\theta') & \cos(\theta') \end{bmatrix} \begin{bmatrix} x' \\ y' \end{bmatrix} + \begin{bmatrix} 0 \\ \Delta y \end{bmatrix} \tag{6.4}$$

where:

θ	is the rotation angle of the left scene;
θ'	is the rotation angle of the right scene;
S	is the scale factor of the right scene;
Δy	is the *y* shift of the right scene;
(x_n, y_n)	are the coordinates in the left scene after normalization (i.e., left normalized scene coordinates); and
(x'_n, y'_n)	are the coordinates in the right scene after normalization (i.e., right normalized scene coordinates).

In the normalized scenes, *y* coordinates of the tie (conjugate) points should be equal. Therefore, by equating y_n and y'_n in Equations 6.3 and 6.4 results in:

$$-\sin(\theta)x + \cos(\theta)y = -S.\sin(\theta')x' + S.\cos(\theta')y' + \Delta y$$

This equation can be rewritten as:

$$-\frac{\sin(\theta)}{\Delta y}x+\frac{\cos(\theta)}{\Delta y}y+\frac{S.\sin(\theta')}{\Delta y}x'-\frac{S.\cos(\theta')}{\Delta y}y'=1 \tag{6.5}$$

Comparing Equations 6.5 and 6.2, the following equalities can be derived:

$$\begin{aligned} G_1 &= -\frac{\sin(\theta)}{\Delta y} \\ G_2 &= \frac{\cos(\theta)}{\Delta y} \\ G_3 &= \frac{S.\sin(\theta')}{\Delta y} \\ G_4 &= -\frac{S.\cos(\theta')}{\Delta y} \end{aligned} \tag{6.6}$$

From Equations 6.6, the transformation parameters (*θ, θ', S, and Δy*) can be derived as follows:

$$\begin{aligned} \theta &= \arctan\left(-\frac{G_1}{G_2}\right) \\ \theta' &= \arctan\left(-\frac{G_3}{G_4}\right) \\ \Delta y &= -\frac{\sin(\theta)}{G_1}=\frac{\cos(\theta)}{G_2} \\ S &= \frac{G_3\Delta y}{\sin(\theta')}=-\frac{G_4\Delta y}{\cos(\theta')} \end{aligned} \tag{6.7}$$

Therefore, after deriving G_1 to G_4, the transformation parameters can be computed from Equations 6.7. Then, the normalized scenes can be generated using the mathematical relationships in Equations 6.3 and 6.4.

6.2.2.2 Scenario II

Equations 6.3 and 6.4 indicate that only one scale value is applied to one of the scenes. In frame images, as discussed in Section 2.1.3.2, recall that the plane on which the normalized images are projected is selected in such a way as to divide the scaling between the images; that is, by choosing an average rotation angle *ω* across the base. Similarly, it is preferred to introduce two scale values in Equations 6.3 and 6.4; one is smaller than unity and the other is larger than unity while their product equals unity. By enforcing this criterion (using *S* for the right scene scale and 1/*S* for the left scene scale), no additional parameters are introduced. Therefore, Equations 6.3 and 6.4 can be rewritten as:

$$\begin{bmatrix} x_n \\ y_n \end{bmatrix} = \frac{1}{S}\begin{bmatrix} \cos(\theta) & \sin(\theta) \\ -\sin(\theta) & \cos(\theta) \end{bmatrix}\begin{bmatrix} x \\ y \end{bmatrix} + \begin{bmatrix} 0 \\ -\dfrac{\Delta y}{2} \end{bmatrix} \tag{6.8}$$

$$\begin{bmatrix} x_n' \\ y_n' \end{bmatrix} = S\begin{bmatrix} \cos(\theta') & \sin(\theta') \\ -\sin(\theta') & \cos(\theta') \end{bmatrix}\begin{bmatrix} x' \\ y' \end{bmatrix} + \begin{bmatrix} 0 \\ \dfrac{\Delta y}{2} \end{bmatrix} \tag{6.9}$$

In the same manner, the shift value *Δy* is divided between the two scenes. Equating the *y* coordinate values of the above two equations results in:

$$-\frac{\sin(\theta)}{S}x + \frac{\cos(\theta)}{S}y - \frac{\Delta y}{2} = -S.\sin(\theta')x' + S.\cos(\theta')y' + \frac{\Delta y}{2}$$

This equation can be rewritten as:

$$-\frac{\sin(\theta)}{S\Delta y}x + \frac{\cos(\theta)}{S\Delta y}y + \frac{S.\sin(\theta')}{\Delta y}x' - \frac{S.\cos(\theta')}{\Delta y}y' = 1$$

By comparing this equation to Equation 6.2, the following equalities can be written:

$$
\begin{aligned}
G_1 &= -\frac{\sin(\theta)}{S\Delta y}\\
G_2 &= \frac{\cos(\theta)}{S\Delta y}\\
G_3 &= \frac{S.\sin(\theta')}{\Delta y}\\
G_4 &= -\frac{S.\cos(\theta')}{\Delta y}
\end{aligned}
\tag{6.10}
$$

The transformation parameters can therefore be computed as follows:

$$
\begin{aligned}
\theta &= \arctan\left(-\frac{G_1}{G_2}\right)\\
\theta' &= \arctan\left(-\frac{G_3}{G_4}\right)\\
S &= \sqrt{-\frac{G_3\sin(\theta)}{G_1\sin(\theta')}} = \sqrt{-\frac{G_4\cos(\theta)}{G_2\cos(\theta')}}\\
\Delta y &= -\frac{\sin(\theta)}{S.G_1} = \frac{\cos(\theta)}{S.G_2} = \frac{S.\sin(\theta')}{G_3} = -\frac{S.\cos(\theta')}{G_4}
\end{aligned}
\tag{6.11}
$$

In summary, G_1 to G_4 in Equation 6.2 can be computed either *directly* (using navigation data) as explained in Chapters 4 and 5, or *indirectly* using a least-squares adjustment procedure involving identified tie points in the left and right scenes of a stereopair. Subsequently, by adopting Scenario I, the transformation parameters can be computed using Equations 6.7. Then, the normalized scenes can be generated using the mathematical relationships in Equations 6.3 and 6.4. Alternatively, adopting Scenario II, the transformation parameters can be computed using Equations 6.11, and the normalized scenes can be generated using Equations 6.8 and 6.9. In is very important to mention that a perspective-to-parallel correction has to be applied first, as discussed in Chapter 5, prior to handling the scenes as parallel projected scenes.

6.2.3 Example

In this example, the main objective is to verify whether the above transformations are sufficient for epipolar resampling of captured scenes according to parallel projection. For this reason, two scenes were simulated according to parallel projection. Scene parallel projection parameters for the left and right scenes are chosen to be similar to Parameters 1 and Parameters 2, respectively (see Table 4.2). Terrain was simulated with zero elevation and a height variation of ±1000m. The left and right scenes are shown in Figure 6.1.

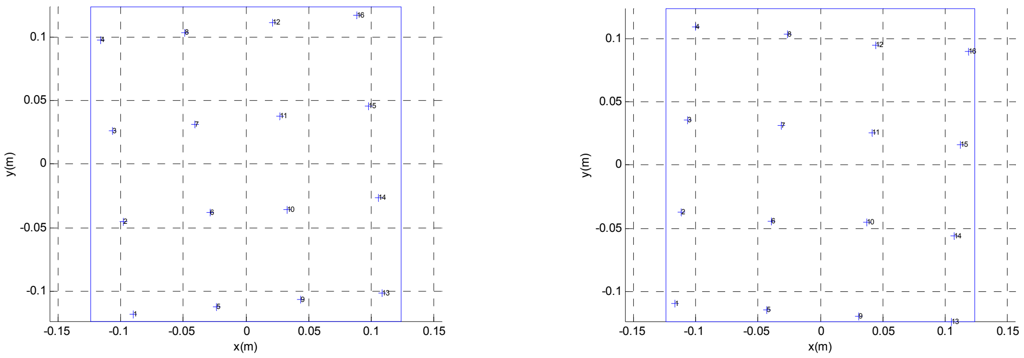

(a) (b)

Figure 6.1: Left Scene (a), and Right Scene (b) generated according to parallel projection

Using the scene coordinates, the estimated epipolar line parameters together with the square root of the variance component are listed in Table 6.1.

Table 6.1: Estimated epipolar line parameters and the square root of the variance component

Parameter	Value
$\hat{\sigma}_0$	0.0 Pixels
G_1	-89.774036
G_2	75.215906
G_3	69.069181
G_4	-90.406242

Adapting Scenarios I and II, the transformation parameters are listed in Table 6.2. This table lists the average P_y, based on the transformations suggested in Section 6.2.2; the transformed scenes are shown in Figure 6.2.

Table 6.2: Derived transformation parameters using Scenarios I and II

	Scenario I	Scenario II
θ, (°)	50.042518	50.042518
θ', (°)	37.379352	37.379352
S	0.971415	0.985604
Δy, (m)	0.008538	0.008663
Mean $\lvert P_y \rvert$, Pixels	0.00	0.00

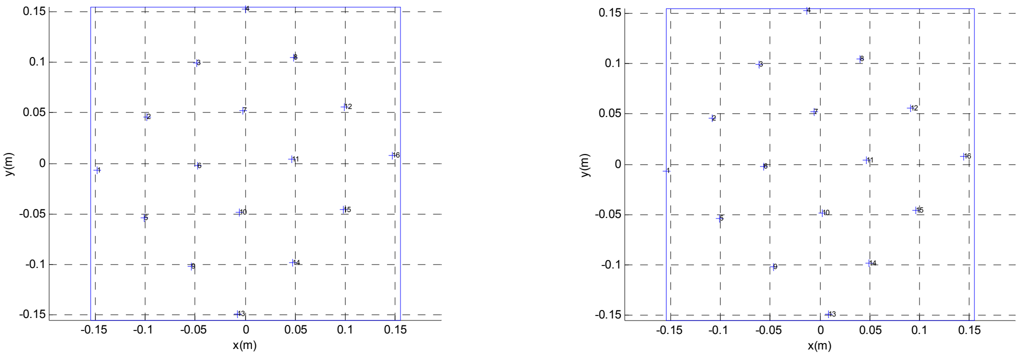

(Left) (Right)

Figure 6.2: Normalized scenes

From Table 6.2 and Figure 6.2, zero P_y is realized for the normalized scenes. Now, the P_x must be analyzed as it is directly related to the elevation values and, consequently, is important for three-dimensional restitution of the object space from the resampled scenes. Figure 6.3 shows the relationship between P_x and elevation (Z). No linear relationship between P_x and Z can be seen. In addition, the estimated variance component from straight-line fitting to the data points, representing the relation P_x versus Z, is 464.8^2 m^2 for both Scenarios I and II.

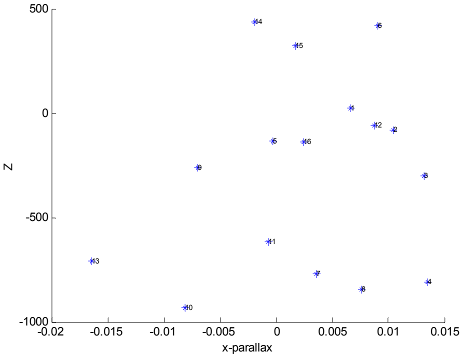

Figure 6.3: The relationship between P_x and Z

From this example, it can be seen that the resulting P_x is not useful for mapping purposes; for example, for recovering the depth information from the corresponding P_x. Therefore, the transformations in Section 6.2.2 are not sufficient for the generation of normalized scenes. At this stage, it is important to redefine the normalized scenes according to epipolar geometry in the following form: *Normalized scenes are those where corresponding points lie along the same row/column (i.e., no y-parallax) AND have x-parallax values that are linearly proportional to the elevation values*.

It is important to note that the suggested transformation (rotation, scale and shift) in Section 6.2.2 does not change the plane where the scene is located. In other words, the values of ω and φ of a scene do not change as a result of this transformation. Therefore, the left and right scenes remain in their own planes after the transformation. As a result, the two scenes might not be in a common plane. In the next section, the plane on which the scenes are first projected, is determined. Recall that epipolar resampling of frame images requires projecting the images into a specific common plane (see Section 2.2.3).

6.2.4 Normalization Plane for the Normalized Scenes

The main emphasis of this section is to decide upon the orientation of the normalization plane, which will contain the normalized scenes. The orientation of that plane will be chosen in such a way that the resulting P_x in the normalized scenes should be linearly proportional to the corresponding elevation of object space points. In other words, points with the same elevation should have the same P_x regardless of their planimetric location.

Before starting this analysis, it is important to note that the epipolar lines are parallel to the plane defined by the parallel projection directions for the left and right scenes, which will be denoted as the *epipolar plane* (see Figure 6.4). There is an infinite number of epipolar planes but for any point, either in the object or scene space, there is only one epipolar plane that passes through this point and which includes the projection directions associated with the left and right scenes. Thus, the epipolar line will be the intersection of this plane with the scene plane.

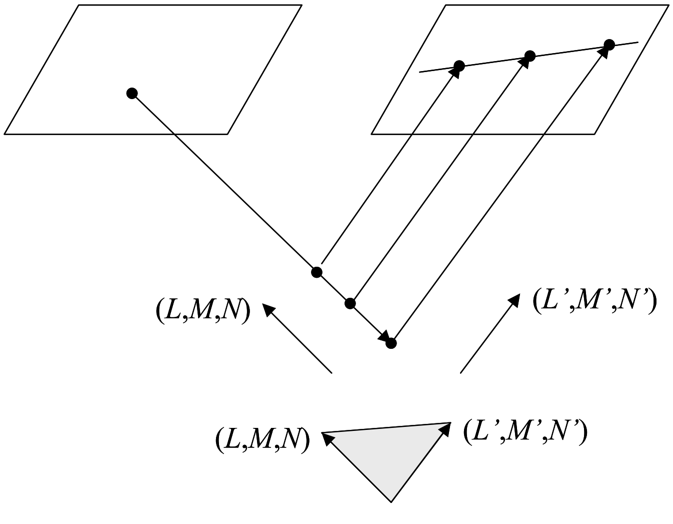

Figure 6.4: Epipolar lines are parallel to the epipolar plane defined by the two parallel projection directions and the object point under consideration

It is important to choose the plane on which the scenes are projected before proceeding with the transformation procedure described in Section 6.2.2 to generate normalized scenes. In order to show this, let us analyze the epipolar plane more closely (see Figure 6.5). This figure contains the epipolar plane, which is the plane of the page, and the intersection of the epipolar plane with the original scenes (epipolar lines). In other words, this figure represents a profile in the scenes along the direction of the epipolar plane.

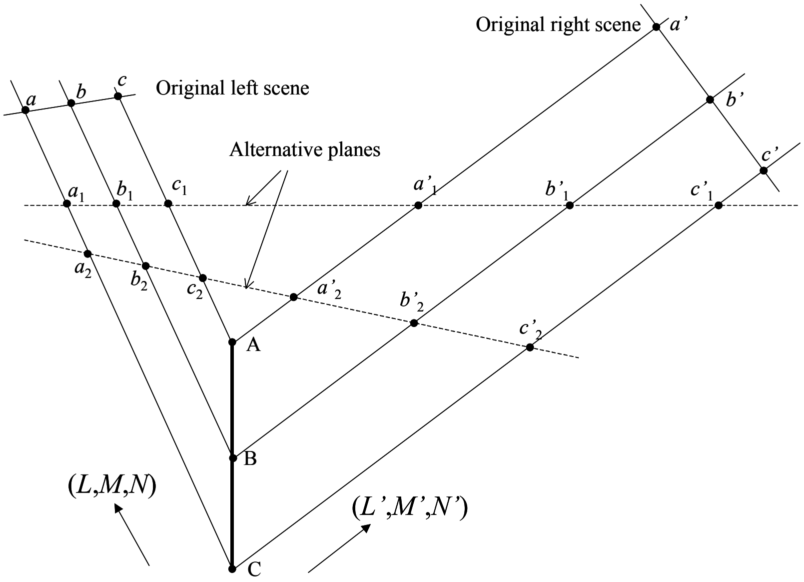

Figure 6.5: P_x of vertically aligned points

In Figure 6.5, points *A*, *B,* and *C* are aligned vertically; that is, they have the same *X*, *Y* but different *Z* values. Moreover, point *B* has the average elevation of points *A* and *C*. One should note that the P_x has to be linearly proportional to the elevation value, so that the normalized stereo scenes become useful for 3-D object space reconstruction. For this reason, the *x*-parallax of the scene point *b* must be the average of the *x*-parallax values of points *a* and *c*. The *x*-parallax values of points *a*, *b*, and *c* will be denoted as P_{xa}, P_{xb}, and P_{xc}, respectively, and can be computed as follows:

$$P_{xa} = x_a - x_{a'}$$
$$P_{xb} = x_b - x_{b'}$$
$$P_{xc} = x_c - x_{c'}$$

Because of the parallel projection, it can be seen that the recorded scene point *b* is the midpoint of *a* and *c* (i.e., $x_b = (x_a + x_c)/2$). Similarly, the recorded scene point *b'* is the midpoint of *a'* and *c'* (i.e., $x_{b'} = (x_{a'} + x_{c'})/2$).

Therefore:

$$\begin{aligned} P_{xb} &= \frac{x_a + x_c}{2} - \frac{x_{a'} + x_{c'}}{2} \\ &= \frac{(x_a - x_{a'}) + (x_c - x_{c'})}{2} \\ &= \frac{P_{xa} + P_{xc}}{2} \end{aligned}$$

It can be proven that, for any plane with any orientation intersecting the epipolar plane (dotted lines in Figure 6.5), the same equation is valid. Thus, the relation between the P_x and elevation, for vertically aligned points (i.e., sharing the same planimetric coordinates), is linear, regardless of the orientation of the plane(s) containing the scenes. However, it is important to analyze the relationship between the P_x and the corresponding elevation for points with different planimetric coordinates.

Figure 6.6 shows two points, *B* and *D*, of the same elevation value but with different planimetric coordinates. The *x*-parallax of point *D*, P_{xd}, is defined as:

$$P_{xd} = x_d - x_{d'}$$

This parallax can be expressed in terms of the *x*-parallax associated with point *B* as follows:

$$\begin{aligned} P_{xd} &= x_d - x_{d'} \\ &= (x_b + bd) - (x_{b'} + b'd') \\ &= (x_b - x_{b'}) + (bd - b'd') \\ &= P_{xb} + (bd - b'd') \end{aligned}$$

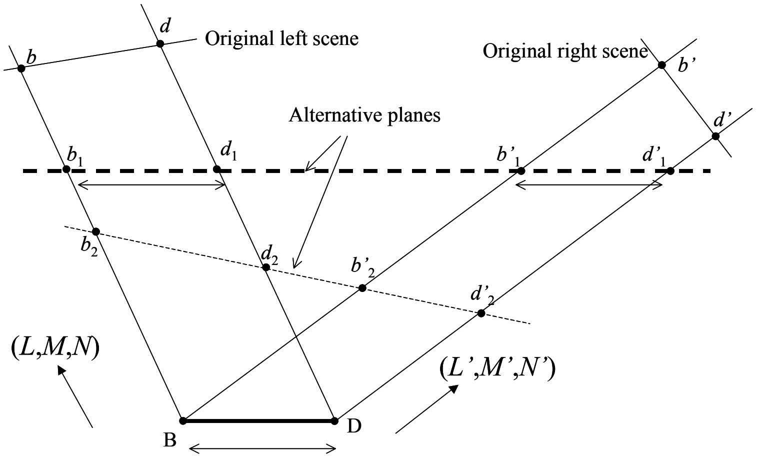

Figure 6.6: P_x for points with the same elevation

Therefore, in order for the two points to have the same P_x, the distances *bd* and *b'd'* should be equal. This will not be the case unless the scene plane is horizontal (i.e., it is parallel to *BD*), as shown by the thick dotted line in Figure 6.6.

In summary, the P_x in the normalized scenes will be linearly proportional to the elevations if and only if the plane including the normalized scenes (the normalization plane) is parallel to the *XY*-plane of the ground coordinate system.

Before developing an approach for normalized scene generation, the incorporation of a horizontal normalization plane is tested in the example introduced in Section 6.2.3. In this case, scenes were projected first on a horizontal plane, each along its own parallel projection direction. The mathematical model for such a transformation is described in Section 4.5.2. After epipolar resampling, P_y was reduced to 0.0 pixels and the relationship between P_x and elevation is a straight line ($\hat{\sigma}_0$=0.0 m for line fitting - see Figure 6.7).

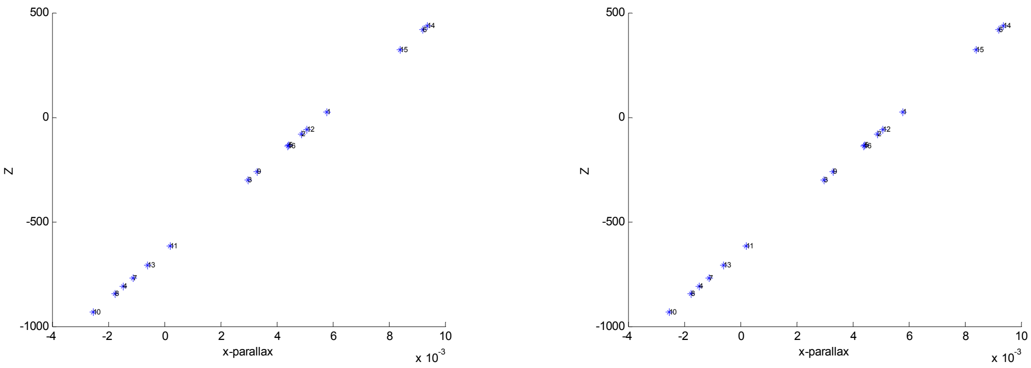

(a) (b)

Figure 6.7: The relationship between P_x and elevation by Adapting Scenario I, (a), and Scenario II (b) after projection into horizontal normalization plane

6.3 UTILIZING PARALLEL PROJECTION PARAMETERS FOR EPIPOLAR RESAMPLING

From the discussion in Section 6.2.4, epipolar lines are parallel to the epipolar planes, defined by the projection directions and the object points under consideration. Therefore, determining this direction (i.e., the direction of the epipolar lines) will directly determine the *x*-axis of the normalized scenes. Figure 6.8 shows the epipolar plane containing the two parallel projection vectors (*L*, *M*, *N*) and (*L'*, *M'*, *N'*). It is important to note that this plane is not necessarily vertical. The direction of the epipolar lines along the normalization plane can be determined by intersecting the epipolar plane with the *XY* plane (which is parallel to the normalization plane). Assuming that the vector (*U*, *V*, 0) is along this intersection, the triple product of the three vectors (*L*, *M*, *N*), (*L'*, *M'*, *N'*) and (*U*, *V*, 0) should be zero (see Figure 6.8):

$$\begin{vmatrix} L & M & N \\ L' & M' & N' \\ U & V & 0 \end{vmatrix} = 0$$

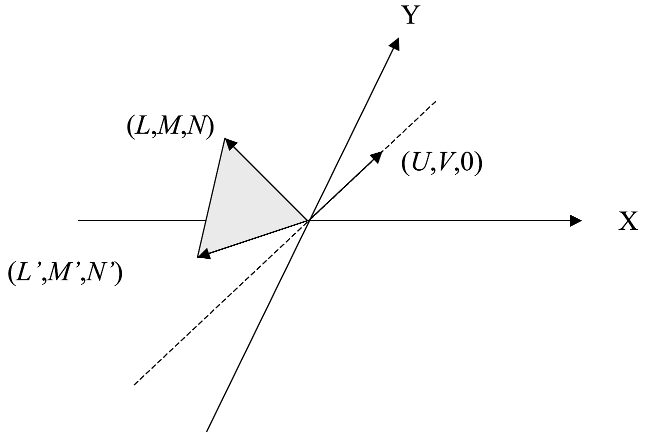

Figure 6.8: Determining the direction of the epipolar lines along the normalization plane

Therefore, the relationship between *U* and *V* can be computed as follows:

$$\left(M.N' - N.M'\right) U + \left(N.L' - L.N'\right) V = 0$$

$$\frac{V}{U} = \frac{N.M' - M.N'}{N.L' - L.N'}$$

The direction of the epipolar lines, κ_n, can be determined as follows:

$$\kappa_n = \arctan\left(\frac{V}{U}\right) = \arctan\left(\frac{N.M' - M.N'}{N.L' - L.N'}\right) \tag{6.12}$$

Therefore, after determining the parallel projection parameters for each scene, the parallel projection parameters of the normalized scenes can be selected as follows:

- ω_n and φ_n are set to zero (to define a horizontal normalization plane).

- κ_n is computed from Equation 6.12 (to define the direction of the epipolar lines along the normalization plane).
- s_n is computed as the average scale of the two scenes.
- Δx_n and Δy_n can be computed as the average shifts of the two scenes.
- L_n, M_n, and N_n are the same as L, M, and N, respectively (same direction vector).
- L'_n, M'_n, and N'_n are the same as L', M', and N', respectively (same direction vector).

Selecting the parallel projection parameters according to the above values will ensure the generation of the normalized scenes with P_x that is linearly proportional to the terrain elevation.

Based on the knowledge accumulated throughout this research, a procedure for epipolar resampling of linear array scanner scenes has been developed. This procedure is summarized in the following steps:

- Scenes must be transformed from perspective to parallel projection, as explained in Chapter 5. This transformation requires a knowledge of the scanner roll angle, which can be directly available from the navigation data (see Section 5.3.1) or indirectly estimated using GCP (see Section 5.3.2).
- Scene parallel projection parameters are then derived. They can be directly derived using navigation data, as discussed in Section 5.4. Alternatively, they can be derived indirectly using GCP. In this case, 2-D Affine parameters are estimated based on GCP, Equations 4.10 or Equations 5.13. Afterwards, scene parallel projection parameters are derived as discussed in Section 4.4.4.
- Normalized scene parallel projection parameters are then computed as explained in this section. They are (ω_n, φ_n, κ_n, s_n, Δx_n, Δy_n, L_n and M_n) for the left normalized scene and (ω_n, φ_n, κ_n, s_n, Δx_n, Δy_n, L'_n and M'_n) for the right normalized scene.

- Finally, the scenes are then re-projected using the normalized parameters. Each scene is re-projected along its own parallel projection direction. The mathematical model for this transformation is derived in Section 4.5.2.

6.4 EXPERIMENTS

In this section, the approach developed for epipolar resampling of linear array scanner scenes is tested, using synthetic and real data.

6.4.1 Experiments using Synthetic Data

To prove the feasibility of the approaches developed in this dissertation, Experiment 6.1, resembling scenes generated by changing the pitch angles similar to the case of IKONOS scenes, was performed. In this experiment, object points were simulated as having a height variation of ±1000m; then, IOP and EOP parameters were selected similar to those of IKONOS. Based on the rigorous perspective model (IOP and EOP), the object points were back-projected into the scene space. Then, a normally distributed noise with a zero mean and standard deviation of 1, 2 and 3 pixels was added to the scene coordinates. The object space points together with the scene footprints are shown in Figure 6.9. In this figure, 16 points shown as red triangles were used as GCP, while 9 points shown in green circles were used as check points. The procedure summarized in the previous section was then performed, producing the results as listed in Table 6.3.

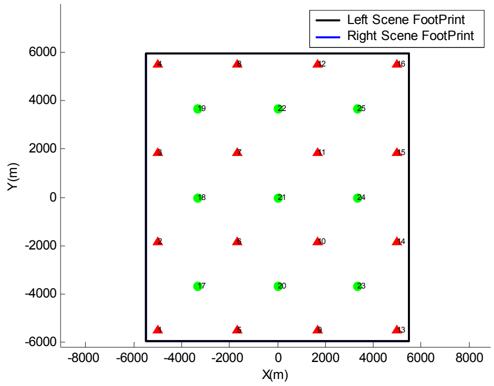

Figure 6.9: Overview of the Object space GCP (red triangles), and check points (green circles), for Experiment 6.1

Table 6.3: Results for Experiment 6.1

σ -Noise, pixels		0	1	2	3
$\widehat{\sigma}_0$ (2-D Affine-Left), pixels		1.5	1.5	2.4	2.6
$\widehat{\sigma}_0$ (2-D Affine-Right), pixels		1.5	1.6	2.4	3.3
Mean|P_y|, pixels		0.0	1.0	1.5	2.6
$\widehat{\sigma}_0$ (line fitting of P_x, Z), m		0.0	1.4	2.6	3.9
GCP	$\text{Mean}_{XY} \pm \text{Std}_{XY}$, m	0.000 ± 1.684	0.000 ± 1.567	0.000 ± 2.171	0.000 ± 2.528
	$\text{Mean}_Z \pm \text{Std}_Z$, m	0.000 ±0.000	0.000 ± 1.399	0.000 ± 2.541	0.000 ± 3.733
Check points	$\text{Mean}_{XY} \pm \text{Std}_{XY}$, m	0.552 ±1.720	0.447 ± 1.880	0.685 ± 1.815	0.762 ± 3.841
	$\text{Mean}_Z \pm \text{Std}_Z$, m	0.000 ±0.000	1.089 ± 1.538	2.068 ± 2.137	0.909 ± 5.235

From Table 6.3 it can be seen that, when the data contain no noise, a linear relationship between P_x and Z is achieved together with the reduction of P_y to zero. As the noise level increases, larger errors are produced. From the error measures in the object space, no biases can be found using the GCP while small bias values exist using check points. In addition, as the error level increases, Std_Z increases faster than Std_{XY}. This observation is highly related to the base-height ratio of the scenes. Future work will investigate the effects of different base-height ratios and the terrain variation on the achieved accuracy.

6.4.2 Experiments using Real Data

A panchromatic stereopair of IKONOS scenes covering Daejeon, South Korea was used in the experiments. The geographical coordinates of the area range from 36.26° to 36.36° North Latitude and from 127.31° to 127.45° East Longitude. An overview of these scenes is shown in Figure 6.10. The number of rows and columns and the acquisition data/time of the scenes are listed in Table 6.4.

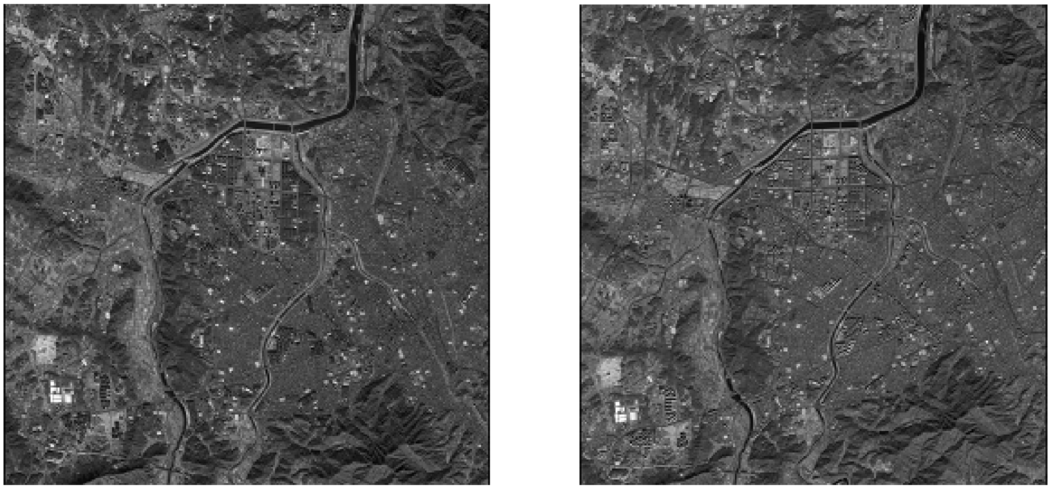
(a) Left Scene (b) Right Scene

Figure 6.10: Overview of the IKONOS scenes

Table 6.4: IKONOS scenes' dimensions and acquisition data/time

	Left	Right
Number of rows	13824	14336
Number of columns	13816	13816
Acquisition date/time	2001-11-19 / 02:18 GMT	2001-11-19 / 02:19 GMT

No information regarding the roll angles of the scenes was available. In addition, no GCP were available. Instead, the rational functions' coefficients (Madani, 1999) of each of the scenes were provided.

Because of the unavailability of GCP, the rational functions' coefficients were used to derive the ground coordinates of measured tie points - 162 points in all (Tao and Hu, 2002). A coordinate transformation was then implemented to obtain GCP in the local Cartesian coordinate system. In this regard, it is important to mention that the accuracy of the estimated object coordinates depends on:

- The measurement accuracy of the scene coordinates;
- The accuracy of the rational functions' coefficients (typically not provided); and
- The validity of the rational functions as an approximate model.

The developed approach for epipolar resampling was then performed, yielding results as listed in Table 6.5. Three sets of experiments were tested using different numbers of GCP and check points.

Table 6.5: Results of resampling approaches of IKONOS data

Experiment		6.2	6.3	6.4
# of GCP		9	25	162
# of Check		153	137	0
$\hat{\sigma}_0$(2-D Affine-Left), pixels		4.8	3.7	2.9
$\hat{\sigma}_0$(2-D Affine-Right), pixels		1.7	1.3	1.1
Mean$\lvert P_y \rvert$, pixels		2.3	1.6	1.5
$\hat{\sigma}_0$(fitting of P_x, Z), m		6.0	6.2	5.4
GCP	Mean$_{XY}$ ± Std$_{XY}$, m	0.000 ± 1.707	0.000 ± 0.993	0.000 ± 0.889
	Mean$_Z$ ± Std$_Z$, m	0.000 ± 5.674	0.000 ± 6.086	0.000 ± 5.450
Check points	Mean$_{XY}$ ± Std$_{XY}$, m	0.103 ± 1.364	0.095 ± 0.930	-
	Mean$_Z$ ± Std$_Z$, m	1.588 ± 6.101	0.587 ± 5.491	-

From Table 6.5, the left scene does not completely conform to the parallel projection model compared to the right scene as indicated by the large estimated variance component. One has to note that the provided IKONOS scenes might not be raw (unprocessed) scenes. From the same table, an insignificant improvement between Experiments 6.3 and 6.4 can be seen. Thus, it can be concluded that just a few GCP can be used for epipolar resampling according to the approach developed in this research. In addition, the standard deviation of the error values of the check points are not significantly different from those of the GCP. Therefore, the suggested approaches achieve similar errors throughout the resulting normalized stereopair. In other words, errors 'far from' the GCP are similar to those 'close to' the GCP.

The scenes resampled according to epipolar geometry are shown side-by-side in Figure 6.11. The two scenes are overlaid to generate a stereo anaglyph (see Figure 6.12) which can be stereo-viewed using anaglyph glasses.

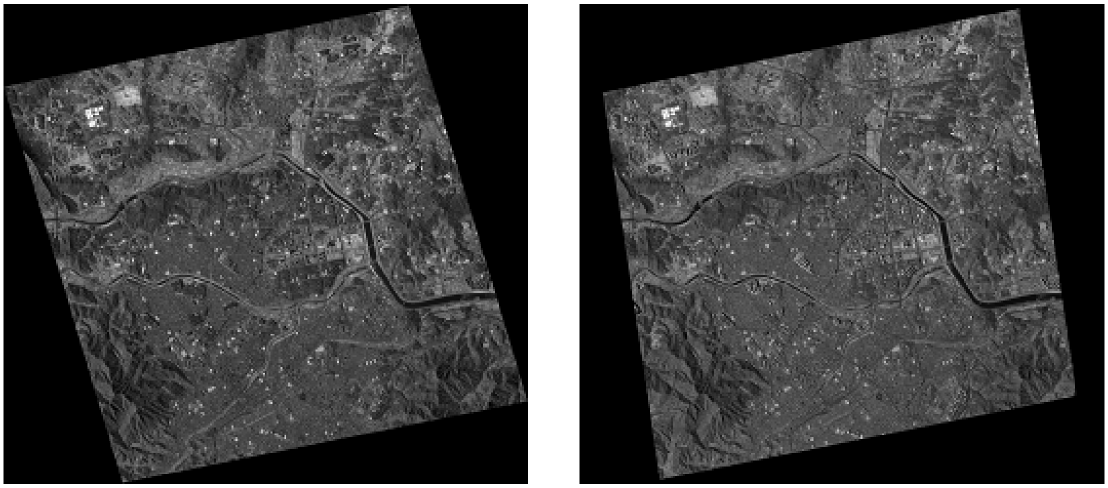

(a) Left Scene (b) Right Scene

Figure 6.11: Normalized Scenes

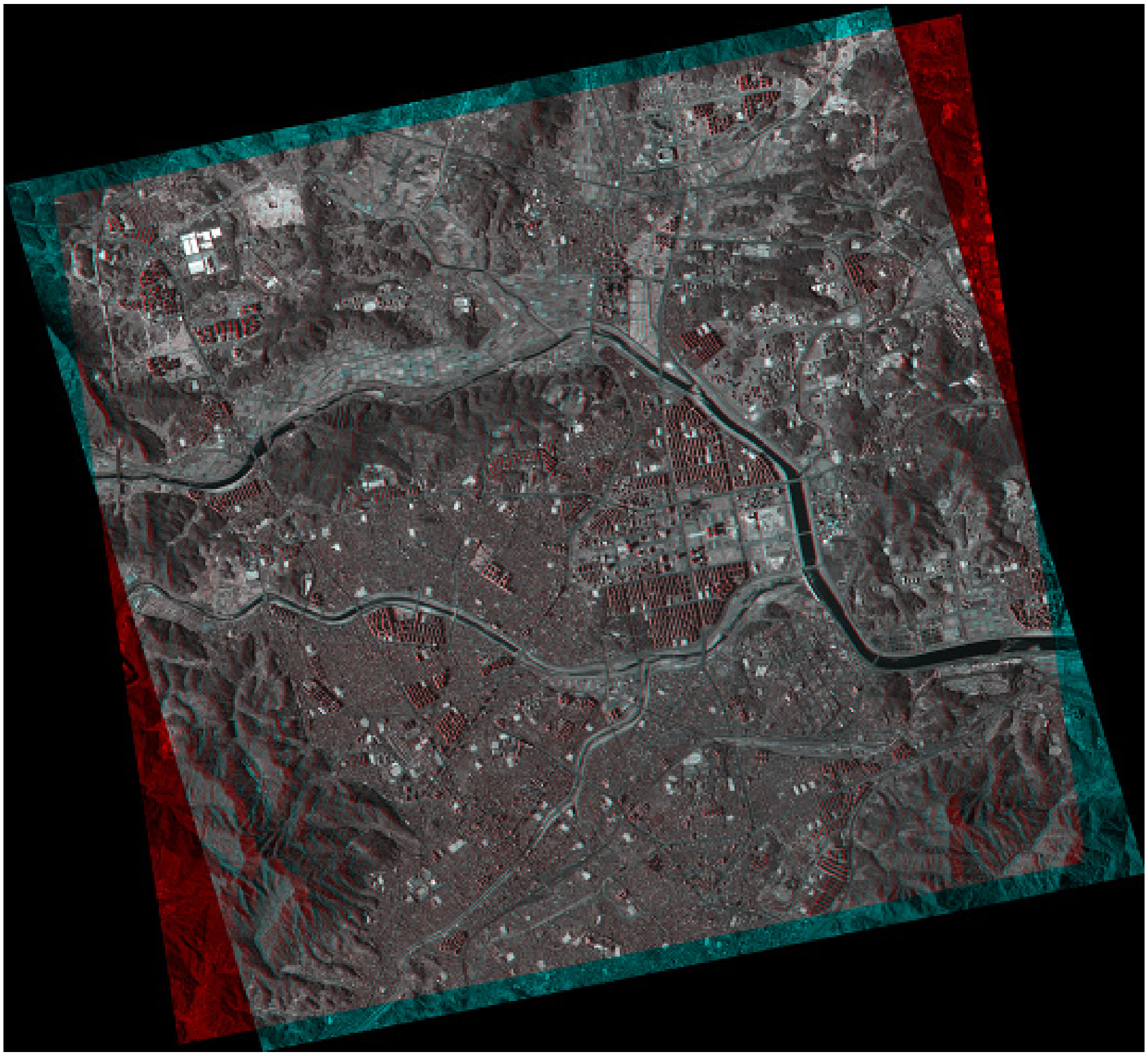

Figure 6.12: Stereo anaglyph of the normalized scenes

6.5 SUMMARY

In this chapter, normalized scenes were strictly defined as those having the following properties:

- P_y is zero to ensure that conjugate points or epipolar lines belong to the same row/column. No control information is required at this stage.

- P_x is linearly related to Z in order to have a useful normalized stereopair where estimated height should be linearly related to the true height. Control information is required to meet this requirement.

An approach for the epipolar resampling of linear array scanner scenes has been developed. In this approach, scene parallel projection parameters (derived from GCP or navigation data) are utilized to derive the required transformations. Perspective-to-parallel correction is a prerequisite and can performed as explained in Chapter 5. Experiments using synthetic and real data showed the feasibility of the developed approach.

CHAPTER 7: CONCLUSIONS AND RECOMMENDATIONS

7.1 SUMMARY AND CONCLUSIONS

The main objective of this research is to generate normalized scenes obtained by linear array scanners. Normalized scenes, in regard to matching problems, have the prime advantage of reduced search space and computation time in addition to reducing matching ambiguities. This makes the normalized scene important and pre-requisite for wide variety of applications such as automatic matching, automatic relative orientation, automatic aerial triangulation, automatic DEM generation, ortho-photo generation, and stereo viewing.

Chapter 2 provided an introduction of epipolar geometry and resampling of imagery captured by frame cameras. In Chapter 2, linear array scanners were introduced together with their rigorous and approximate modeling as reported in literature. Based on the fact that epipolar lines in frame images are straight lines, the shape analysis of epipolar lines in linear array scanners becomes important.

Chapter 3 presented the shape analysis of epipolar lines in scenes captured by linear array scanners moving with constant velocity and constant attitude. In addition, the effect of different stereo-imaging configurations on the shape of epipolar lines was studied. Based on this analysis, it was concluded that linear array scanners do not, in general, produce straight lines. Moreover, for high altitude scanners with narrow AFOV moving with constant velocity and constant attitude, epipolar lines become straighter. Given this background, an alternative model was sought to represent such scenes.

Parallel projection, as an alternative model was presented in Chapter 4. The relationship between the object and corresponding scene coordinates in imagery captured according to parallel projection was derived in Chapter 4. The mathematical relationship between the parallel projection parameters and the 2-D Affine transformation parameters (forward and backward transformations) was derived. In addition, the mathematical relationship between corresponding points in two scenes generated according to parallel projection as well as the epipolar line equation was derived. As this chapter deals with scenes complying with parallel projection, which is different from the rigorous perspective model, transformation between the models becomes a prerequisite.

Chapter 5 dealt with the transformation from perspective to parallel projection of scenes captured by linear array scanners. Such a transformation requires a knowledge of the scanner roll angle, which can be obtained directly from the navigation data or indirectly using GCP. The mathematical relationship between the navigation parameters (scanner EOP) of the original scenes and the parallel projection parameters of the transformed scenes according to parallel projection was derived.

Based on the knowledge accumulated throughout this research, Chapter 6 deals with developing an approach for epipolar resampling of linear array scanner scenes. The developed approach was then tested using synthetic as well as real data.

The procedure and analysis described above allowed certain conclusions to be reached. First, the nature of epipolar lines is a function of the scanner type and imaging configuration. Moreover, scenes with stereo-coverage achieved along track using pitch angles as well as three-line scanners results in epipolar lines that are closer to straight lines than those achieved in scenes with across-track stereo coverage, using roll angles.

Second, for high altitude photography with narrow AFOV, the perspective imaging can be approximated by parallel projection.

Third, for scenes captured according to exact parallel projection, the fate of epipolar lines varies with planarity of the object space:

1. For non-planar object space, straight epipolar lines are obtained. Therefore, scenes can be resampled according to epipolar geometry.

2. For planar object space, the 1-D epipolar lines would reduce to 0-D points. Therefore, the exact correspondence between conjugate points can be precisely established.

Fourth, scenes generated according to perspective geometry can be transformed into parallel projection to maintain uniform scale. For scenes whose stereo coverage is achieved along track using pitch angles as well as using three-line scanners, no scale modification is required.

Fifth, transformation from perspective to parallel projection requires a knowledge of the roll angle. Two alternatives can be used for deriving the roll angle:

1. Directly, using the scanner orientation angles as explained in Section 5.3.1.
2. Indirectly, using GCP, as explained in Section 5.3.2.

Sixth, parallel projection parameters can be derived in three possible ways:

1. Using control points in Equations 4.4, which constitute a non-linear model.
2. Using control points in Equations 4.10, which constitutes a linear model to obtain the 2D Affine parameters, or Equations 5.13, followed by a transformation from 2D Affine parameters to scene parallel projection parameters, as described in Section 4.4.4.
3. Using navigation data (scanner EOP) directly, without using control information, as described in Chapter 5.

Seventh, epipolar resampling of linear array scanner scenes have the following objectives:

1. Eliminating y-parallax, to obtain conjugate points or epipolar lines along the same rows (or columns). Conjugate points are needed, while no GCP is required, for this purpose.

2. Having *x*-parallax linearly related to the elevation, to obtain useful normalized stereopair. Control information (e.g., GCP) is required for this objective.

Eighth, by combining the objectives identified in the seventh conclusion, it is reasonable to find that epipolar resampling requires control information. An approach for epipolar resampling was developed, by utilizing scene parallel projection parameters (obtained from navigation data or GCP) to compute the necessary transformation parameters.

Ninth, epipolar resampling requires the projection of the scenes on a normalization plane, which has to be horizontal.

Tenth, experimental results using synthetic data as well as real data proved the feasibility of the developed approach.

7.2 RECOMMENDATIONS FOR FUTURE WORK

Recommendations for future work include performing more experiments using synthetic data to investigate the effect of different base-height ratios, different noise levels and different terrain variations on the developed epipolar resampling approach. Additional experiments using real data (such as SPOT scenes) are also recommended to test the generality of the developed approach.

Future work should also include an enhancement of the perspective-to-parallel model to incorporate knowledge of the trend of the terrain as it could be indicated from GCP. In addition, direct and indirect methods for epipolar resampling may be compared in terms of the achieved accuracy.

Parallel projection models can be included in photogrammetric triangulations. Higher order primitives (e.g., linear and areal features) can also be incorporated in the parallel projection model. In addition, object space constraints can be utilized to reduce the minimum requirement of GCP. Finally, DEM and ortho-photos can be generated based on the normalized scenes.

BIBLIOGRAPHY

Abdel-Aziz, Y., and H. Karara, 1971. Direct Linear Transformation from Comparator Coordinates into Object Space Coordinates in Close-Range Photogrammetry, *Proceedings of ASP/UI Symposium on CloseRange Photogrammetry*, University of Illinois at Urbana Champaign, Urbana, Illinois, pp. 1-18.

Baltsavias, E., M. Pateraki, and L. Zhang, 2001. Radiometric and geometric evaluation of Ikonos Geo images and their use for 3D building modeling. *Proc. Joint ISPRS Workshop High Resolution Mapping from Space 2001*, Hanover, 2001.

Cho, W., T. Schenk, and M. Madani, 1992. Resampling Digital Imagery to Epipolar Geometry, *IAPRS International Archives of Photogrammetry and Remote Sensing*, 29(B3): 404-408.

Dowman, I., and J. Dolloff, 2000. An Evaluation of Rational Functions for Photogrammetric Restitutions, *International Archives of Photogrammetry and Remote Sensing*, 33 (Part B3): 254-266.

Ethridge, M., 1977. Geometric Analysis of Single and Multiply Scanned Aircraft Digital Data Array, PhD Thesis, Purdue University, West Lafayette, Indiana, 301p.

Fraser, C., 2000. High-Resolution Satellite Imagery: A Review of Metric Aspects, *IAPRS*, 33(B7): 452-459.

Fraser, C., and H. Hanley, 2003. Bias Compensation in Rational Functions for IKONOS Satellite Imagery, *Journal of Photogrammetric Engineering & Remote Sensing*, 69(1): 53:57.

Fraser, C., H. Hanley, and T. Yamakawa, 2001. Sub-Metre Geopositioning with IKONOS GEO Imagery, *ISPRS Joint Workshop on High Resolution Mapping from Space*, Hanover, Germany, 2001.

Fraser, C., H. Hanley, and T. Yamakawa, 2002. Three-Dimensional Geopositioning Accuracy of IKONOS Imagery, *Journal of Photogrammetric Record*, 17(99): 465-479.

Fritz, L., 1995. Recent Developments for Optical Earth Observation in the United States, *Photogrammetric Week*, pp75-84, Stuttgart, 1995.

Grodecki, J., and G. Dial, 2003. Block Adjustment of High Resolution Satellite Images Described by Rational Polynomials, *Journal of Photogrammetric Engineering & Remote Sensing*, 69(1):59-68.

Habib, A., 1999. Aerial Triangulation using Point and Linear Features*, International Archives of Photogrammetry and Remote Sensing on Automatic Extraction of GIS Objects from Digital Imagery,* München, Germany, 32(3-2W5): 137-142.

Habib, A., and B. Beshah, 1998a. Modeling Panoramic Linear Array Scanner. *ISPRS Commission III Symposium*, Columbus, Ohio (6 – 10 July, 1998).

Habib, A. and Beshah, B., 1998b. Multi Sensor Aerial Triangulation. *ISPRS Commission III Symposium*, Columbus, Ohio (6 – 10 July, 1998).

Habib, A., Y. Lee, and M. Morgan, 2001. Bundle Adjustment with Self-Calibration of Line Cameras using Straight Lines. *Joint Workshop of ISPRS WG I/2, I/5 and IV/7: High Resolution Mapping from Space 2001*, University of Hanover (19-21 September, 2001).

Hanley, H., and C. Fraser, 2001. Geopositioning Accuracy of IKONOS Imagery: Indications from Two Dimensional Transformations, *Journal of Photogrammetric Record*, 17(98): 317-329.

Hanley, H., T. Yamakawa, and C. Fraser, 2002. Sensor Orientation for High Resolution Satellite Imagery, *Pecora 15/Land Satellite Information IV/ISPRS Commission I/FIEOS*, Denver 2002.

Hattori, S., T. Ono, C. Fraser, and H. Hasegawa, 2000. Orientation of High-Resolution Satellite Images Based on Affine Projection, *IAPRS International Archives of Photogrammetry and Remote Sensing*, 33(B3): 359-366.

Heipke, C., W. Kornus, and A. Pfannenstein, 1996. The Evaluation of MEOSS Airborne Three-Line Scanner Imagery: Processing Chain and Results, *Journal of Photogrammetric Engineering & Remote Sensing*, 62(3): 293-299.

Kim, T., 2000. A Study on the Epipolarity of Linear Pushbroom Images, *Journal of Photogrammetric Engineering & Remote Sensing*, 66(8): 961-966.

Kraus, K., 1993. *Photogrammetry*, Dümmler Verlag, Bonn., Volume 1, 397p.

Lee, Y., and A. Habib, 2002. Pose Estimation of Line Cameras Using Linear Features, *ISPRS Symposium of PCV'02 Photogrammetric Computer Vision*, Graz, Austria.

Lee, C., H. Theiss, J. Bethel, and E. Mikhail, 2000. Rigorous Mathematical Modeling of Airborne Pushbroom Imaging Systems, *Journal of Photogrammetric Engineering & Remote Sensing*, 66(4): 385-392.

Luong, Q., and O. Faugeras, 1996. The Fundamental Matrix: Theory, Algorithms, and Stability Analysis, International Journal of Computer Vision, 17(1): 43-76.

Madani, M., 1999. Real-Time Sensor-Independent Positioning by Rational Functions. *Proceedings of ISPRS Workshop on "Direct versus Indirect Methods of Sensor Orientation"*, 25-26 November, Barcelona, Spain, pp. 64-75.

McGlone, C., 1996. Sensor Modeling in Image Registration, *Digital Photogrammetry: An Addendum* (C. W. Greve, editor), American Society of Photogrammetry and Remote Sensing, Bethesda, Maryland, pp. 115-123.

McGlone, C., and E. Mikhail, 1981. Photogrammetric Analysis of Aircraft Multispectral Scanner Data, School of Civil Engineering, Purdue University, West Lafayette, Indiana, 178p.

Okamoto, A., 1992. Ultra-Precise Measurement using Affine Transformation, *IAPRS International Archives of Photogrammetry and Remote Sensing*, 29(B2): 318-322.

Okamoto, A., S. Akamatu, and H. Hasegawa, 1992. Orientation Theory for Satellite CCD Line-Scanner Imageries of Hilly Terrains, *IAPRS International Archives of Photogrammetry and Remote Sensing*, 29(B2): 217-222.

Okamoto, A., and C. Fraser, 1998. An Alternative Approach to the Triangulation of SPOT Imagery, *IAPRS International Archives of Photogrammetry and Remote Sensing*, 32(4): 457-462.

Okamoto, A., S. Hattori, H. Hasegawa, and T. Ono, 1996. Orientation and Free Network Theory of Satellite CCD Line-Scanner Imagery, *IAPRS International Archives of Photogrammetry and Remote Sensing*, 31(B3): 604-610.

Ono, T., Y. Honmachi, and S. Ku, 1999. Epipolar Resampling of High Resolution Satellite Imagery, Joint Workshop of ISPRS WG I/1, I/3 and IV/4 Sensors and Mapping from Space.

Ono, T., A. Okamoto, S. Hattori, and H. Hasegawa, 1996. Fundamental Analytic of Satellite CCD Camera Imagery Using Affine Transformation, *IAPRS International Archives of Photogrammetry and Remote Sensing*, 31(B3): 611-615.

Ono, T., S. Hattori, H. Hasegawa, and S. Akamatsu, 2000. Digital Mapping using High Resolution Satellite Imagery based on 2-D Affine Projection Model, *IAPRS International Archives of Photogrammetry and Remote Sensing*, 33(B3): 672-677.

Orun, A., and K. Natarajan, 1994. A Modified Bundle Adjustment Software for SPOT Imagery and Photography: Tradeoff, *Journal of Photogrammetric Engineering & Remote Sensing*, 60(12): 1431-1437.

Paderes, J., E. Mikhail, and J. Fagerman, 1989. Batch and On-Line Evaluation of Stereo-SPOT Imagery, *Proceedings of the ASPRS-ACSM Convention*, 02-07 April, Baltimore, Maryland, pp. 21-40.

Papadimitriou, D., and T. Dennis, 1996. Epipolar Line Estimation and Rectification for Stereo Image Pairs, IEEE Transactions on Image Processing, 5(4):672-676.

Sandau, R., B. Braunecker, H. Driescher, A. Eckardt, S. Hilbert, J. Hutton, W. Kirchhofer, E. Lithopoulos, R. Reulke, and S. Wicki, 2000. Design Principles of the LH Systems ADS40 Airborne Digital Sensor, *International Archives of Photogrammetry and Remote Sensing*, Amsterdam, 33(B1): 258-265.

Schenk, T., 1990. Computation of Epipolar Geometry, Technical Notes in Photogrammetry, No. 5, Department of Civil and Environmental Engineering and Geodetic Science, The Ohio State University.

Schenk, T., 1999. Digital Photogrammetry - Volume I, TerraScience, Laurelville, Ohio, USA, 428p.

Tao, V., and Y. Hu, 2001. A Comprehensive Study for Rational Function Model for Photogrammetric Processing, *Journal of Photogrammetric Engineering & Remote Sensing*, 67(12):1347-1357.

Tsioukas, V., E. Stylianidis, and P. Patias, 2000. Epipolar Images for Close Range Applications, *IAPRS International Archives of Photogrammetry and Remote Sensing*, 33(B5): 145-150.

Wang, Y., 1999. Automated Triangulation of Linear Scanner Imagery, *Joint Workshop of ISPRS WG I/1, I/3 and IV/4 on Sensors and Mapping from Space*, Hanover, 1999.

Zhang, Z., R. Deriche, O. Faugeras, and Q. Luong, 1995. A Robust Technique for Matching Two Uncalibrated Images Through the Recovery of the Unknown Epipolar Geometry, Artificial Intelligence Journal, Vol.78, pages 87-119.

APPENDIX A: ANALYSIS OF THE ROTATION MATRIX

A.1 OBJECTIVES

The rotation matrix of the collinearity equations has important properties that are utilized in this dissertation. The elements of the rotation matrix have significant meaning that can be used to define the parallel projection direction, as in Chapter 5. The rotation matrix cannot be defined in separation from the collinearity equations. Therefore, Section A.2 introduces the collinearity equations together with the associated rotation matrix. In Section A.3, the orthonormality property of the rotation matrix is introduced. Finally, Section A.4 deals with defining the orientation vectors of frame images.

A.2 COLLINEARITY EQUATIONS

The main objective of the collinearity equations is to define the mathematical relationship between the image and object space coordinates in perspective views. The concept of the collinearity equations states that the image point, object point and the perspective center are collinear; that is, they belong to one straight line – see Figure A.1.

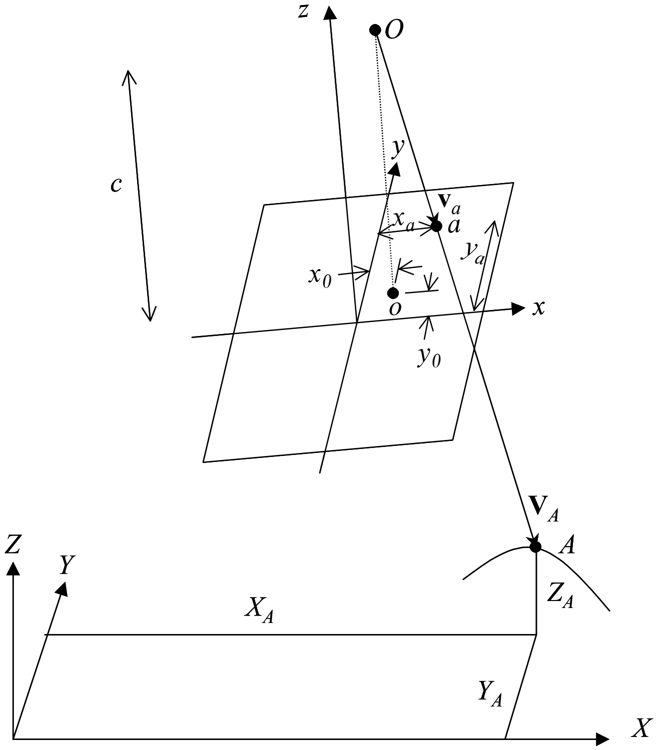

Figure A.1: Concept of collinearity equations – Object point *A*, image point *a*, and perspective center *O* are collinear

A.2.1 Mathematical Derivation

Figure A.1 shows an object point *A* mapped as point *a* in a frame image whose perspective center is *O*. The image coordinate system (a right handed system) can be defined in such a way as to have its origin at the fiducial center (in the case of analog cameras) or the center of the 2-D array (in the case of digital cameras). *x*- and *y*-axes are perpendicular to each other and lie within the image plane. The *z*-axis is normal to the image plane pointing upwards. Due to possible manufacturing imperfections, the perspective center *O* might be shifted from the *z*-axis by distances of x_0 and y_0 in the *x* and *y* directions, respectively. Coordinates of point *O* with respect to the image coordinate system are then $(x_0, y_0, c)^T$ where *c* is the camera principal distance. It is important to note that line *Oo* represents the optical axis of the lens, while point *o* is the principal points, i.e., the intersection of the optical axis with the image plane. For any point a in the image, its coordinates with respect to the image coordinate system are $(x_a, y_a, 0)^T$. Vector $\mathbf{v}_a$, connecting the perspective center and the image point, can be defined with respect to the image coordinate system as:

$$\mathbf{v}_a = \begin{bmatrix} x_a \\ y_a \\ 0 \end{bmatrix} - \begin{bmatrix} x_0 \\ y_0 \\ c \end{bmatrix} = \begin{bmatrix} x_a - x_0 \\ y_a - y_0 \\ -c \end{bmatrix} \tag{A.1}$$

For the object point A, its coordinates with respect to the object coordinate system are $(X_A, Y_A, Z_A)^T$. The coordinates of the perspective center O with respect to the object coordinate systems are $(X_0, Y_0, Z_0)^T$. Therefore, vector $\mathbf{V}_A$, connecting the perspective center and the object point, can be defined with respect to the object coordinate system as:

$$\mathbf{V}_A = \begin{bmatrix} X_A \\ Y_A \\ Z_A \end{bmatrix} - \begin{bmatrix} X_0 \\ Y_0 \\ Z_0 \end{bmatrix} = \begin{bmatrix} X_A - X_0 \\ Y_A - Y_0 \\ Z_A - Z_0 \end{bmatrix} \tag{A.2}$$

Three independent rotation angles are used to represent the rotation between the object and image coordinate systems. This dissertation employs the convention that the rotation matrix is from the image coordinate system to the object coordinate system. The rotation matrix can be expressed as follows:

$$\begin{aligned} R &= \begin{bmatrix} r_{11} & r_{12} & r_{13} \\ r_{21} & r_{22} & r_{23} \\ r_{31} & r_{32} & r_{33} \end{bmatrix} = R_\omega R_\varphi R_\kappa \\ &= \begin{bmatrix} 1 & 0 & 0 \\ 0 & \cos\omega & -\sin\omega \\ 0 & \sin\omega & \cos\omega \end{bmatrix} \begin{bmatrix} \cos\varphi & 0 & \sin\varphi \\ 0 & 1 & 0 \\ -\sin\varphi & 0 & \cos\varphi \end{bmatrix} \begin{bmatrix} \cos\kappa & -\sin\kappa & 0 \\ \sin\kappa & \cos\kappa & 0 \\ 0 & 0 & 1 \end{bmatrix} \\ &= \begin{bmatrix} \cos\varphi\cos\kappa & -\cos\varphi\sin\kappa & \sin\varphi \\ \cos\omega\sin\kappa + \sin\omega\sin\varphi\cos\kappa & \cos\omega\cos\kappa - \sin\omega\sin\varphi\sin\kappa & -\sin\omega\cos\varphi \\ \sin\omega\sin\kappa - \cos\omega\sin\varphi\cos\kappa & \sin\omega\cos\kappa + \cos\omega\sin\varphi\sin\kappa & \cos\omega\cos\varphi \end{bmatrix} \end{aligned} \tag{A.3}$$

where ω is the primary rotation around the X-axis; φ is the secondary rotation around the Y-axis; and κ is the tertiary rotation around the Z-axis.

The collinearity equations state that the two vectors $\mathbf{v}_a$ and $\mathbf{V}_A$ are collinear (see Figure A.1). Therefore:

$$\mathbf{V}_A = \frac{1}{\lambda} R.\mathbf{v}_a$$

Expressing the components of the vectors $\mathbf{v}_a$ and $\mathbf{V}_A$ results in:

$$\begin{bmatrix} X_A - X_0 \\ Y_A - Y_0 \\ Z_A - Z_0 \end{bmatrix} = \frac{1}{\lambda} R \begin{bmatrix} x_a - x_0 \\ y_a - y_0 \\ -c \end{bmatrix} \tag{A.4}$$

where λ is a scale factor, which is the ratio between the length of vector $\mathbf{v}_a$ to the length of vector $\mathbf{V}_A$. It is important to note that vector $\mathbf{v}_a$ is pre-multiplied by the rotation matrix R in order to transform it to the object coordinate system.

Pre-multiplying both sides of Equations A.4 with the rotation matrix R^{T}, and using the orthonormality property of the rotation matrix (i.e., $R^{\mathrm{T}}R=I$, Equation A.20) result in:

$$\begin{bmatrix} x_a - x_0 \\ y_a - y_0 \\ -c \end{bmatrix} = \lambda R^T \begin{bmatrix} X_A - X_0 \\ Y_A - Y_0 \\ Z_A - Z_0 \end{bmatrix} \tag{A.5}$$

Equations A.4 and A.5 are alternative forms of the collinearity equations containing the scale factor λ. Dividing the first and second equations by the third one in Equations A.4 and A.5, to eliminate the scale factor, and rearranging result in:

$$\begin{aligned} X_A &= X_0 + (Z_A - Z_0)\frac{r_{11}(x_a - x_0) + r_{12}(y_a - y_0) + r_{13}(-c)}{r_{31}(x_a - x_0) + r_{32}(y_a - y_0) + r_{33}(-c)} \\ Y_A &= Y_0 + (Z_A - Z_0)\frac{r_{21}(x_a - x_0) + r_{22}(y_a - y_0) + r_{23}(-c)}{r_{31}(x_a - x_0) + r_{32}(y_a - y_0) + r_{33}(-c)} \end{aligned} \tag{A.6}$$

$$\begin{aligned} x_a &= x_0 - c\frac{r_{11}(X_A - X_0) + r_{21}(Y_A - Y_0) + r_{31}(Z_A - Z_0)}{r_{13}(X_A - X_0) + r_{23}(Y_A - Y_0) + r_{33}(Z_A - Z_0)} \\ y_a &= y_0 - c\frac{r_{12}(X_A - X_0) + r_{22}(Y_A - Y_0) + r_{32}(Z_A - Z_0)}{r_{13}(X_A - X_0) + r_{23}(Y_A - Y_0) + r_{33}(Z_A - Z_0)} \end{aligned} \tag{A.7}$$

Equations A.6 and A.7 are other alternative forms of the collinearity equations.

A.3 Orthogonality and Orthonormality of the Rotation Matrix

In order to prove the orthonormality of the rotation matrix *R*, the following characteristics must be proven:

- The norm of each row or column in the rotation matrix is unit (normality condition).
- The dot product of any two different rows or columns is zero (orthogonality condition).

The norm of the first, second and third rows are $|\mathbf{r}_1|$, $|\mathbf{r}_2|$, and $|\mathbf{r}_3|$, respectively, and can be computed as:

$$\begin{aligned} |\mathbf{r}_1| &= \sqrt{r_{11}^2 + r_{12}^2 + r_{13}^2} \\ &= \sqrt{(\cos\varphi\cos\kappa)^2 + (-\cos\varphi\sin\kappa)^2 + (\sin\varphi)^2} \\ &= \sqrt{(\cos\varphi)^2\left((\sin\kappa)^2 + (\cos\kappa)^2\right) + (\sin\varphi)^2} \\ &= \sqrt{(\cos\varphi)^2 + (\sin\varphi)^2} \\ &= \sqrt{1} = 1 \end{aligned} \tag{A.8}$$

$$
\begin{aligned}
|\mathbf{r}_2| &= \sqrt{r_{21}^2 + r_{22}^2 + r_{23}^2} \\
&= \sqrt{(\cos\omega \sin\kappa + \sin\omega \sin\varphi \cos\kappa)^2 + (\cos\omega \cos\kappa - \sin\omega \sin\varphi \sin\kappa)^2 + (-\sin\omega \cos\varphi)^2} \\
&= \sqrt{(\cos\omega)^2 \left((\sin\kappa)^2 + (\cos\kappa)^2\right) + (\sin\omega \sin\varphi)^2 \left((\sin\kappa)^2 + (\cos\kappa)^2\right) + (\sin\omega \cos\varphi)^2} \\
&= \sqrt{(\cos\omega)^2 + (\sin\omega \sin\varphi)^2 + (\sin\omega \cos\varphi)^2} \\
&= \sqrt{(\cos\omega)^2 + (\sin\omega)^2 \left((\sin\varphi)^2 + (\cos\varphi)^2\right)} \\
&= \sqrt{(\cos\omega)^2 + (\sin\omega)^2} \\
&= \sqrt{1} = 1
\end{aligned}
\tag{A.9}
$$

$$
\begin{aligned}
|\mathbf{r}_3| &= \sqrt{r_{31}^2 + r_{32}^2 + r_{33}^2} \\
&= \sqrt{(\sin\omega \sin\kappa - \cos\omega \sin\varphi \cos\kappa)^2 + (\sin\omega \cos\kappa + \cos\omega \sin\varphi \sin\kappa)^2 + (\cos\omega \cos\varphi)^2} \\
&= \sqrt{(\sin\omega)^2 \left((\sin\kappa)^2 + (\cos\kappa)^2\right) + (\cos\omega \sin\varphi)^2 \left((\sin\kappa)^2 + (\cos\kappa)^2\right) + (\cos\omega \cos\varphi)^2} \\
&= \sqrt{(\sin\omega)^2 + (\cos\omega \sin\varphi)^2 + (\cos\omega \cos\varphi)^2} \\
&= \sqrt{(\sin\omega)^2 + (\cos\omega)^2 \left((\sin\varphi)^2 + (\cos\varphi)^2\right)} \\
&= \sqrt{(\sin\omega)^2 + (\cos\omega)^2} \\
&= \sqrt{1} = 1
\end{aligned}
\tag{A.10}
$$

Similarly, the norm of the first, second, and third columns are $|\mathbf{c}_1|$, $|\mathbf{c}_2|$, and $|\mathbf{c}_3|$, respectively, and can be computed as:

$$
\begin{aligned}
|\mathbf{c}_1| &= \sqrt{r_{11}^2 + r_{21}^2 + r_{31}^2} \\
&= \sqrt{(\cos\varphi \cos\kappa)^2 + (\cos\omega \sin\kappa + \sin\omega \sin\varphi \cos\kappa)^2 + (\sin\omega \sin\kappa - \cos\omega \sin\varphi \cos\kappa)^2} \\
&= \sqrt{(\cos\varphi \cos\kappa)^2 + (\sin\kappa)^2 \left((\cos\omega)^2 + (\sin\omega)^2\right) + (\sin\varphi \cos\kappa)^2 \left((\sin\omega)^2 + (\cos\omega)^2\right)} \\
&= \sqrt{(\cos\varphi \cos\kappa)^2 + (\sin\kappa)^2 + (\sin\varphi \cos\kappa)^2} \\
&= \sqrt{(\cos\kappa)^2 \left((\cos\varphi)^2 + (\sin\varphi)^2\right) + (\sin\kappa)^2} \\
&= \sqrt{(\cos\kappa)^2 + (\sin\kappa)^2} \\
&= \sqrt{1} = 1
\end{aligned}
\tag{A.11}
$$

$$\begin{aligned}
|\mathbf{c}_2| &= \sqrt{r_{12}^2 + r_{22}^2 + r_{32}^2} \\
&= \sqrt{(-\cos\varphi\sin\kappa)^2 + (\cos\omega\cos\kappa - \sin\omega\sin\varphi\sin\kappa)^2 + (\sin\omega\cos\kappa + \cos\omega\sin\varphi\sin\kappa)^2} \\
&= \sqrt{(\cos\varphi\sin\kappa)^2 + (\cos\kappa)^2\left((\cos\omega)^2 + (\sin\omega)^2\right) + (\sin\varphi\sin\kappa)^2\left((\sin\omega)^2 + (\cos\omega)^2\right)} \\
&= \sqrt{(\cos\varphi\sin\kappa)^2 + (\cos\kappa)^2 + (\sin\varphi\sin\kappa)^2} \\
&= \sqrt{(\sin\kappa)^2\left((\cos\varphi)^2 + (\sin\varphi)^2\right) + (\cos\kappa)^2} \\
&= \sqrt{(\sin\kappa)^2 + (\cos\kappa)^2} \\
&= \sqrt{1} = 1
\end{aligned} \tag{A.12}$$

$$\begin{aligned}
|\mathbf{c}_2| &= \sqrt{r_{13}^2 + r_{23}^2 + r_{33}^2} \\
&= \sqrt{(\sin\varphi)^2 + (-\sin\omega\cos\varphi)^2 + (\cos\omega\cos\varphi)^2} \\
&= \sqrt{(\sin\varphi)^2 + (\cos\varphi)^2\left((\cos\omega)^2 + (\sin\omega)^2\right)} \\
&= \sqrt{(\sin\varphi)^2 + (\cos\varphi)^2} \\
&= \sqrt{1} = 1
\end{aligned} \tag{A.13}$$

Therefore, $\mathbf{r}_1$, $\mathbf{r}_2$, $\mathbf{r}_3$, $\mathbf{c}_1$, $\mathbf{c}_2$ and $\mathbf{c}_3$ are unit vectors (normality condition).

The dot product of the vectors that represents the rows of R can be computed as:

$$\begin{aligned}
\mathbf{r}_1 \circ \mathbf{r}_2 &= r_{11}r_{21} + r_{12}r_{22} + r_{13}r_{23} \\
&= (\cos\varphi\cos\kappa)(\cos\omega\sin\kappa + \sin\omega\sin\varphi\cos\kappa) \\
&\quad + (-\cos\varphi\sin\kappa)(\cos\omega\cos\kappa - \sin\omega\sin\varphi\sin\kappa) + (\sin\varphi)(-\sin\omega\cos\varphi) \\
&= (\cos\varphi\cos\kappa)(\cos\omega\sin\kappa) + (\cos\varphi\cos\kappa)(\sin\omega\sin\varphi\cos\kappa) \\
&\quad - (\cos\varphi\sin\kappa)(\cos\omega\cos\kappa) + (\cos\varphi\sin\kappa)(\sin\omega\sin\varphi\sin\kappa) - (\sin\varphi)(\sin\omega\cos\varphi) \\
&= (\cos\varphi\cos\kappa)(\sin\omega\sin\varphi\cos\kappa) + (\cos\varphi\sin\kappa)(\sin\omega\sin\varphi\sin\kappa) \\
&\quad - (\sin\omega\sin\varphi\cos\varphi) \\
&= (\sin\omega\sin\varphi\cos\varphi)\left((\cos\kappa)^2 + (\sin\kappa)^2 - 1\right) \\
&= (\sin\omega\sin\varphi\cos\varphi)(1 - 1) \\
&= 0
\end{aligned} \tag{A.14}$$

$$
\begin{aligned}
\mathbf{r}_1 \circ \mathbf{r}_3 &= r_{11}r_{31} + r_{12}r_{32} + r_{13}r_{33} \\
&= (\cos\varphi\cos\kappa)(\sin\omega\sin\kappa - \cos\omega\sin\varphi\cos\kappa) \\
&\quad +(-\cos\varphi\sin\kappa)(\sin\omega\cos\kappa + \cos\omega\sin\varphi\sin\kappa) + (\sin\varphi)(\cos\omega\cos\varphi) \\
&= (\cos\varphi\cos\kappa)(\sin\omega\sin\kappa) - (\cos\varphi\cos\kappa)(\cos\omega\sin\varphi\cos\kappa) \\
&\quad -(\cos\varphi\sin\kappa)(\sin\omega\cos\kappa) - (\cos\varphi\sin\kappa)(\cos\omega\sin\varphi\sin\kappa) + (\sin\varphi)(\cos\omega\cos\varphi) \\
&= -(\cos\varphi\cos\kappa)(\cos\omega\sin\varphi\cos\kappa) - (\cos\varphi\sin\kappa)(\cos\omega\sin\varphi\sin\kappa) \\
&\quad +(\cos\omega\sin\varphi\cos\varphi) \\
&= (\cos\omega\sin\varphi\cos\varphi)\left(-(\cos\kappa)^2 - (\sin\kappa)^2 + 1\right) \\
&= (\cos\omega\sin\varphi\cos\varphi)(-1+1) \\
&= 0
\end{aligned}
\tag{A.15}
$$

$$
\begin{aligned}
\mathbf{r}_2 \circ \mathbf{r}_3 &= r_{21}r_{31} + r_{22}r_{32} + r_{23}r_{33} \\
&= (\cos\omega\sin\kappa + \sin\omega\sin\varphi\cos\kappa)(\sin\omega\sin\kappa - \cos\omega\sin\varphi\cos\kappa) \\
&\quad +(\cos\omega\cos\kappa - \sin\omega\sin\varphi\sin\kappa)(\sin\omega\cos\kappa + \cos\omega\sin\varphi\sin\kappa) \\
&\quad +(-\sin\omega\cos\varphi)(\cos\omega\cos\varphi) \\
&= (\sin\omega\cos\omega)\left((\sin\kappa)^2 + (\cos\kappa)^2\right) - \left(\sin\omega\cos\omega(\sin\varphi)^2\right)\left((\sin\kappa)^2 + (\cos\kappa)^2\right) \\
&\quad -(\sin\omega\cos\varphi)(\cos\omega\cos\varphi) \\
&= (\sin\omega\cos\omega) - \left(\sin\omega\cos\omega(\sin\varphi)^2\right) - (\sin\omega\cos\varphi)(\cos\omega\cos\varphi) \\
&= (\sin\omega\cos\omega)\left(1 - (\sin\varphi)^2 - (\cos\varphi)^2\right) \\
&= (\sin\omega\cos\omega)(1-1) \\
&= 0
\end{aligned}
\tag{A.16}
$$

Similarly, the dot product of the vectors that represents the columns of R can be computed as:

$$
\begin{aligned}
\mathbf{c}_1 \circ \mathbf{c}_2 &= r_{11}r_{12} + r_{21}r_{22} + r_{31}r_{32} \\
&= (\cos\varphi\cos\kappa)(-\cos\varphi\sin\kappa) \\
&\quad +(\cos\omega\sin\kappa + \sin\omega\sin\varphi\cos\kappa)(\cos\omega\cos\kappa - \sin\omega\sin\varphi\sin\kappa) \\
&\quad +(\sin\omega\sin\kappa - \cos\omega\sin\varphi\cos\kappa)(\sin\omega\cos\kappa + \cos\omega\sin\varphi\sin\kappa) \\
&= -(\cos\varphi\cos\kappa)(\cos\varphi\sin\kappa) \\
&\quad +(\sin\kappa\cos\kappa)\left((\cos\omega)^2 + (\sin\omega)^2\right) - \left((\sin\varphi)^2\sin\kappa\cos\kappa\right)\left((\sin\omega)^2 + (\sin\omega)^2\right) \\
&= -(\cos\varphi\cos\kappa)(\cos\varphi\sin\kappa) + (\sin\kappa\cos\kappa) - \left((\sin\varphi)^2\sin\kappa\cos\kappa\right) \\
&= (\sin\kappa\cos\kappa)\left(-(\cos\varphi)^2 - (\sin\varphi)^2 + 1\right) \\
&= (\sin\kappa\cos\kappa)(-1+1) \\
&= 0
\end{aligned}
\tag{A.17}
$$

$$\begin{aligned}
\mathbf{c}_1 \circ \mathbf{c}_3 &= r_{11}r_{13} + r_{21}r_{23} + r_{31}r_{33} \\
&= (\cos\varphi\cos\kappa)(\sin\varphi) + (\cos\omega\sin\kappa + \sin\omega\sin\varphi\cos\kappa)(-\sin\omega\cos\varphi) \\
&\quad +(\sin\omega\sin\kappa - \cos\omega\sin\varphi\cos\kappa)(\cos\omega\cos\varphi) \\
&= (\cos\varphi\cos\kappa)(\sin\varphi) - (\cos\omega\sin\kappa)(\sin\omega\cos\varphi) - (\sin\omega\sin\varphi\cos\kappa)(\sin\omega\cos\varphi) \\
&\quad +(\sin\omega\sin\kappa)(\cos\omega\cos\varphi) - (\cos\omega\sin\varphi\cos\kappa)(\cos\omega\cos\varphi) \\
&= (\sin\varphi\cos\varphi\cos\kappa) - (\sin\omega\sin\varphi\cos\kappa)(\sin\omega\cos\varphi) \\
&\quad -(\cos\omega\sin\varphi\cos\kappa)(\cos\omega\cos\varphi) \\
&= (\sin\varphi\cos\varphi\cos\kappa)\left(1 - (\sin\omega)^2 - (\cos\omega)^2\right) \\
&= (\sin\varphi\cos\varphi\cos\kappa)(1-1) \\
&= 0
\end{aligned} \tag{A.18}$$

$$\begin{aligned}
\mathbf{c}_2 \circ \mathbf{c}_3 &= r_{12}r_{13} + r_{22}r_{23} + r_{32}r_{33} \\
&\quad (-\cos\varphi\sin\kappa)(\sin\varphi) + (\cos\omega\cos\kappa - \sin\omega\sin\varphi\sin\kappa)(-\sin\omega\cos\varphi) \\
&\quad +(\sin\omega\cos\kappa + \cos\omega\sin\varphi\sin\kappa)(\cos\omega\cos\varphi) \\
&= -(\cos\varphi\sin\kappa)(\sin\varphi) - (\cos\omega\cos\kappa)(\sin\omega\cos\varphi) + (\sin\omega\sin\varphi\sin\kappa)(\sin\omega\cos\varphi) \\
&\quad +(\sin\omega\cos\kappa)(\cos\omega\cos\varphi) + (\cos\omega\sin\varphi\sin\kappa)(\cos\omega\cos\varphi) \\
&= -(\sin\varphi\cos\varphi\sin\kappa) + (\sin\omega\sin\varphi\sin\kappa)(\sin\omega\cos\varphi) \\
&\quad +(\cos\omega\sin\varphi\sin\kappa)(\cos\omega\cos\varphi) \\
&= (\sin\varphi\cos\varphi\sin\kappa)\left(-1 + (\sin\omega)^2 + (\cos\omega)^2\right) \\
&= (\sin\varphi\cos\varphi\sin\kappa)(-1+1) \\
&= 0
\end{aligned} \tag{A.19}$$

Therefore, the vectors representing the rows, or columns, of the rotation matrix *R* are orthogonal (orthogonality condition).

Hence, it can be concluded that the rotation matrix *R* is orthonormal.

Another proof of the orthonormality of the rotation matrix can be made in the following form:

$$\begin{aligned}
R^T R &= \left(R_\omega R_\varphi R_\kappa\right)^T R_\omega R_\varphi R_\kappa \\
&= \left(R_\kappa\right)^T \left(R_\varphi\right)^T \left(R_\omega\right)^T R_\omega R_\varphi R_\kappa \\
&= \left(R_\kappa\right)^T \left(R_\varphi\right)^T I.R_\varphi R_\kappa \\
&= \left(R_\kappa\right)^T \left(R_\varphi\right)^T R_\varphi R_\kappa \\
&= \left(R_\kappa\right)^T I.R_\kappa \\
&= \left(R_\kappa\right)^T R_\kappa \\
&= I
\end{aligned} \tag{A.20}$$

where each of rotation matrices R_ω, R_φ, or R_κ is orthonormal. Similarly:

$$\begin{aligned}
R.R^T &= R_\omega R_\varphi R_\kappa \left(R_\omega R_\varphi R_\kappa\right)^T \\
&= R_\omega R_\varphi R_\kappa \left(R_\kappa\right)^T \left(R_\varphi\right)^T \left(R_\omega\right)^T \\
&= R_\omega R_\varphi .I\left(R_\varphi\right)^T \left(R_\omega\right)^T \\
&= R_\omega R_\varphi \left(R_\varphi\right)^T \left(R_\omega\right)^T \\
&= R_\omega .I\left(R_\omega\right)^T \\
&= R_\omega \left(R_\omega\right)^T \\
&= I
\end{aligned} \tag{A.21}$$

Therefore, R is an orthonormal matrix.

A.4 Orientation Vectors in Frame Images

The main objective is to determine the vectors that correspond to the image axis, **x**, **y**, and **z**, (see Figure A.2) with respect to the object coordinate system.

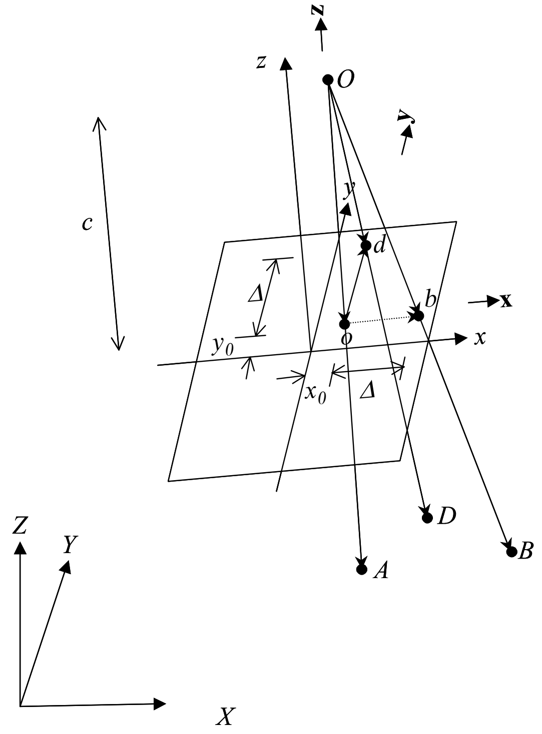

Figure A.2: Unit vectors **x**, **y**, and **z** that correspond to the image coordinate axes with respect to the object coordinate system

A.4.1 Orientation Vector z

As shown in Figure A.2, vector *Oo* corresponds to the optical axis. In order to determine it in space, x_0 and y_0 can substitute for x_a, and y_a, respectively (i.e., writing the collinearity equations for point *o*). Therefore:

$$OA = \begin{bmatrix} X_A - X_0 \\ Y_A - Y_0 \\ Z_A - Z_0 \end{bmatrix} = \frac{1}{\lambda} R \begin{bmatrix} x_0 - x_0 \\ y_0 - y_0 \\ -c \end{bmatrix}$$

$$= \frac{1}{\lambda} R \begin{bmatrix} 0 \\ 0 \\ -c \end{bmatrix} \tag{A.22}$$

$$= -\frac{c}{\lambda} \begin{bmatrix} r_{13} \\ r_{23} \\ r_{33} \end{bmatrix}$$

Thus, vector $(X_A\text{-}X_0, Y_A\text{-}Y_0, Z_A\text{-}Z_0)^T$ represents the space vector of the optical axis pointing downwards. Therefore, a unit vector along the optical axis can be obtained by normalizing this vector:

$$\frac{OA}{|OA|} = \frac{1}{\sqrt{(X_A - X_0)^2 + (Y_A - Y_0)^2 + (Z_A - Z_0)^2}} \begin{bmatrix} X_A - X_0 \\ Y_A - Y_0 \\ Z_A - Z_0 \end{bmatrix}$$

$$= \frac{-\frac{c}{\lambda}}{\frac{c}{\lambda}\sqrt{r_{13}^2 + r_{23}^2 + r_{33}^2}} \begin{bmatrix} r_{13} \\ r_{23} \\ r_{33} \end{bmatrix}$$

Using Equation A.13, the above normal vector can be rewritten as:

$$\frac{OA}{|OA|} = -\begin{bmatrix} r_{13} \\ r_{23} \\ r_{33} \end{bmatrix} \tag{A.23}$$

This is the same unit direction vector along *Oo*, which is parallel to *z*-axis but in the opposite direction. Therefore, the unit vector along the *z*-axis, **z**, is expressed with respect to the object coordinate system as:

$$\mathbf{z} = \begin{bmatrix} r_{13} \\ r_{23} \\ r_{33} \end{bmatrix} \tag{A.24}$$

Vector *Oo* has a length of c and, therefore, can be expressed as:

$$Oo = -c\begin{bmatrix} r_{13} \\ r_{23} \\ r_{33} \end{bmatrix} \tag{A.25}$$

A.4.2 Orientation Vector x

In order to determine a vector along *x*-axis, image point *b* whose coordinates with respect to the image coordinate system are $(\Delta + x_0, y_0, 0)^T$ is selected, where Δ is an arbitrary distance. In other words, line *ob* is parallel to the *x*-axis. The object space point is *B* and its coordinates with respect to the object coordinate system are $(X_B, Y_B, Z_B)^T$. Using point *B* and its image point *b* in the collinearity equations, vector *OB*, connecting the perspective center to the object point, with respect to the object coordinate system can be obtained as:

$$\begin{aligned} OB = \begin{bmatrix} X_{\mathbf{B}} - X_0 \\ Y_B - Y_0 \\ Z_B - Z_0 \end{bmatrix} &= \frac{1}{\lambda} R \begin{bmatrix} \Delta + x_0 - x_0 \\ y_0 - y_0 \\ -c \end{bmatrix} \\ &= \frac{1}{\lambda} R \begin{bmatrix} \Delta \\ 0 \\ -c \end{bmatrix} \\ &= \frac{1}{\lambda} \begin{bmatrix} r_{11}\Delta - r_{13}c \\ r_{21}\Delta - r_{23}c \\ r_{31}\Delta - r_{33}c \end{bmatrix} \end{aligned} \tag{A.26}$$

A unit vector along *OB* can be expressed as:

$$\frac{OB}{|OB|}=\frac{1}{\sqrt{(X_B-X_0)^2+(Y_B-Y_0)^2+(Z_B-Z_0)^2}}\begin{bmatrix}X_{\mathbf{B}}-X_0\\Y_B-Y_0\\Z_B-Z_0\end{bmatrix}$$

$$=\frac{\frac{1}{\lambda}}{\frac{1}{\lambda}\sqrt{(r_{11}\Delta-r_{13}c)^2+(r_{21}\Delta-r_{23}c)^2+(r_{31}\Delta-r_{33}c)^2}}\begin{bmatrix}r_{11}\Delta-r_{13}c\\r_{21}\Delta-r_{23}c\\r_{31}\Delta-r_{33}c\end{bmatrix}$$

$$=\frac{1}{\sqrt{\Delta^2\left((r_{11})^2+(r_{21})^2+(r_{31})^2\right)+c^2\left((r_{13})^2+(r_{23})^2+(r_{33})^2\right)-2c\Delta(r_{11}r_{13}+r_{21}r_{23}+r_{31}r_{33})}}\times$$

$$\begin{bmatrix}r_{11}\Delta-r_{13}c\\r_{21}\Delta-r_{23}c\\r_{31}\Delta-r_{33}c\end{bmatrix}$$

Using Equations A.11, A.13 and A.18:

$$\frac{OB}{|OB|}=\frac{1}{\sqrt{\Delta^2+c^2}}\begin{bmatrix}r_{11}\Delta-r_{13}c\\r_{21}\Delta-r_{23}c\\r_{31}\Delta-r_{33}c\end{bmatrix} \tag{A.27}$$

Which is also the unit vector along *Ob* with respect to the object coordinate system.

Vector *Ob* has a length of $\sqrt{\Delta^2+c^2}$. Therefore, it can be expressed as:

$$Ob=\begin{bmatrix}r_{11}\Delta-r_{13}c\\r_{21}\Delta-r_{23}c\\r_{31}\Delta-r_{33}c\end{bmatrix} \tag{A.28}$$

Therefore, vector *ob*, which is parallel to the *x*-axis can be expressed as:

$$ob = Ob - Oo = \begin{bmatrix} r_{11}\Delta - r_{13}c \\ r_{21}\Delta - r_{23}c \\ r_{31}\Delta - r_{33}c \end{bmatrix} + c\begin{bmatrix} r_{13} \\ r_{23} \\ r_{33} \end{bmatrix} = \Delta\begin{bmatrix} r_{11} \\ r_{21} \\ r_{31} \end{bmatrix} \tag{A.29}$$

Therefore, a unit vector along *ob*, which is the same unit vector along the *x*-axis, **x**, is:

$$\mathbf{x} = \begin{bmatrix} r_{11} \\ r_{21} \\ r_{31} \end{bmatrix} \tag{A.30}$$

A.4.3 Orientation Vector y

In order to determine a vector along the *y*-axis, image point *d*, whose coordinates with respect to the image coordinate system are $(x_0, \Delta + y_0, 0)^T$, is selected, where Δ is an arbitrary distance. In other words, line *od* is parallel to the *y*-axis. The object space point is *D* and its coordinates with respect to the object coordinate system are $(X_D, Y_D, Z_D)^T$. Using point *D* and its image point *d* in the collinearity equations, vector *OD* with respect to the object coordinate system can be obtained as:

$$OD = \begin{bmatrix} X_D - X_0 \\ Y_D - Y_0 \\ Z_D - Z_0 \end{bmatrix} = \frac{1}{\lambda} R \begin{bmatrix} x_0 - x_0 \\ \Delta + y_0 - y_0 \\ -c \end{bmatrix} = \frac{1}{\lambda} R \begin{bmatrix} 0 \\ \Delta \\ -c \end{bmatrix} = \frac{1}{\lambda} \begin{bmatrix} r_{12}\Delta - r_{13}c \\ r_{22}\Delta - r_{23}c \\ r_{32}\Delta - r_{33}c \end{bmatrix} \tag{A.31}$$

A unit vector along *OD* can be expressed as:

$$\frac{OD}{|OD|}=\frac{1}{\sqrt{(X_D-X_0)^2+(Y_D-Y_0)^2+(Z_D-Z_0)^2}}\begin{bmatrix}X_D-X_0\\ Y_D-Y_0\\ Z_D-Z_0\end{bmatrix}$$

$$=\frac{\frac{1}{\lambda}}{\frac{1}{\lambda}\sqrt{(r_{12}\Delta-r_{13}c)^2+(r_{22}\Delta-r_{23}c)^2+(r_{32}\Delta-r_{33}c)^2}}\begin{bmatrix}r_{12}\Delta-r_{13}c\\ r_{22}\Delta-r_{23}c\\ r_{32}\Delta-r_{33}c\end{bmatrix}$$

$$=\frac{1}{\sqrt{\Delta^2\left((r_{12})^2+(r_{22})^2+(r_{32})^2\right)+c^2\left((r_{13})^2+(r_{23})^2+(r_{33})^2\right)-2c\Delta(r_{12}r_{13}+r_{22}r_{23}+r_{32}r_{33})}}\times$$

$$\begin{bmatrix}r_{12}\Delta-r_{13}c\\ r_{22}\Delta-r_{23}c\\ r_{32}\Delta-r_{33}c\end{bmatrix}$$

Using Equations A.12, A.13 and A.19:

$$\frac{OD}{|OD|}=\frac{1}{\sqrt{\Delta^2+c^2}}\begin{bmatrix}r_{12}\Delta-r_{13}c\\ r_{22}\Delta-r_{23}c\\ r_{32}\Delta-r_{33}c\end{bmatrix} \tag{A.32}$$

which is also a unit vector along *Od* with respect to the object coordinate system. Vector *Od* has a length of $\sqrt{\Delta^2+c^2}$. Therefore, it can be expressed as:

$$Od=\begin{bmatrix}r_{12}\Delta-r_{13}c\\ r_{22}\Delta-r_{23}c\\ r_{32}\Delta-r_{33}c\end{bmatrix} \tag{A.33}$$

Therefore, vector *od*, which is parallel to *y*-axis can be expressed as:

$$
\begin{aligned}
od = Od - Oo &= \begin{bmatrix} r_{12}\Delta - r_{13}c \\ r_{22}\Delta - r_{23}c \\ r_{32}\Delta - r_{33}c \end{bmatrix} + c\begin{bmatrix} r_{13} \\ r_{23} \\ r_{33} \end{bmatrix} \\
&= \Delta\begin{bmatrix} r_{12} \\ r_{22} \\ r_{32} \end{bmatrix}
\end{aligned}
\tag{A.34}
$$

Therefore, a unit vector along *od*, which is the same unit vector along the *y*-axis, **y**, is:

$$
\mathbf{y} = \begin{bmatrix} r_{12} \\ r_{22} \\ r_{32} \end{bmatrix} \tag{A.35}
$$

In conclusion, vectors **x**, **y**, and **z** represent the first, second and third columns, respectively, of the rotation matrix *R*. It is also important to recall the orthonormality of these vectors.